

POLITECNICO DI MILANO
Corso di Laurea in Ingegneria Elettronica
Dipartimento di Elettronica e Informazione



Development of the HICAM imaging system for SPECT applications

Relatore:

Chiar.mo Prof. Carlo Fiorini

Correlatori:

Ing. Paolo Busca

Ing. Roberta Peloso

Tesi di Laurea di:
Mattia Colombo, matricola 735728

Anno Accademico 2010-2011

To my family and my friends

Abstract

Nuclear medical imaging is a generic term that covers many imaging techniques based on the interaction of ionizing radiations into biological tissues, with the common aim to gather information about metabolic activity of the studied object.

The goal of the *Hicam project* was the development of a compact, light-weighted gamma camera, for earlier and more reliable diagnosis and therapy planning of cancer in specific applications. A high overall spatial resolution, system compactness and the capability to place the detector near the target are the most significant features of this novel diagnostic instrument of European interest.

During the project two prototypes were built, offering a 25cm^2 and a 100cm^2 field of view, and following the well-known Anger architecture, now implementing solid state detectors. In fact, a gamma camera based on SDDs represents an imaging device with several potentialities in the field of medical imaging, thanks to the possibility to achieve a good spatial resolution and the opportunity to integrate the system in a magnetic resonance environment.

The research objective of this thesis is to study the behaviour of the gamma camera throughout the phases of the imaging process. A simulator was involved in preliminary analyses to anticipate the functioning of the gamma camera together with the issues associated to the structure of the device, like the geometry or the materials involved. Performances of the detectors were checked taking advantage of specific measurements, allowing us to install and exploit SDDs in optimal working conditions. Eventually, experimental data were processed with a customized software allowing the reconstruction of enhanced images; calibrations and corrections were performed taking advantage of the results achieved in preliminary studies.

A comparison between Hicam and a commercial gamma camera is presented to show the results achieved in planar scintigraphy. Tomographic acquisitions were also carried out on small phantoms, showing how this prototype, provided with a high spatial resolution, may be involved in SPECT measurements on small animals or human patients.

Sommario

La *medicina nucleare* è una metodica di diagnostica per immagini le cui tecniche si basano sull'interazione di radiazioni ionizzanti all'interno dei tessuti biologici, con lo scopo di raccogliere informazioni relative all'attività metabolica dell'oggetto di studio.

L'obiettivo del *progetto Hicam* è stato lo sviluppo di una gamma camera leggera e compatta, utile per eseguire diagnosi preliminari più affidabili e in applicazioni specifiche per la pianificazione di terapie contro il cancro. Questo dispositivo presenta caratteristiche molto significative, come l'elevata risoluzione spaziale, la compattezza, e la possibilità di posizionare la gamma camera vicino al paziente, rendendolo uno strumento unico e di interesse europeo.

Durante il progetto sono stati costruiti due prototipi con un campo di vista di 25cm^2 e 100cm^2 , proponendo una struttura che riprende l'architettura di Anger, implementando però rivelatori a stato solido in sostituzione dei fototubi. Infatti, una gamma camera che integra SDD è un dispositivo con grandi potenzialità in ambito biomedicale grazie alla possibilità di ottenere un'elevata risoluzione spaziale e all'opportunità di effettuare misure congiuntamente ad un apparato di imaging a risonanza magnetica.

L'obiettivo di questa tesi è lo studio del comportamento della gamma camera in tutte le fasi del processo di imaging. Analisi preliminari sono state effettuate grazie all'uso di un simulatore per comprendere le dinamiche dei fenomeni fisici coinvolti nella rivelazione, e prevedere i possibili problemi. Successivamente sono state eseguite delle misure per garantire il corretto funzionamento dei sensori, cercando di utilizzarli in condizioni di lavoro ottimali. Infine è stato realizzato un software ad-hoc, per processare i dati e migliorare la ricostruzione delle immagini attraverso calibrazioni e correzioni, elaborate a partire dai risultati ottenuti nelle precedenti analisi.

Viene inoltre presentato un confronto tra gli esami scintigrafici effettuati con Hicam e quelli realizzati con una gamma camera commerciale, con l'obiettivo di mostrare le prestazioni del dispositivo e i risultati ottenuti. Grazie alla notevole risoluzione spaziale dello strumento, è stato possibile eseguire acquisizioni tomografiche (SPECT) di piccoli modelli adatti alla valutazione delle prestazioni, dimostrando come questi esperimenti possano essere estesi anche a pazienti umani, o piccoli animali.

Contents

Abstract	I
Sommario	III
1 Introduction	1
2 Analysis of a γ-ray detection system	3
2.1 General radiation features	3
2.1.1 X-ray and γ -ray	3
2.1.2 Origin of γ -rays	5
2.1.3 Interaction of γ -rays with matter	6
2.2 Principles of radiation detection	10
2.2.1 Architecture of a gamma camera	11
2.2.2 Detection efficiency	12
2.2.3 Interaction in the detector	13
2.2.4 Performances and objectives	14
2.3 Electronic read-out	16
3 Structure of the Hicam system	21
3.1 Gamma camera	21
3.1.1 Collimator	22
3.1.2 Scintillation crystal	24
3.1.3 Photodetector array	27
3.1.4 Case and sealing	33
3.2 Holder board	34
3.2.1 Electronic read-out	35
3.3 Motherboard	35
3.4 Data acquisition board	36
3.5 Acquisition and reconstruction software	37
4 Charge collection analysis	39
4.1 Spatial resolution and energy resolution	39
4.2 Energy resolution analysis	41
4.2.1 Calculating the total energy resolution	41

4.2.2	Intrinsic contribution	43
4.2.3	Statistical contribution	43
4.2.4	Electronic noise contribution	52
4.3	Dead areas impact	58
4.4	Reconstruction issues	61
4.4.1	Hicam25 - first issues	61
4.4.2	Hicam100 - unexpected issues	62
5	Reconstruction software	73
5.1	Image reconstruction	74
5.2	Calibrations and corrections	79
5.2.1	Gain and offset calibration	79
5.2.2	Energy correction	81
5.2.3	Uniformity correction	82
5.2.4	Linearity correction	83
5.2.5	Software implementation	85
5.3	Setup of the prototype	86
5.4	Results and applications	88
6	Single photon emission computed tomography	91
6.1	Principles and techniques	91
6.1.1	Filtered backprojection (FBP)	93
6.1.2	Iterative methods	96
6.2	Hicam setup	99
6.3	Image reconstruction	100
7	Conclusion and future developments	105
	Bibliography	108

List of Figures

2.1	Representation of the electromagnetic spectrum, showing an overlap between γ -ray (<i>in yellow</i>) and X-ray (<i>in blue</i>) energy range.	4
2.2	Diagram of <i>Beer-Lambert law</i> , showing how light is absorbed when interacting with matter.	7
2.3	Diagram showing the dynamics of the photoelectric effect. . .	7
2.4	Diagram showing the linear attenuation coefficient as a function of the energy. Different materials are analysed.	8
2.5	Diagram showing the dynamics of the compton scattering. . .	9
2.6	Diagram showing the absorption mechanisms as a function of the energy of the incident photon and the Z of the material. . .	10
2.7	Diagram showing the structure of an Anger Camera.	11
2.8	Schematic representation of the absorption efficiency.	12
2.9	Linear attenuation coefficient and efficiency for Si, Ge, Ar and CsI.	14
2.10	Normalized energy spectrum.	15
2.11	Typical point spread function and calculus of the spatial resolution.	16
2.12	Charge preamplifier configuration in the Hicam system.	17
2.13	Conversion of the signal in the shaping filter.	18
3.1	Impact of the collimator on the detection efficiency and diagram of its inner structure.	22
3.2	Diagram showing how high-energy photons are converted into visible photons.	24
3.3	Diagram of the absorption distribution in a CsI(Tl) crystal, 1cm thick (simulated in Geant3).	26
3.4	Diagram of a single SDD. The contacts of the detector are shown as well as the integrated FET.	28
3.5	The first picture is the trend of the drain current of the integrated FET as a function of the voltage between source and drain. The second picture is the current flowing in the reset diode, after a significant voltage is applied. In the third picture the depletion current of the inner guard ring is plotted.	29

3.6	The first picture is the current flowing from Ring1 to RingN, increasing the voltage difference in between them. The second picture shows how the detector is depleted increasing the negative voltage level of the Back contact. In the third picture the depletion current of the first ring is plotted.	30
3.7	Detector layout for both Hicam25 and Hicam100. The active area of a single detector is outlined in red.	31
3.8	Features and dimensions of the flex PCB and its connector. In the top-right corner a photo of the modules is shown, while on the bottom-right corner there is a photo of the bondings on the bottom of the PCB.	32
3.9	Picture of Hicam100 during assembling stages. All the pieces of the case are visible, except for one lateral panel and the cover.	33
3.10	Picture of Hicam100 during assembling stages. All the pieces of the case are visible, except for one lateral panel and the cover. On this lateral view the connections for nitrogen and cooling liquid are visible.	34
3.11	The holder board is studied to host the ASIC and bring bias voltage levels to the detectors.	34
3.12	The motherboard is connected to the power supply (wiring on the left) and is designed to host up to 4 holder boards.	35
3.13	The digital acquisition board is formed by three different interfaces all plugged in together.	36
3.14	Screenshot of the acquisition software. A thyroid phantom is being reconstructed online, during acquisition.	38
4.1	A trade-off must be discussed when considering charge collection. Different types of coatings have been implemented in order to fulfil the specifications concerning spatial resolution, that is the most expected feature of the Hicam gamma camera.	40
4.2	Spectra of a ^{57}Co and a $^{99\text{m}}\text{Tc}$ source. The sources cannot be distinguished in the global spectrum when analysed together because of a low energy resolution.	41
4.3	Trend of the energy resolution as a function of the energy (left) and trend of the energy resolution as a function of the number of detectors involved (right).	42
4.4	Representation of a generic solid angle $d\Omega$	44
4.5	Representation of Hicam detectors: not all the photons generated after the scintillation are collected (in blue: photons collected, in red: photons lost because of dead areas).	45
4.6	Solid angle including only those photons which are collected by detectors.	46
4.7	In the evaluation of the efficiency map both direct and reflected contribution are considered.	47

4.8	Total efficiency map represented as an interpolated surf plot.	48
4.9	Total efficiency map projections, on Hicam axis.	48
4.10	Reflectance of an incident ray of visible light. Light strikes the interface between a CsI(Tl) ($n_1 = 1.788$) and Visilox optical grease ($n_1 = 1.463$).	49
4.11	Reconstructed image and spectrum of the flood simulation, used to confirm the impact of the statistical contribution to the total energy resolution.	51
4.12	Events reconstructed in different locations in the detector matrix lead to a spread of the spectrum.	52
4.13	Histogram of the number of SDD involved in the detection of a gamma event at 140.2 keV.	52
4.14	Trend of the equivalent noise charge as a result of three different contributions: series, parallel, and $1/f$. The ENC^2 is plotted as a function of the shaping time.	54
4.15	Representation of the ballistic deficit. A significant loss of charge occurs because of a short shaping time.	55
4.16	Some of the detector spectra are shown: a ^{55}Fe source was employed for this acquisition. These are some of detector arrays mounted in the bigger prototype.	56
4.17	Trend of the equivalent noise charge. ENC value is calculated for each SDD, and an average value will be used for the following simulations.	57
4.18	Reconstructed image and spectrum of the flood simulation, used to confirm the impact of the electronic noise contribution to the total energy resolution.	58
4.19	Trend of efficiency along Z-axis, orthogonal to the detector layer. The simulated point of interaction is located at the centre of a detector.	59
4.20	Trend of efficiency along Z-axis, orthogonal to the detector layer. The simulated point of interaction is located at the centre of a dead area.	60
4.21	Reconstructed image of a flood acquisition and average energy absorbed in a given pixel row.	61
4.22	Reconstructed image processed from flood acquisition. Detector layout is omitted to show better the problem.	62
4.23	Simulation of 20 000 γ -rays, divided in two single points.	63
4.24	Reconstructed image of the two points (A) and profile of the counts (B).	63
4.25	Histogram showing the distribution of the SDDs involved. (X_1, Y_1) in figure (A), and (X_2, Y_2) in figure (B).	64
4.26	Simulation of 50 000 γ -rays, randomly distributed in the red area.	65

4.27	Reconstructed image of the simulated data (A) and profile of the counts (B).	65
4.28	Distribution of the error (A), and location of points whose error is over threshold (X axis projections).	66
4.29	Light cast on the detectors in three different positions. Actual centroid is painted in green, while the location of the reconstructed centroid is painted in red.	66
4.30	Location of points whose error is over threshold (A) and light cast on the detectors in two different positions (B). Actual centroid is painted in green, while the location of the reconstructed centroid is painted in red.	67
4.31	Simulation of 50 000 γ -rays, randomly distributed in the red area.	68
4.32	Reconstructed image of the simulated data (A) and profile of the counts (B); comparison with the horizontal dead area profile is also shown (C).	68
4.33	Distribution of the reconstruction error.	69
4.34	Location of points whose error is over threshold: lateral projection (A), frontal projection (B). The frontal projection considers only the points that aren't affected by border effect, evaluated between <i>5mm</i> and <i>45mm</i> ; these boundaries are painted in yellow in (A).	69
4.35	Comparison between the horizontal (A) and vertical (B) dead areas and their effect on reconstruction.	69
4.36	Simulation of two source of events which cast a symmetrical cone of light (A); the profile of the reconstructed image is also shown (B).	70
4.37	Simulation of 80 000 γ -rays, randomly distributed in the red area.	71
4.38	Reconstructed image of the simulated data (A) and profile of the counts (B). Yellow and green areas compensate for each other keeping the integral of the profile constant.	72
4.39	Reconstructed image of the experimental data (A) and profile of the counts (B).	72
5.1	Reconstruction software developed in Matlab environment.	73
5.2	This panel is introduced to select the size and the location of the reconstruction area.	74
5.3	Filtering stage parameters selection.	75
5.4	Main panel of the reconstruction software.	76
5.5	Figure of the reconstructed image, displayed together with the detector layout.	77
5.6	Figure showing the slides of a tomographic acquisition. A <i>mini-movie</i> can be generated to display the rotating phantom.	78

5.7	The data manager allows to save and load images saved in different formats.	78
5.8	Graphic user interface implemented to visualize DICOM images.	79
5.9	^{55}Fe spectra of single detectors are not aligned due to manufacturing mismatches, but a suitable calibration can be implemented to align the spectra with the expected iron peaks. .	80
5.10	Global spectrum of a flood image calculated before and after energy correction.	81
5.11	Image of a thyroid phantom shown before and after uniformity correction.	83
5.12	Graphic user interface built to calculate the profile of an image, in order to evaluate spatial resolution. In this screenshot a grid image is shown, processed with uniformity and linearity correction.	84
5.13	Panels embedded in the reconstruction software to load and generate correction maps.	85
5.14	Photographs of the system in operational condition, and diagram showing the final setup.	87
5.15	Comparison of a thyroid phantom (left) with a thyroid of a real patient (right).	89
5.16	Comparison between two measurements of the same patient carried out with a commercial gamma camera (E.cam) and the Hicam prototype.	89
6.1	Principle of tomographic acquisition. The gamma camera is rotating around the patient's body, injected with the tracer. .	92
6.2	Shepp-Logan phantom (500x500 pixels), and corresponding sinogram, calculated between 0° and 359° (step= 2°). Each row of the sinogram is the projection of a slice at a given angular position of the detector.	93
6.3	Modelization of geometry of backprojection. With ray-driven method, value attributed to each pixel along a given direction is proportional to the line length.	94
6.4	Steps of the backprojection algorithm. In the first figure the original phantom is represented. The other figures (A-D) show how the image may be reconstructed taking advantage of 1, 3, 6, 8 projections. In the last two figures the image is reconstructed with 180 projections, which are enough to avoid any artifact; however the image is blurred (E) because of the issues already dealt with, but it may be improved with a common <i>Hamming filter</i> (F), which is a two-dimensional band-pass filter.	95

6.5	Photo of the setup used for SPECT experiments. On the left, 3 capillars are used to perform the calibration of the system, while on the right a typical phantom is being studied with a pinhole collimator.	99
6.6	Comparison between the images reconstructed with the ART algorithm and the images reconstructed with advanced calibration techniques by a partner team from UCL.	101
7.1	A collimated source of ^{137}Cs (661keV) is shifted, while pointed at the gamma camera from an orthogonal direction. The spectrum is calculated considering the measurement of a single point only	107
7.2	Biodistribution of ^{123}I in a small mouse. T=thyroid, B=bladder, S=spleen.	107

Chapter 1

Introduction

“Nothing has such power to broaden the mind as the ability to investigate systematically and truly all that comes under thy observation in life.”

Marcus Aurelius

In this chapter an overview of the thesis will be presented, with a particular focus on the purposes and the objectives of the project, showing how this work was developed to fulfill them.

In the beginning of this thesis a small prototype of the Hicam gamma camera was already functioning. However several issues were to be fixed, and while new solutions regarding the electronics apparatus were being implemented, a detailed study of the behaviour of the gamma camera was required to study what kind of calibrations or corrections were useful to enhance the reconstructed images.

Meanwhile, a bigger prototype was being assembled, and the detector modules needed to undergo a series of measurements to prove their correct functioning in optimal conditions. At first a characterization was carried out to check the performances of the SDDs as semiconductors; the second phase consisted of experimental measurements arranged to find the suitable voltage levels that allow to bias the detectors in the optimal way.

Considering the reconstruction of the images the main goal was the achievement of significant improvements in terms of energy resolution, since it is one of the required specification to complete scintigraphic exams with patients. The sources of the spread of the energy spectrum were the object of a detailed analysis which involved the impact of dead areas too. During this research, it was also discovered that the geometry of the detectors was one of the sources causing inequalities in the reconstructed image, leading to an obvious loss in terms of spatial resolution, which is one of the outstanding features of this prototype. Two solutions had been developed to correct both energy resolution issues and uniformity problems.

The possibility to carry out tomographic experiments allowed us to study the main features of three-dimensional reconstruction, providing a detailed description of state-of-the-art algorithms and presenting a possible implementation of one of them. A special setup was needed to perform this kind of experiments, and it was arranged during one of the measurement campaigns completed in Ospedali Riuniti di Bergamo, where also plain scintigraphic exams were conducted with excellent results.

The structure of the thesis is outlined hereafter:

- *Chapter 2 - Analysis of a γ -ray detection system*: in this chapter the features of a generic gamma camera are presented, together with principles of radiation detection and electronic read-out systems for nuclear applications.
- *Chapter 3 - Structure of the Hicam system*: in this chapter the structure of the Hicam gamma camera is presented, discussing the main characteristics of this complex system. All the parts are separately introduced to show the whole imaging process, starting from the place where radiation is first absorbed and concluding with the final reconstructed image.
- *Chapter 4 - Charge collection analysis*: in this chapter energy resolution is discussed, taking advantage of a detailed analysis of all the contributes leading to a spread in the spectrum. Dead areas impact and problems associated with the implementation of the centroid method are also introduced.
- *Chapter 5 - Reconstruction software*: in this chapter the customized software we developed will be shown. This software allows to reconstruct images and perform all the calibrations and the corrections needed to enhance reconstructed images.
- *Chapter 6 - Single photon emission computed tomography*: in this chapter we will talk about tomographic reconstruction, discussing the techniques and the algorithms usually implemented, and showing results from experimental data acquired with the Hicam gamma camera.
- *Chapter 7 - Conclusion and future developments*: in the final chapter conclusions to this work are reported alongside with some current and future applications where the performances of Hicam may be fully exploited.

Chapter 2

Analysis of a γ -ray detection system

“I did not think; I investigated. I assumed that the effect must have come from the tube, since its character indicated that it could come from nowhere else. I tested it. In a few minutes there was no doubt about it. Rays were coming from the tube which had a luminescent effect upon the paper. I tried it successfully at greater and greater distances, even at two metres. It seemed at first a new kind of invisible light. It was clearly something new, something unrecorded.”

Wilhelm Conrad Röntgen

In this chapter we will introduce the basic γ -ray principles and analyse the mechanism of light detection, since all these elements are necessary to build a gamma camera prototype. We will also talk about the improvements that need to be achieved like a reasonable spatial and energetic resolution, which are prerequisites of a working apparatus in the medical field. The main features of the electronic read-out system will be discussed as well as some generic characteristics of the detectors, focusing on the choices of our project.

2.1 General radiation features

2.1.1 X-ray and γ -ray

Both X-ray and γ -ray are commonly used to perform some important medical exams, involving structural and functional analyses of the human body. Considering the electromagnetic spectrum, it's visible that both X-ray and γ -ray are high-frequency waveforms, thus high-energy radiations are sent out during this kind of activities, and it's important to understand how they are generated and how they interact with matter. Most of the pictures showing

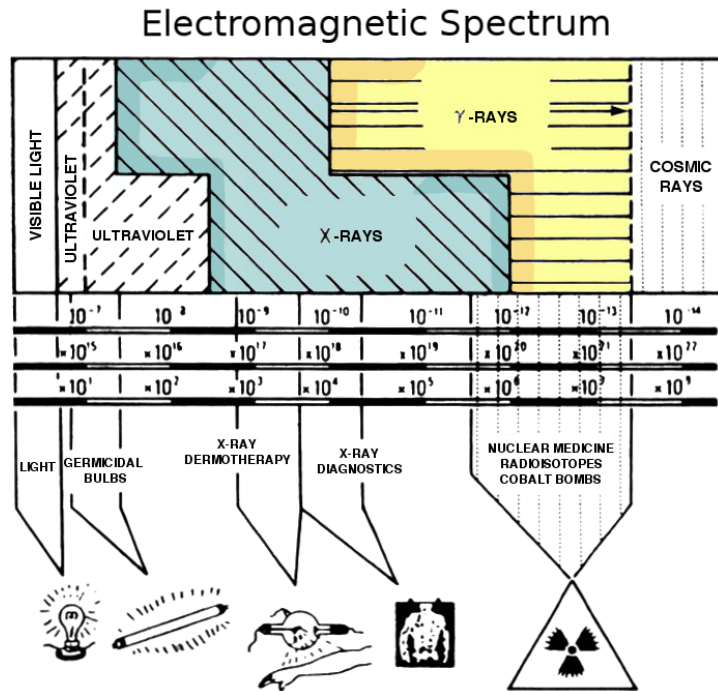


Figure 2.1: Representation of the electromagnetic spectrum, showing an overlap between γ -ray (in yellow) and X-ray (in blue) energy range.

the EM spectrum usually point out that the main difference between X-ray and γ -ray is their energy range, however in Figure 2.1 we can see that there is a partial overlap in their spectra, and that's the range usually involved in medical applications. Actually, the real difference is in the origin of the radiation: in fact, γ -rays are sent out as a result of nuclear phenomena while X-rays are a consequence of a changing in the electron energy state, like fluorescence or Brehmsstrahlung [1].

X-rays have lots of medical applications like radiographic scan, computerized axial tomography, mammography and dual-emission X-ray absorptiometry (DEXA [2]), which is a means of measuring bone mineral density. In general, these exams are used for a structural analysis of the human body: the outline of the final image is depending on the properties of the tissues, which bring to different levels of absorption, even if radiations are spread in a uniform way from the source. In this field, X-rays are usually employed in a range included between 1 KeV and 300 KeV.

From now on, we will concentrate on γ -rays, since we're dealing with a gamma-camera prototype.

2.1.2 Origin of γ -rays

Several elements of the periodic table can be found in an energetically unstable state because of their nuclear composition: these isotopes are called *radionuclides*, and they reach stability emitting electromagnetic or corpuscular radiations [3]. During this process of transformation, nuclear energy is lost by the involved atom: this phenomenon is called *radioactive decay*, and it is stochastic on the level of single atoms [4]. However, when considering a large number of identical atoms, the decay rate is predictable and characterized by:

$$A = -\frac{dN}{dt} = \lambda N, \quad (2.1)$$

where A is number of decays an object undergoes per second, N is the total number of particles in the sample and λ is the *decay constant*. The decay rate is inherently negative and proportional to the absolute number of unstable atoms. According to the International System of Units (SI), activity is billed in Becquerel (Bq), where 1 Bq corresponds to 1 decay per second. Another unit has also been used, the Curie (Ci), where 1 Ci corresponds to 37 GBq, the number of decays which take place in one second in one gram of ^{226}Ra . The solution to the differential equation is thus an exponentially decreasing function:

$$N(t) = N_0 \cdot e^{(-\lambda t)} = N_0 \cdot e^{(-t/\tau)}, \quad (2.2)$$

where N_0 is the value of N at $t = 0$, and $\tau = 1/\lambda$ is the average lifetime of a radioactive particle (*mean lifetime*). Another commonly used parameter is the *half-life*, that is the time taken for half the radionuclide's atoms to decay. This period of time is due to a probabilistic law, it is typical for each element and its range is included within fractions of a second and millions of years.

$$\tau_{1/2} = \frac{\ln(2)}{\lambda}. \quad (2.3)$$

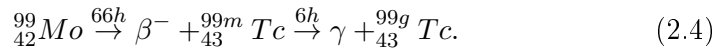
Actually, radioactive emissions can be divided into three types of beams: α , β and γ , and while the first one was seen only in heavy elements, the other two types of decay were seen in all of them. On the one hand α and β are corpuscular radiations, since they consist in particles provided with mass and electrical charge, and they lead to direct ionization. On the other hand, γ -rays are non-corpuscular radiation, since photons have neither mass nor electrical charge.

Furthermore, it's important to point out the differences in the spectra of the radiations: in fact, X -rays and γ -rays are usually characterized by a specific energy value for each isotope, while the spectrum of β particles is

spread in a wider energy range, limited by the expected maximum energy value of a given isotope.

Even if β particles are used in some medical application, like positron emission tomography (PET) ¹, we will now focus on γ -rays for the purpose of our project, as already said before.

In fact, γ -rays are commonly used for diagnostic activities in nuclear medicine: one of the most involved radionuclide is ^{99m}Tc . Technetium undergoes an isomeric transition, a radioactive decay process that involves emission of a gamma ray from an atom where the nucleus is in an excited metastable state; the emission of a gamma ray from an excited nuclear state allows the nucleus to lose energy and reach either a lower energy state [5].



As shown in eq. 2.4, the whole process starts from molybdenum which has an half-life period about $66h$ long, making it easy to be transported. Afterwards it is processed in a *technetium^{99m}generator*, giving birth to the daughter nuclide, technetium in a metastable state, generated together with the emission of a β particle. ^{99m}Tc loses its energy falling to the ground state and emitting a γ -ray (@ $140keV$) during a half-life period of about $6h$. This amount of time is a limitation of the available time for the diagnosis, but it allows the patient not to be hospitalized as a consequence of the decaying radiation.

The last transition represents a changing in the energetic state of the nucleus, without any modification of its composition. The reason that allows the use of this type of radionuclides in nuclear medicine lies in the absence of corpuscular radiation together with a short half-life period, which are biologically favourable features.

2.1.3 Interaction of γ -rays with matter

In order to describe the interaction of radiation with matter, it is necessary to mention the *Beer-Lambert law*, which states that the incident radiation is absorbed according to an exponentially decreasing profile, as show in figure 2.2.

The profile of radiation is thus $I(t) = I_0 \cdot e^{(-\mu t)}$, where μ is the attenuation coefficient, that is a function of the energy of the incident light. Also $\mu = \frac{1}{\lambda}$, where λ is the mean free path or the absorption length, which depends on the physical properties of the material considered. If considering a given

¹For the positron emission tomography, β^+ particles are sent out by the radioactive markers injected in the patient, and they are usually absorbed in a few millimeters. After an annihilation phenomenon two γ -rays are generated, and they're actually detected by the surrounding machinery.

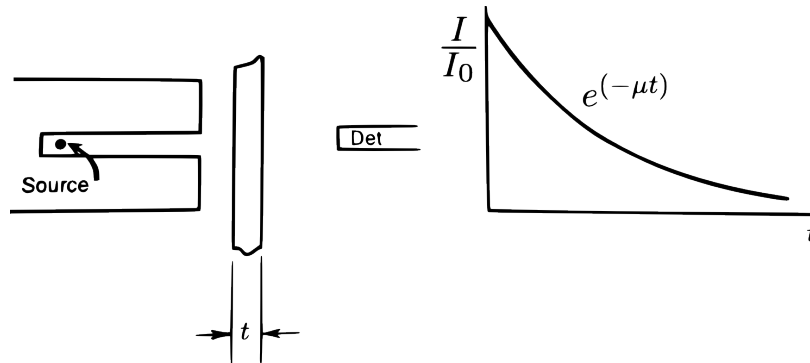


Figure 2.2: Diagram of *Beer-Lambert law*, showing how light is absorbed when interacting with matter.

material as a shield, that should be at least 5λ thick to absorb all the incident radiation. To tell the truth, the attenuation coefficient is also depending on the density of the material: $\mu = \mu' \rho$. Density instead is usually accounted as a constant for all the materials except for gases, therefore the attenuation coefficient μ is the parameter considered for any evaluation. μ' is defined as the *mass attenuation coefficient*, and it is related only to the properties of the material.

The mass attenuation coefficient is the result of three different contributions, which are representative of three different physical phenomena of absorption: photoelectric effect, Compton scattering and pair production.

$$\mu' = \mu'_{\text{photoelectric}} + \mu'_{\text{Compton}} + \mu'_{\text{pair}}$$

Photoelectric effect

The photoelectric effect is one of the most important phenomena when considering the interaction of a photon with matter and its correct interpretation

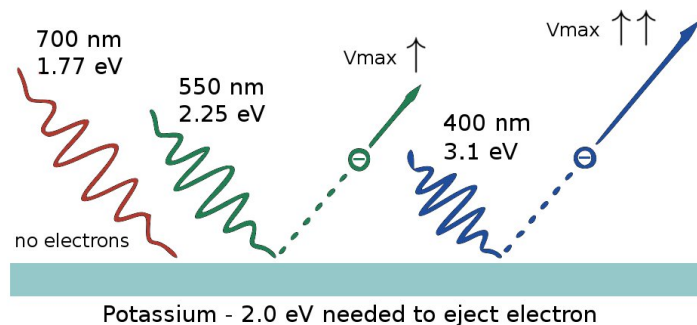


Figure 2.3: Diagram showing the dynamics of the photoelectric effect.

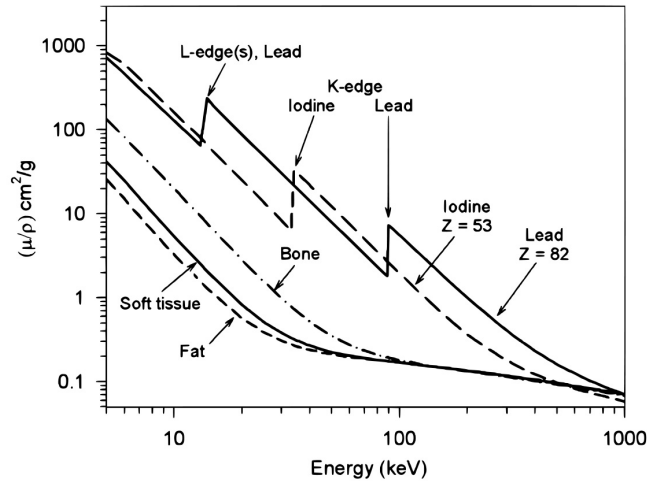


Figure 2.4: Diagram showing the linear attenuation coefficient as a function of the energy. Different materials are analysed.

was worth the Nobel prize to Albert Einstein in 1921. The photoelectric effect occurs when a photon (belonging to a mid-low energy range) releases all its energy hitting an electron of an inner shell that will be ejected after the collision. The energy of the incident photon needs to be higher than the work function of the material to allow the electron to escape with a kinetic energy proportional to the energy in excess. Since the energy of the photons is only depending on the frequency of light, increasing the intensity of the incoming light won't change the energy of the ejected electrons, but only their number. After the impact, fluorescence also occurs since an orbital electron relaxes to its ground state by emitting a light photon, which is usually absorbed because of its low energy; the ejected electron instead, usually hits other electrons causing subsequent ionizations but eventually it will be absorbed as well.

In figure 2.4 the linear attenuation coefficient is plotted for different materials, usually involved when considering shielding or nuclear medicine applications.

$$\mu'_{\text{photoelectric}} \div \frac{Z^n}{E_{\gamma}^3},$$

where Z is the atomic number of the material, and n varies between 4 and 5 over the γ -ray energy region of interest [6]. μ' is related to the energy of the photons and it is characterized by a decreasing trend: whether the incident photon is too energetic, the probability of the electron to be removed drops rapidly to the next *edge*, where the energy level is enough to eject the particle from the corresponding shell.

Compton scattering

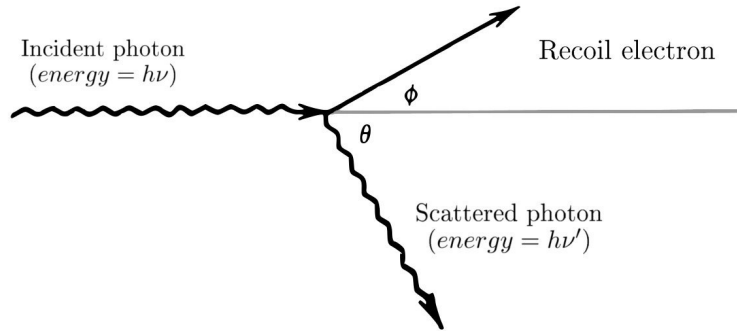


Figure 2.5: Diagram showing the dynamics of the compton scattering.

Compton scattering can be represented as an anelastic collision, according to the laws of classical mechanics, thus energy is conserved as well as momentum. The diagram in figure 2.5 shows how compton scattering works: an incident photon hits an electron weakly bound to the atom, losing part of its energy and deflecting its own trajectory. The energy of the scattered photon, $h\nu'$ is given from the following formula:

$$h\nu' = \frac{h\nu}{1 + \frac{h\nu}{m_0c^2}(1 - \cos\theta)},$$

where θ is the deflection angle from the initial direction. The statistical distribution of the trajectories $\frac{d\sigma}{d\Omega}$ depends on the energy of the incident photon and it is calculated with the Klein-Nishina formula, which won't be discussed here. As a conclusion we should underline that this contribute to the linear attenuation coefficient is proportional to the density of the material:

$$\mu'_{compton} \div Z,$$

since the number of electrons that might be involved in the collision increases along with the number of atoms in a given volume unit.

Compton scattering is one of the main factors that affect imaging systems leading to a visible worsening in the reconstructed images and spectra: γ -rays emitted by the inner source are deflected while travelling through tissues, making them difficult to be detected and read in the correct way.

Pair production

Pair production is a phenomenon that may occur whenever the incident photon has an energy value higher than $2m_0c^2 = 1.022MeV$, that is the rest mass energy of the electron and its antiparticle, the positron. In that

case, a pair formed by an electron and a positron may be produced, usually in the neighbourhood of a nucleus that is essential to the conservation of momentum since the photon energy might not be enough to provide the particles with the adequate kinetic energy. However, pair production effects are negligible in nuclear medicine since they're dominant in a high-energy range, while the typical sources used for diagnostic applications are usually far less energetic and they're absorbed thanks to the photoelectric effect. A diagram of the absorption mechanisms is shown hereafter (figure 2.6). Other phenomena are also involved, like coherent scattering and Auger effect, but they're not significant in the energetic range considered in nuclear medicine activities.

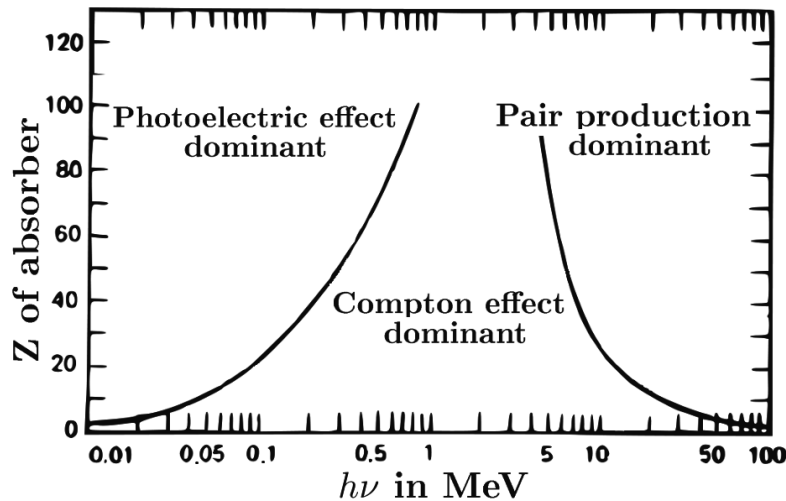


Figure 2.6: Diagram showing the absorption mechanisms as a function of the energy of the incident photon and the Z of the material.

2.2 Principles of radiation detection

After having presented the main traits of radiation, we will now give an outline of how it can be detected and read, pointing out all the goals that need to be achieved. The detection of X -rays and γ -rays is based on two main objectives: the first is to stop the radiation and the second is to convert the energy released by the photons in the detector into an electrical signal that will be processed by an electronic read-out apparatus. Other information may also be obtained, like the interaction point or the instant of the collision, in case imaging or timing specifications were significant as well.

The simplest solution, and actually the most accurate one, would involve a detector which converts the radiation directly into electrical charge, collected in a specific electrode read by the pre-amplifier. Silicon is a suitable

material but is not very efficient: gamma photons belong to a high-energy range and most of them pass through the detectors, which are not able to stop them because their thickness is limited by technological specifications and the material itself is not very dense too.

Otherwise, it is possible to convert the initial physical quantity into another one, and only afterwards it is converted into an electrical signal. That's what usually happens in common gamma-cameras: γ -photons are converted into visible photons with a scintillation crystal and the light produced is detected by an array of photodetectors. The main advantage of this kind of setup is the higher efficiency, even if the cascade of two processes leads to a worsening of the statistical resolution.

2.2.1 Architecture of a gamma camera

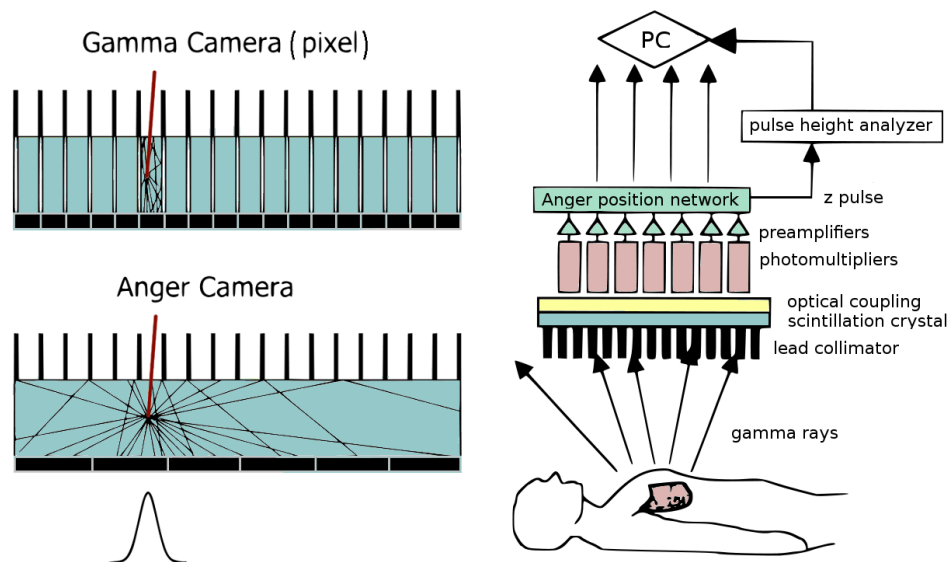


Figure 2.7: Diagram showing the structure of an Anger Camera.

Gamma cameras can be analysed following the two most known designs: a pixel structured gamma camera and the *Anger camera*, invented by Hal Anger in 1957. In the Hicam project the Anger architecture is chosen, and it is represented in the diagram figure 2.7. Most of the gamma rays coming from the patient are filtered thanks to a lead collimator, while the others are absorbed in the scintillation crystal, coupled to an array of photodetectors. The following stage is specific for the processing of the signals: the preamplifier collects the data that will be used to calculate the coordinates of the interaction point and the energy of the event. In our project Silicon detectors are implemented rather than photomultiplier tubes and the processing is made via software thanks to a DAQ board. Pros and cons of this kind of

setup will be discussed later on, analysing worsenings and improvements of the performances of the camera, considering both imaging and spectrometry.

2.2.2 Detection efficiency

Efficiency is the parameter that shows the fraction of γ -rays detected, usually expressed as a percentage, in relation to the total number of photons available emitted by the source. Total efficiency is the product of three different contributors: geometrical efficiency, absorption efficiency and photopeak efficiency.

$$\eta_{tot} = \eta_{geometrical} \cdot \eta_{absorption} \cdot \eta_{photopeak}.$$

Geometrical efficiency

Geometrical efficiency represents the fraction of the emitted photons that actually hit the detector. Efficiency gets higher increasing the area of the detector (A) and decreasing the distance from the source (d). In fact the solid angle Ω is given by the following formula:

$$\Omega \approx \frac{A}{d^2}.$$

The approximation is valid if the source is placed at a significant distance.

$$\eta_{geometrical} = \frac{\Omega}{4\pi},$$

where 4π is the whole solid angle available.

Absorption efficiency

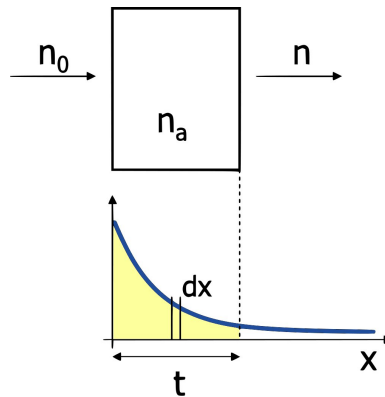


Figure 2.8: Schematic representation of the absorption efficiency.

Absorption efficiency represents the fraction of the photons hitting the detector that are actually absorbed. In figure 2.8 a schematic representation of the mechanism is presented, where n_0 is the total number of incident

photons, n_a are the photons absorbed and n are the escaping ones. As previously shown, the probability of a photon to be absorbed is an exponentially decreasing function.

$$p(x)dx = A_0 \cdot e^{-\mu x} dx,$$

where A_0 is a constant that can be easily calculated: as a probability function, its integral must be normalized to 1 meaning that if we consider an hypothetical infinitely thick detector, all the photons would be absorbed; resolving the equation we found out that $A_0 = \mu$. Thus absorption efficiency is calculated as follows:

$$\eta_{absorption} = \int_0^t p(x)dx = 1 - e^{-\mu t}.$$

Photopeak efficiency

Photopeak efficiency or full-energy peak efficiency represents the fraction of detected photons whose energy is fully converted into electron kinetic energy [6]. Generally, the photons absorbed thanks to the photoelectric effect are fully converted, except for those cases in which fluorescence photons manage to escape; the energy of scattered photons instead, may be absorbed only in a partial way, leading to a loss of signal and a spread in the spectrum. The detector should be designed in order to maximize the probability of a Compton scattered photon to be absorbed.

2.2.3 Interaction in the detector

From now on we will consider a system based on an indirect conversion process, like the Anger camera architecture.

Silicon in fact is suitable as a detector but it is efficient in a limited energy range, that is (10–30KeV); furthermore it is not possible to increase the thickness indefinitely because the voltage needed to bias the detector (in order to deplete the junction) would be too high ², since $V_{depl} \div (thickness)^2$.

Germanium instead is more efficient than Silicon due to its small energy gap, that makes it impossible to use such a material as a photodetector unless it is cooled down to 170K, which is a difficult operative condition to reach.

Gas detectors are inherently less efficient than semiconductors but they could be designed according to more flexible structures. In order to gain more efficiency, thickness could be increased up to several centimeters, making it possible to use these detectors for low-energy X-ray applications.

²For example, for a detector 1cm thick an approximate bias voltage of $\approx 40KV$ is needed.

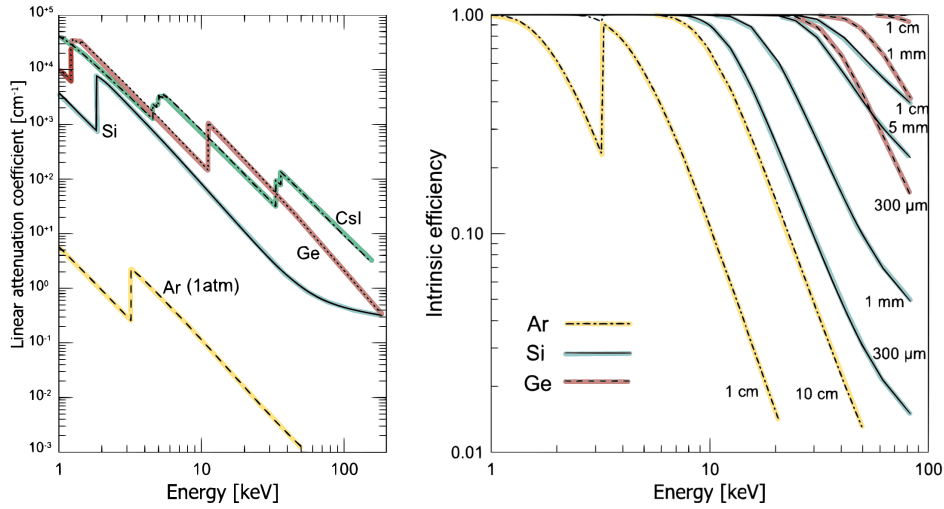


Figure 2.9: Linear attenuation coefficient and efficiency for Si, Ge, Ar and CsI.

In our project an array of Silicon photodetectors is coupled to a *scintillation crystal*, taking advantage of the intermediate conversion that allow the γ -rays to be converted into visible light. In these materials (e.g., *CsI*, *NaI*, *LaBr₃*) ionization may hardly occur, but nonetheless they're often chosen because of their great efficiency.

The efficiency trend and the linear attenuation coefficient of all these materials are shown in figure 2.9.

The amount of charge generated in the detector is proportional to the energy of the incident photon:

$$Q = \frac{q \cdot E}{\epsilon},$$

where q is the electrical charge of the electron. ϵ is a constant factor, used as a figure of merit to confront different types of sensors: it is approximately independent of the energy and the physical mechanism of the absorption, since it is proportional only to the total energy released in the detector. ϵ affects sensitivity, the minimal quantity of energy detectable, and it depends on the material considered.

2.2.4 Performances and objectives

The main goal of a gamma camera, as well as any imaging system, is to achieve good performances in terms of *spatial* and *energy resolution*, as already mentioned before. Both these objectives are deeply affected by the total amount of charge generated and subsequently collected; for this very reason the factor ϵ and all the phenomena that occur inside the detector must be seriously taken into account in every step of the processing of the data.

Energy resolution

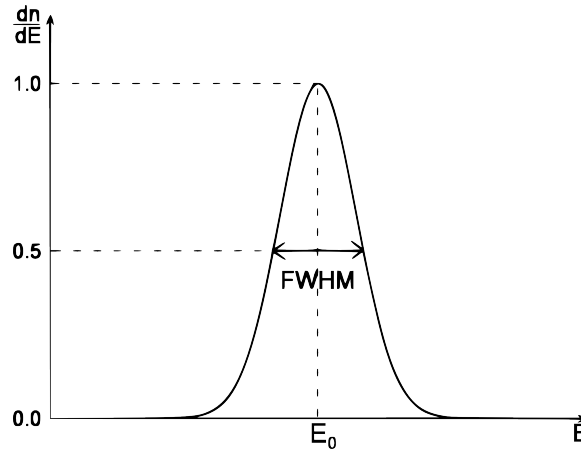


Figure 2.10: Normalized energy spectrum.

Energy resolution is one of the most important target of our system because it represents the accuracy of the measurement of the energy: in medical exams it's very important to have a high resolution to reject scattered photons whose deflection is represented by a subsequent loss of energy. From a mathematical point of view, the resolution is the width of the spectrum ΔE divided by the energy in correspondance to the peak E_0 . The spectrum in fact can be fitted to a gaussian distribution, where the centroid is generally aligned to the peak and the width is calculated as the *full width at half maximum* (FWHM).

$$R = \frac{\Delta E_{FWHM}}{E_0}.$$

$$\Delta E_{FWHM} = 2.36 \cdot \sigma,$$

A detailed analysis regarding the evaluation of energy resolution is presented in chapter 4.

Spatial resolution

Spatial resolution is the accuracy of the location of the interaction point. In case a discrete detector is used, the resolution is given by the dimension of the pixel; in our gamma camera instead, according to the Anger architecture, a continuous detector is used and the coordinates of the interactions may change over the whole surface of the detector. The *point spread function* is the response of the system to a pointlike collimated source and it should be a 2D delta in an ideal case. The actual response is a 2D gaussian distribution

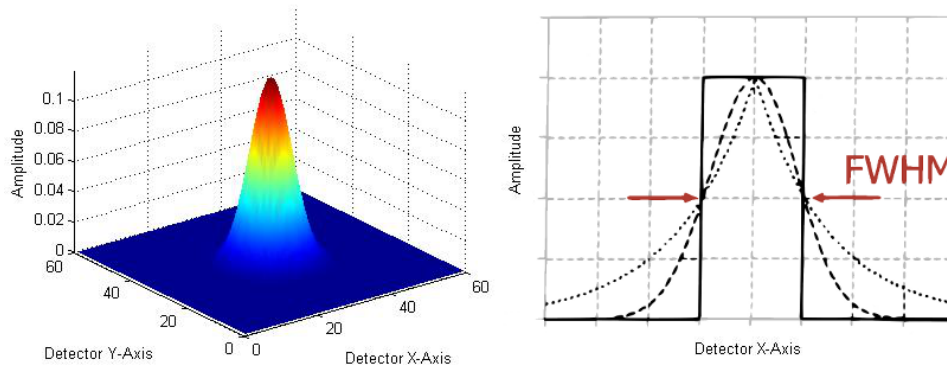


Figure 2.11: Typical point spread function and calculus of the spatial resolution.

and the resolution is calculated as the FWHM³.

Among some other features that are involved in the calculus of the spatial resolution, the fluctuation of the collected charge is one of the most important. Statistical noise affects the detection and it can't be excluded, but it could be considered insignificant if the signal collected were far higher. All the algorithms used for a further reconstruction are deeply affected by electronic and statistical noise, resulting in a blurry image, so it's important to maximize the charge generated and collected in the detector to have good images, as well as accurate information about the energy spectrum.

It's important to point out that in our case an indirect conversion method was chosen. The system is thus formed by the cascade of two detectors in two different stages: the incident γ -rays are converted into visible photons by the *CsI* scintillation crystal which is coupled to an array of Silicon photodetectors that convert the light into electrical charges. These two step are necessary to have a good detection efficiency, as already said, but they represent a worsening contribute when considering statistical noise because fluctuations are introduced in both of the stages and the conversions are not ideal.

2.3 Electronic read-out

The analysis of the data collected in the detector is carried out thanks to an electronic read-out stage, implemented via hardware solutions, and a

³The parameter which best represent the resolution is the FWHM because two different sources can be separately resolved only if the distance between them is at least equal to their FWHM.

further digital processing stage made via software, after the signals have been converted with a custom DAQ board. The main objective is the measurement of the electrical charge, proportional to energy of the radiation absorbed, and in some peculiar application also the timing of the event. The most important steps of the electronic read-out will be shown hereafter, while the role of the electronic boards and the developments of the algorithms will be discussed in the next chapters.

Charge pre-amplifier

The front end of the electronic chain is typically a charge amplifier. In figure 2.12 the circuit implemented in the Hicam gamma camera is depicted. This configuration is particularly suitable when the chosen detector is the *Silicon Drift Device*, which will be presented in the next chapter. In this case, the feedback capacitor C_{a-ig} and the reset diode are integrated in the detector, providing compactness to the system since no external elements are placed outside the chip.

This stage is introduced to convert the charges collected into a voltage level to avoid worsening the signal-to-noise ratio. The FET is integrated too, in order to reduce the parasitic capacitance at the anode.

The preamplifier is designed with two feedback loops: the first one is a classical operational amplifier featuring an inverting configuration, while the second one makes use of a parasitic capacitance of the detector, which is C_{a-ig} , located between the anode and the inner guard. In operative conditions (medium frequencies), C_{in} is a short circuit, forcing V_s to virtual ground. The external loop works to reduce the error signal V_{gs} , pulling the

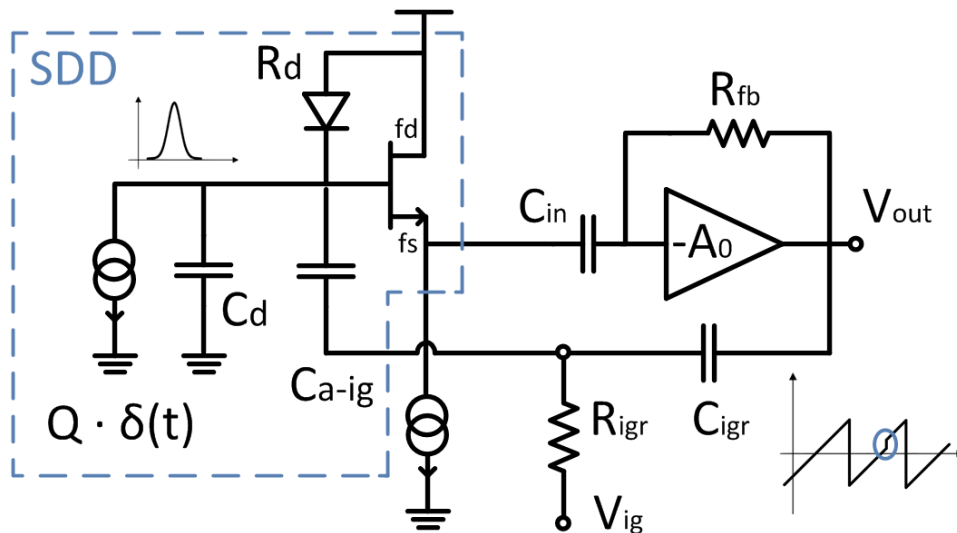


Figure 2.12: Charge preamplifier configuration in the Hicam system.

gate voltage to ground level. The current of the detector is thus forced to flow into the capacitive feedback path, resulting in a subsequent voltage V_{out} at the output contact.

R_{igr} is introduced to bias the guard ring, while C_{igr} is essential for a DC decoupling between the output and the inner guard ring itself.

The output current has two contribution: the signal associated to a gamma event, and leakage current. For this reason, detectors must be reset periodically, in order to avoid the saturation of the output of the preamplifier. The reset frequency is proportional to the leakage current of the detector and inversely proportional to the output dynamic range of the preamplifier. The output voltage V_{out} is expected to be a series of ramps, with the addition of small steps, which represent the useful signal.

Shaping filter

The *shaping filter* transforms the output signal of the pre-amplifier, approximated to an ideal step, into a gaussian impulse. Actually the signal is converted back into an ideal impulse thanks to a derivative stage and then converted into other waveforms. If we consider that the only source of noise is given by white noise, the matched filter to maximize the SNR would be a cusp form, which is not achievable with real analog filters, as demonstrated in more detailed studies [7, 8]. The gaussian shape though, is not achievable using only passive components: a simple solution may involve a semigaussian filter with real poles implemented with a CR - RC^n chain.

The characterization of the filter is based on the following coefficients: A_1, A_2, A_3 , which affect only the shape of the output impulse of the filter, and τ , also known as *shaping time*, that is linked to the width of the impulse. The value of τ is generally programmable and it is calculated to minimize the electronic noise that affects the sensitivity of the whole system.

As already mentioned in the previous paragraph, it would be better to have a short transient phase in the amplifier output signal: if it is too long in fact, the impulse generated from the shaping filter will be wider and smaller in amplitude, leading to a worse signal-to-noise ratio. A more detailed analysis of these aspects will be carried out hereafter.

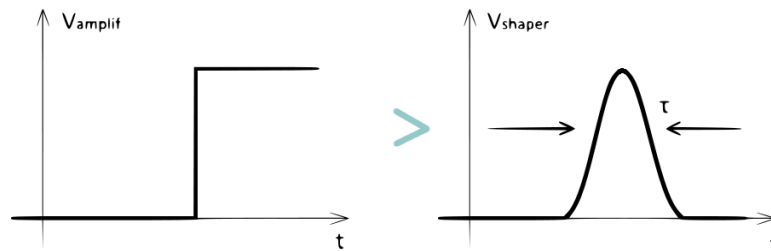


Figure 2.13: Conversion of the signal in the shaping filter.

Pile-up rejector

When the count rate is high, it may occur that close events are detected in a short time period leading to an overlap of the pulses generated by the shaper. This is a misleading situation since the amplitude of the signals may be corrupted, so they need to be detected and then rejected: for this very reason a *pile-up rejector* is introduced to create an inhibition window in which no more events are accepted. This method leads to a smaller rate of the output pulses but it allows a more accurate measurement. A possible solution may be the implementation of a different filter characterized by a shorter τ , which should be however feasible according to other specifications.

Baseline holder

The *baseline holder* (BLH) is an element introduced to achieve an AC decoupling and stabilize the baseline of the output signal of the shaper, for example to ground level, even if there are other DC voltage levels that are slowly variable in time (variations may occur because some parameters such as leakage current are not constant). In the Hicam project, an improved solution involving a non-linear buffer is used to reduce the expected baseline shift due to variations in the count rate [9].

Peak stretcher and multiplexer

The last part of the analog electronic chain is the *peak stretcher*, used to hold the peak value of the pulses to allow the analog-to-digital (ADC) converter to process the incoming data. At the same time it's important for the BLH to hold the DC baseline value as well to carry out a correct measurement.

Another element may be included in the electronic chain as a back-end: a *multiplexer*. In some cases, like in the Hicam project, it is necessary to have a multiplexer because there are several channels that need to be read in sequence; all the signals coming from the peak stretchers (one for each channel) are sampled in a single serial signal which will be read by a DAQ board. Analog signals are converted into digital ones and then sent to the PC where a custom software has been developed to save and process them both online and offline [9].

Chapter 3

Structure of the Hicam system

“The best performance improvement is the transition from the nonworking state to the working state.”

John Ousterhout

After having shown the most significant features of a generic gamma camera system, in this chapter we will show the solutions implemented in the Hicam system with a particular focus on the repercussions of the choices made, analysing which kind of improvements may be developed to achieve the goals established beforehand.

All the parts will be now investigated starting from the point where the γ -rays first interact, concluding with the final part where the results of the analyses are shown and discussed.

The *Hicam project* involves two different prototypes which are actually working: the first one is made of 25 detector (aligned in a 5×5) matrix, while the second one is made of 100 detector (aligned in a 10×10) matrix.

The bigger prototype has been developed because an extended active area was necessary to carry out measurements (such as thyroid scintigraphy) with real patients. However, the structure of the system makes use of a modular design, allowing us to arrange interchangeable pieces in the setup working with both the gamma cameras. In the following descriptions both the implementations will be presented.

3.1 Gamma camera

The first part of the detection process takes place in the gamma camera itself, where the energy of the photons is converted into an electrical signal. The elements involved are listed hereafter: the collimator, the scintillation crystal and the detector array.

3.1.1 Collimator

Medical imaging techniques are based on the correlation between the initial position of the radioactive source in the patient's body and the reconstructed point computed with the detection system. However, radiation is spread in an isotropic way and it's impossible to determine the direction of the incoming photon only from the distribution of the collected charge; the solution is to detect only the photons that come from a given direction with a collimator, a thick layer made of a very dense material, usually lead or tungsten, in which small holes are drilled. In this way a remarkable difference is noticed in terms of efficiency, because a lot of photons are absorbed in the collimator, therefore the dose of radioactive tracer injected in the patient needs to be increased.

Collimators may be designed in different shapes: in the Hicam project two types are evaluated. A *parallel hole* collimator is designed as a matrix of contiguous holes, all of them having the same orientation, orthogonal to the surface of the scintillation crystal; no magnification of the image is obtained. A *pinhole* collimator is designed to achieve a great magnification of the image, thanks to a single small hole, and it is often used to examine small organs.

The evaluation of the performances of a collimator is carried out thanks to two figures of merit: *spatial resolution* and *geometrical efficiency*. These parameters are strictly depending on the geometrical dimension of the collimator:

- a is the diameter of the hole (in case of an hexagonal shape it represents the distance from side to side). $a = 1.2mm$.
- s is the thickness of the septa. $s = 0.2mm$.
- l is the height of the septa. $l = 45mm$.

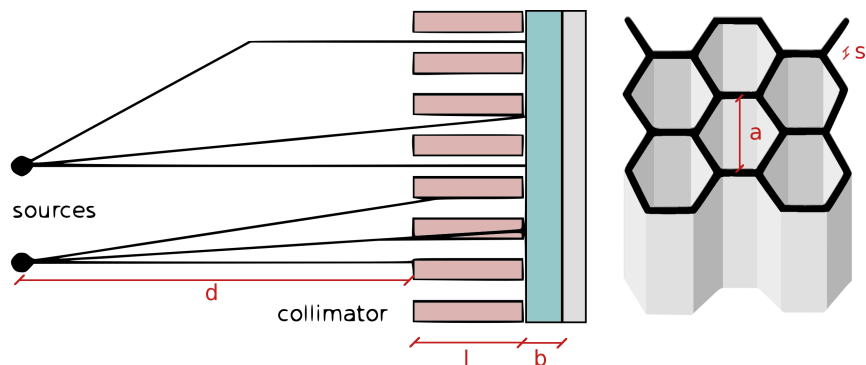


Figure 3.1: Impact of the collimator on the detection efficiency and diagram of its inner structure.

- d is the distance between the source and surface of the collimator.
 $d = 50mm$.

Spatial resolution The spatial resolution is the capability of the collimator to tell two close points apart. It is one of the fundamental contributors to the global spatial resolution and it is indicated by the following formula, valid for a parallel hole collimator:

$$R_c = \frac{a(d+l+b)}{l} = 2.8mm, \quad (3.1)$$

where $b \approx 10mm$ is the distance between the lower surface of the collimator and the detector level, since the scintillation crystal is located in between.

In the Hicam project a high resolution R_c is required to avoid worsening the spatial resolution of the detectors, which is about $0.85mm$. The total resolution is calculated as the quadratic sum of the two contributors.

In the design of a collimator, the thickness of the septa must be taken into account, since it is responsible for obliquely incident photons not being stopped.

Geometrical efficiency The geometrical efficiency represents the fraction of photons that travel through the collimator and hit the scintillation crystal, considering a pointlike source that send radiations out in an isotropic way. Efficiency, E_g , is proportional to the available area (through which the photons can reach the detector) divided by the total area of the device:

$$E_g = G_o \frac{A_{open}}{A_{total}} = \left(\frac{\sqrt{3}}{8\pi} \left[\frac{a^2}{l(a+s/\sqrt{3})} \right]^2 \right) \cdot \frac{A_{open}}{A_{total}} = 73.74 \frac{cpm}{\mu Ci},$$

where G_o is a parameter depending on the shape of the holes since it represents the solid angle subtended by the surface of the collimator ¹.

It's thus necessary to find a trade-off for the dimensions: to achieve a good spatial resolution, it would be better to have small holes, while we should design bigger holes if a more efficient detection is requested.

For the Hicam project both a parallel hole and a pinhole collimator are now available for the small prototype and for big one as well. Two types of parallel hole collimator were produced: a LEUHR (Low Energy Ultra High Resolution), used to achieve an higher spatial resolution, and a LEHR (Low Energy High Resolution) which has bigger holes (a) and a smaller height (l),

¹For the Hicam gamma camera the collimators were realized by *Nuclear Fields International*. This formula is suited to evaluate performances of our device, while for other cases the manufacturer provides an online calculator [10].

available only for the bigger prototype to be used with patients, so to achieve more efficiency providing better statistic. The values previously calculated were referred to the LEUHR collimator.

The collimator is essential in a medical imaging environment, even if there are some problems because some photons may be deflected (with a significant loss of energy) due to *compton scattering*. However these photons may hit the detector and be reconstructed in a wrong location since they don't correspond to a source point in the patient's body, leading to a blurry and corrupted image. This issue may jeopardize the measurement and prevent a three-dimensional reconstruction from being performed, such as in SPECT applications; a simple solution could be the introduction of an *energy window*, that is a software filtering stage used to tell scattered events apart.

3.1.2 Scintillation crystal

The *scintillation crystal* is actually the first detector of the system. In fact this is the stage in which the energy conversion takes place: gamma photons, provided with high energy, are absorbed into the crystal turning into visible photons, according to the scintillation yield of the material (a simple diagram of the mechanism is shown in figure 3.2).

This step is necessary to read the signal with an array of photodetectors, which obviously cannot detect radiation such as *X-rays* or γ -rays because of their limited absorption efficiency.

In Hicam a continuous scintillation crystal is implemented (typical Anger architecture), so visible photons are spread in an isotropic way in the crystal itself: the projection of this flash of light is a three-dimensional bell-shaped

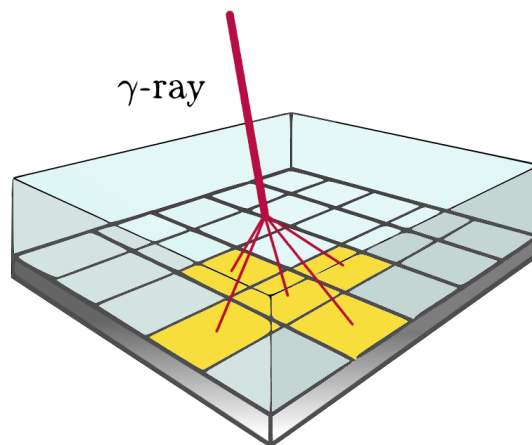


Figure 3.2: Diagram showing how high-energy photons are converted into visible photons.

distribution on the detector layer. Actually the crystal is coupled to the detectors thanks to a thin layer of optical grease, that is useful to remove air bubbles and keep the two pieces together.

There are a lot of figures of merit that need to be considered when choosing a scintillation crystal for a specific project; some of the most significant are listed hereafter:

- *Wavelength*: it's important to consider the wavelength of the visible photons emitted to have the correct coupling between the crystal and the photodetectors, which are suitable to detect photons in a given range.
- *Refractive index*: total reflection and light transmission through optical grease are deeply affected by the refractive index of the crystal. A detailed analysis of these aspects is carried out in the next chapters.
- *Decay time*: it's the time necessary for the conversion. The flash of light is not a pulse, it has a decreasing exponential waveform that is dependant on the physical characteristics of the material. This parameter is deeply affected by temperature variations.
- *Light yield*: represents the number of visible photons emitted. It's dependant on the type of material and it is proportional to the energy of the incoming photon. It's usually expressed in *photons/keV*. In some cases, this parameter is deeply affected by temperature variations, leading to sensible changing in the number of photons emitted and thus in the energetic resolution achievable. Light yield is also subjected to statistical variations, according to Poisson's distribution.
- *Density*: affects the capability of absorption of the crystal.
- *Hygroscopy*: is the ability to attract and hold water molecules from the surrounding environment. It's a damaging factor since water may change the physical structure of the crystal and the impact of some other features as well.

For the Hicam system, a CsI(Tl) crystal was chosen mainly because of its great light yield equal to 54 *photons/keV*. Other features are listed hereafter: a refractive index equal to 1.79, two scintillation decay time constants equal to 1 μ s and 5 μ s, a density equal to 4.51g/cm³ and an emission wavelength equal to 550nm, which makes them suitable to be coupled with detectors covered with a Si₃N₄ anti-reflective layer, 3 μ m thick. The crystal is 1cm thick. This value is selected as trade-off: in fact, more efficiency would be gained if the crystal were thicker, but photons would be spread all over the surface of the detectors, leading to a worsening in terms of spatial resolution. Otherwise, if the crystal were thinner few photons would be absorbed and a longer acquisition time would be required.

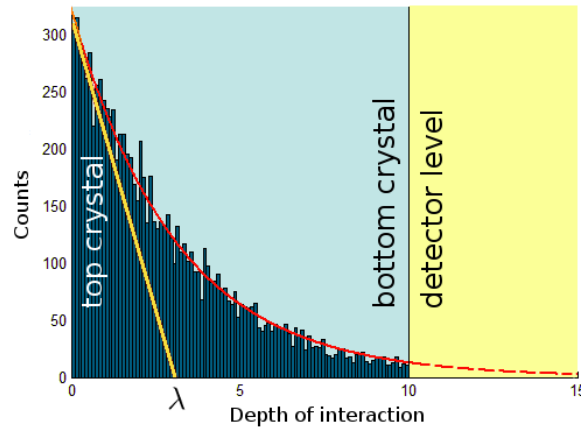


Figure 3.3: Diagram of the absorption distribution in a CsI(Tl) crystal, 1cm thick (simulated in Geant3).

In figure 3.3, a diagram of the absorption is shown, thanks to a custom software realized in *Matlab* and *Geant3*². The crystal is 1cm thick and the material chosen is CsI(Tl), and it is coupled to the detectors ignoring the thickness of optical grease. In Geant3, 10000 γ -rays are fired perpendicularly into the crystal. The histogram pictured is the absorption distribution along the Z-axis of the crystal and it actually follows an exponential curve as expected. The absorption length is $\lambda = 3.09\text{mm}$ for this simulation, resulting from both photoelectric and compton effect: a total of 9658 photons (96.6%) are absorbed in the crystal. The source simulated is ^{99m}Tc whose photons have small energy values (140keV), in fact 98.9% of them are absorbed due to photoelectric effect, as expected analysing figure 2.6.

In the Hicam system, the faces of the crystal need to be covered with specific coatings to avoid total internal reflection and deflections that cannot be reconstructed after the read-out. The lateral faces are covered with a black absorbent tape, so that most of the photons that hit the walls from the inside are absorbed; otherwise they will be detected without being distinguishable from other photons that are detected without any previous deflections. The top face instead is covered with a reflective coating, allowing to collect more charges and double the signal detected leading to an improvement in terms of energetic resolution [12] [13].

²Geant3 is a simulation software designed to describe the passage of elementary particles through matter, using Monte Carlo methods. It was originally developed at CERN for high energy physics experiments [11].

3.1.3 Photodetector array

The detector array is the fundamental stage of a gamma camera because it is the place where the conversion from light to electrical charges takes place. In common gamma camera systems, devices like *PMTs* are usually implemented; in fact, thanks to their high internal gain, they can achieve a great signal-to-noise ratio without the necessity to design a cutting edge electronic front end. On the other side, there are some negative aspects that limit the application of these devices in more complex systems: for example they're very sensitive to magnetic fields, so they couldn't be implemented in an hybrid SPECT/MRI³ system. Furthermore, they usually have a low conversion efficiency, they have big physical dimensions, preventing them from being implemented in a compact environment, and they need high voltage levels to operate.

A possible solution may be the implementation of semiconductor detectors, such as *photodiodes*, which can achieve higher efficiency values even if they're not provided with an internal gain, making the electronic stage determining in terms of noise. Among other features, *APDs* have also an internal gain, but they have other issues like replication difficulties and gain fluctuations due to thermal drifts.

SDD features

For the Hicam project, the photodetector chosen is the *Silicon Drift Device (SDD)*, studied by Gatti and Rehak in 1983 [15]. The most important characteristic of this device is the small anode capacitance, achieved thanks to a transversal field generated by a series of ring electrodes: this is an additional feature to the classical depletion region of a *pin* semiconductor, causing charge carriers to drift to a small collection electrode with high detection efficiency. About 70 *rings* are arranged in a concentric way and biased with increasing negative voltage moving outwards. The anode is made with an inner implantation, next to the rings, and it is forced to ground level. In the middle of the detector, an integrated FET is installed: it is the first stage of the pre-amplifier and it is linked to the anode with a small metallic strip, in order to limit parasitic capacitance and achieve a better matching between gate capacitance (C_g) and SDD depletion capacitance (C_d)⁴. This

³A similar apparatus could provide a greater depth of data about a host of biologic processes and anatomic information including soft-tissue contrast, which is important for many diagnoses. The acquisition of fused images can provide meaningful information for brain studies, heart imaging and a range of other applications useful to improve patient care [14].

⁴A more detailed analysis about noise performances will be carried out afterwards, demonstrating why C_g and C_d should have similar values.

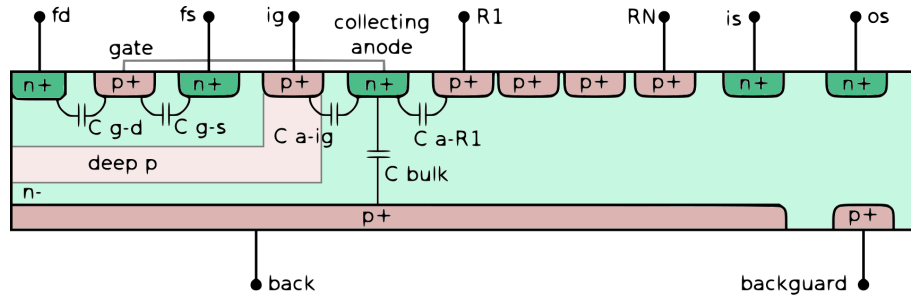


Figure 3.4: Diagram of a single SDD. The contacts of the detector are shown as well as the integrated FET.

solutions allow to design a detector with a large active area and a small anode capacitance, resulting in a better signal-to-noise ratio.

In figure 3.4 a diagram of a single SDD is shown: the role of the contacts will be explained hereafter:

- *Back*: it is the largest contact, placed on the top surface, where the photons hit the detector. It's made with a homogeneous $p+$ well, biased with a high negative voltage level being responsible for the depletion and the overall functioning of the device.
- *Ring1 and RingN*: *Ring1* is the first ring and it's located next to the anode, in the inner part of the detector. It is biased with a small negative voltage. *RingN* is the last ring, placed in the outer part of the detector. It is biased with a high negative voltage. All the other rings included in between are biased with proportional voltages, thanks to a resistive divider. The rings are implanted as $p+$ wells, and they're responsible for the drift electrical field.
- *Backguard*: it is the ring that surrounds the Back contact. It's forced to a higher voltage level since it acts as a protection to the device, and it is necessary when several SDDs are aligned.
- *Inner substrate and outer substrate*: they are bulk contacts, both forced to ground level.
- *Inner guard ring*: it allows the integrated FET to be electrically isolated from the rest of the device that works with several high voltage levels.
- *FS*: it is the source of the integrated FET.
- *FD*: it is the drain of the integrated FET.
- *RD*: it is the *reset diode*, an integrated device used to remove collected charges due to signal and leakage current.

Thanks to these contacts some measurements have been carried out to analyse the functioning of devices, using a *Semiconductor analyser*. Some of the characteristic curves are shown in the graphs of figure 3.5 and figure 3.6.

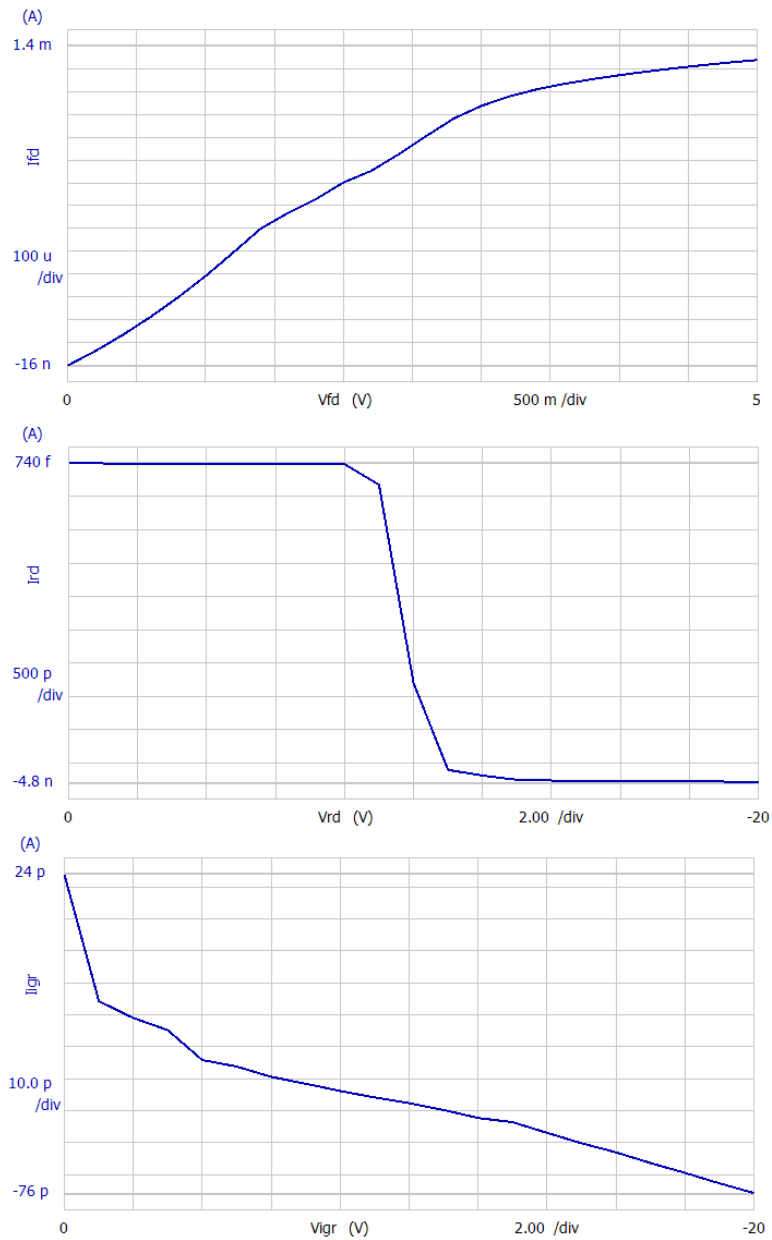


Figure 3.5: The first picture is the trend of the drain current of the integrated FET as a function of the voltage between source and drain. The second picture is the current flowing in the reset diode, after a significant voltage is applied. In the third picture the depletion current of the inner guard ring is plotted.

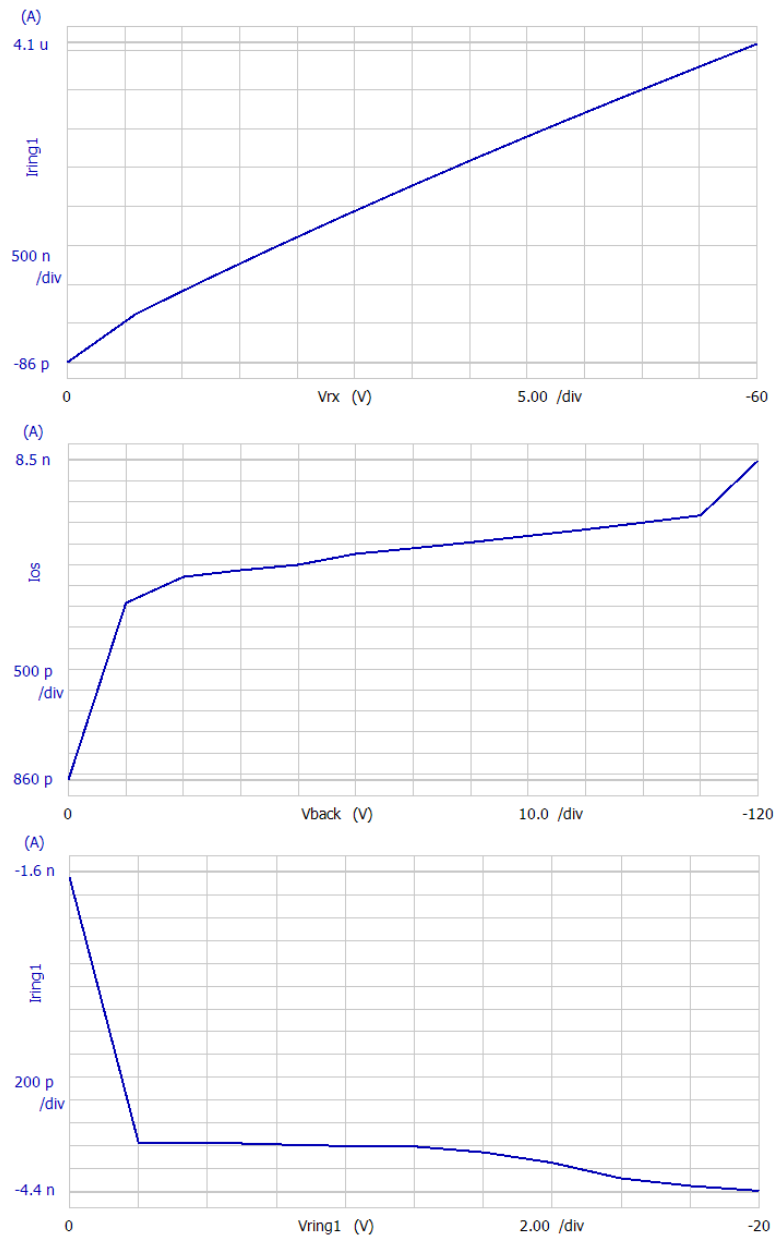


Figure 3.6: The first picture is the current flowing from Ring1 to RingN, increasing the voltage difference in between them. The second picture shows how the detector is depleted increasing the negative voltage level of the Back contact. In the third picture the depletion current of the first ring is plotted.

SDD design and implementation

For this gamma camera, SDDs are designed to form monolithic modules, each made of 5 detectors, which are assembled in larger matrixes composed of 5

modules (small prototype, called Hicam25) and 20 modules (big prototype, called Hicam100).

The detectors are square-shaped and the area of each one is 1cm^2 . The thickness is limited by silicon wafers, which are about $300\mu\text{m}$ thick. This is a limiting factor in terms of absorption efficiency in the X -ray range, in fact 10keV radiations are absorbed with an efficiency equal to $\eta = 90\%$, but 15keV radiations are absorbed with an efficiency equal to $\eta = 50\%$. As a conclusion, SDDs can be used in a low energy range ($E_{ph} < 10\text{keV}$), for example with a ^{55}Fe source, where photons are absorbed because of direct ionization; otherwise, with higher energy values, an indirect conversion process involving a scintillation crystal is needed.

The modules were designed and manufactured by Max Plank Institute of Munich. Each single module is glued and bonded to a small PCB provided with a flat cable and a specific connector. Unfortunately the material used for the PCB (FR4) is a fair thermal conductor: to cool down the detectors, 70 copper vias were made through the base that holds the module. Some pictures and photos of these features are depicted in figure 3.8.

The measurements shown in the previous paragraphs, were carried out for every single detector of each module to ensure that modules hadn't been damaged during shipping or while being arranged on the base. Once having

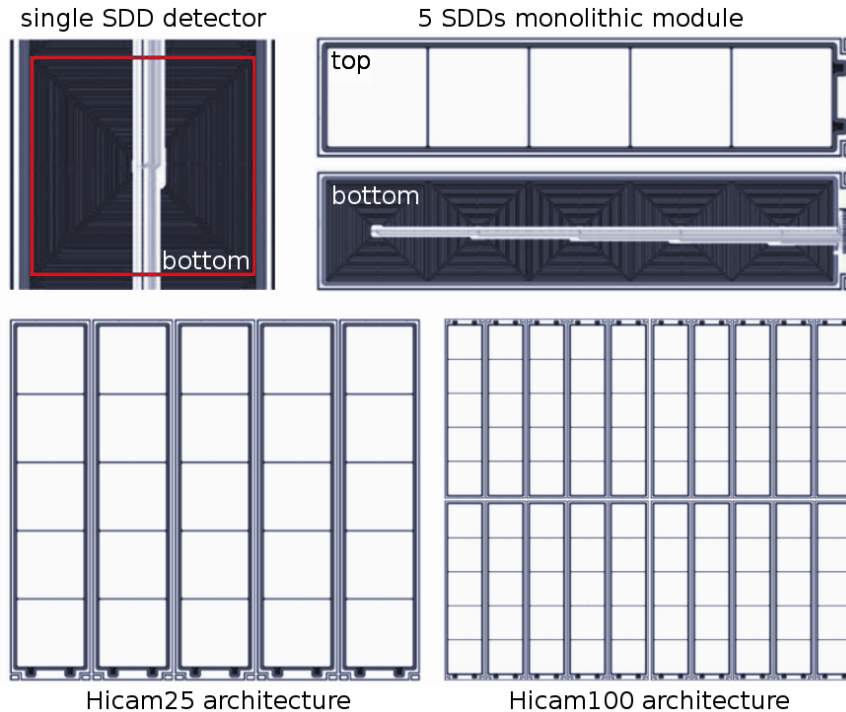


Figure 3.7: Detector layout for both Hicam25 and Hicam100. The active area of a single detector is outlined in red.

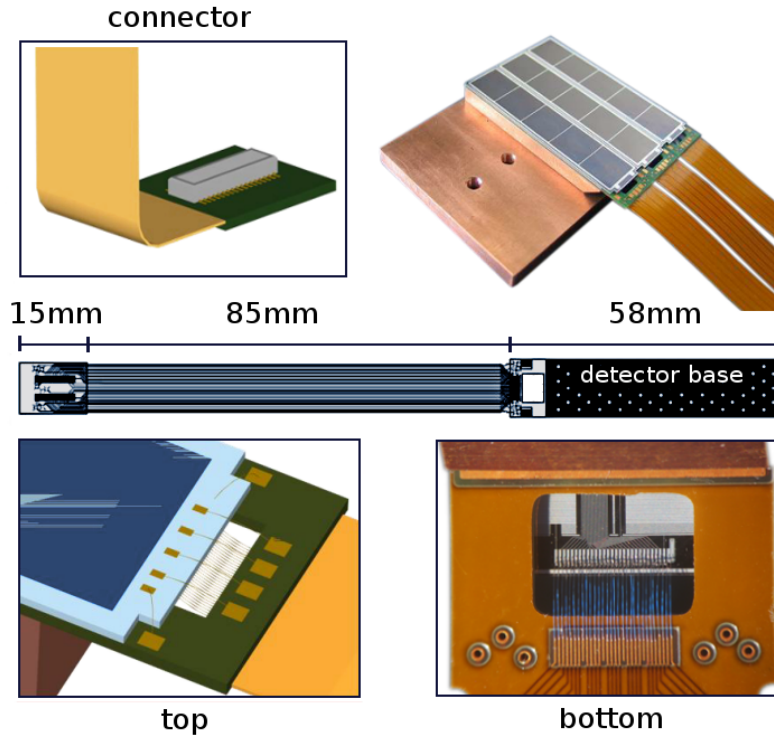


Figure 3.8: Features and dimensions of the flex PCB and its connector. In the top-right corner a photo of the modules is shown, while on the bottom-right corner there is a photo of the bondings on the bottom of the PCB.

checked that all the detectors are properly functioning, there is another important step that needs to be taken, that is the setting of the voltage levels necessary to deplete the device and detect incoming photons. The electrical charges generated in the detector travel to the anode following a given trajectory, according to the bi-dimensional electrical field that drives the particles where potential energy is lower. However, even if the voltage levels can be calculated a priori to drive the charges along the optimal trajectory, there are significant differences in the physical structure of the detectors, due to manufacturing imperfections. For this reason a specific setup has been developed to carry out a manual tuning in order to bias the Ring electrodes with the correct values. During these tests, a ^{55}Fe has been placed upon the detector level before the scintillation crystal was installed: radiations coming from ^{55}Fe in fact, show a 2 – peaks spectrum in a low-energy range (5-6keV), allowing direct conversion absorption. Operating this way, the energy of a single event is absorbed in a given detector and there is no charge sharing with any others (this would be very likely using a scintillation crystal). The setup was arranged featuring an external preamplifier, an external shaping filter, an oscilloscope and other measurement tools, and a special board de-

signed to change voltage values with variable resistors and check how the detection is affected using a MCA system connected to a PC, showing the source spectrum. Once an optimal combination for each module has been reached in this temporary setup, it will be replicated in the real system so to maximize the charges that will be collected, in order to achieve a better energy resolution.

All these measurements were a significant part of the thesis, since the characterization and the biasing of the detectors were essential steps to be carried out on the SDDs that would have been installed on the bigger gamma camera, Hicam100.

3.1.4 Case and sealing

All the elements described are sealed in an iron case filled with *nitrogen*, necessary when the temperature goes down to -10°C : reducing humidity we prevent molecules of water from turning into ice, avoiding possible damage to the detectors. Low temperature values are required to limit thermal noise and the leakage current that corrupts the signal. The detectors are stuck onto small copper stripes, which are screwed on another copper substrate acting as a heat exchanger. This element is coupled to a *Peltier stage* used to cool down substrate and detectors, thanks to a thin layer of thermal grease.

The other side of this device warms up because of the Peltier effect, and



Figure 3.9: Picture of Hicam100 during assembling stages. All the pieces of the case are visible, except for one lateral panel and the cover.

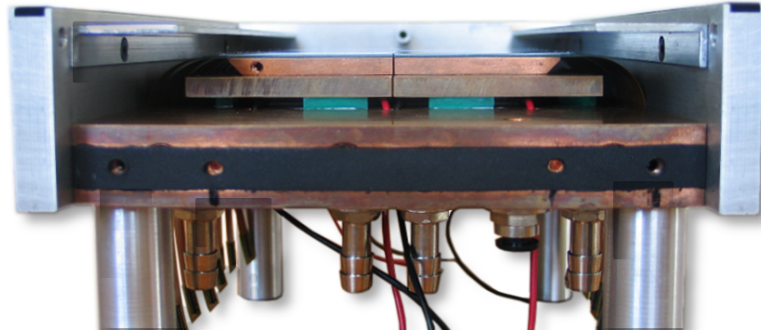


Figure 3.10: Picture of Hicam100 during assembling stages. All the pieces of the case are visible, except for one lateral panel and the cover. On this lateral view the connections for nitrogen and cooling liquid are visible.

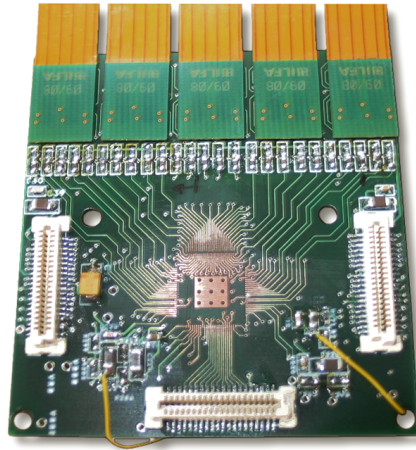


Figure 3.11: The holder board is studied to host the ASIC and bring bias voltage levels to the detectors.

the solution adopted relies on the employment of a *chiller*: this machine allows to remove heat from a liquid (water in our case), which can be circulated through the heat exchanger thanks to special hosepipes.

3.2 Holder board

The *holder board* is studied to host the ASIC which is bonded right in the middle of it; it also brings several voltage levels to the detectors and transfer the signals to the acquisition stage [16]. A picture of the board is shown in figure 3.11. The Hicam system had been designed to be a modular apparatus, in fact the ASIC can handle 25 channels: 1 ASIC is thus necessary to read 25 detectors belonging to the small prototype, and 4 of them are implemented in the bigger prototype. Each board is connected to 5 modules thanks to

special connectors and flatcables, already reported in the previous paragraph. Three connectors are placed nearby the borders to allow digital and analog communication between the holder board and the motherboard.

3.2.1 Electronic read-out

Whenever a γ -photon is absorbed in the crystal, a flash of visible light lights the detectors: an electronic read-out apparatus is arranged in order to detect and measure photogenerated charges in each SDD. The objective is to read and filter the analog signal so to reject electronic noise, and then send it to the digital acquisition. The ASIC is designed with a $0.35\mu\text{m}$ CMOS technology supporting a 25channels read-out. Each channel is formed by: a charge pre-amplifier (closed loop with a single detector), a gain stage, a shaping filter with 6 real poles, a baseline holder, a peak stretcher, an analog multiplexer and an output buffer. These elements have been studied during previous thesis works, and won't be discussed here [16].

3.3 Motherboard

The *motherboard*, depicted in figure 3.12, is the central node of the electronic system of the Hicam gamma camera. In fact, the motherboard is essential

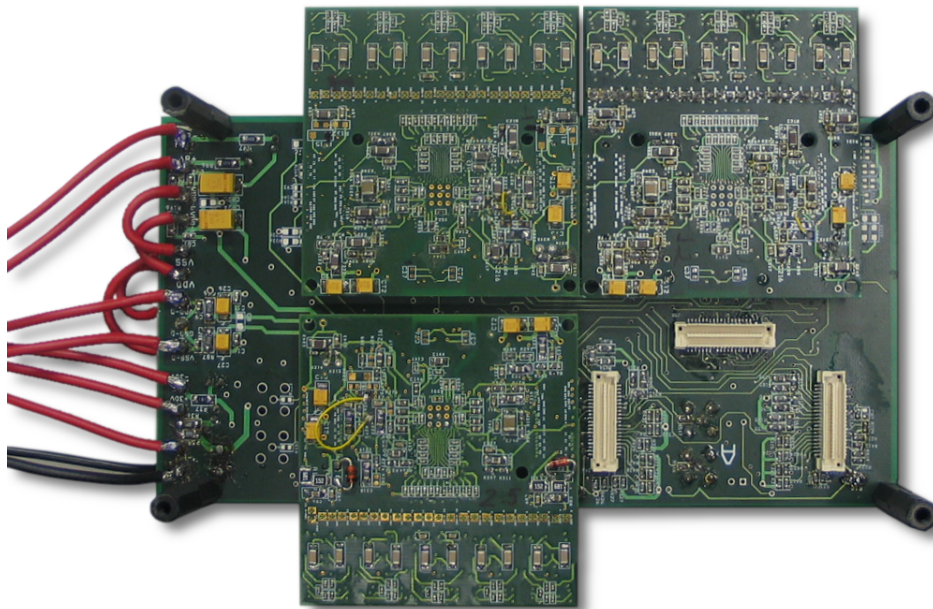


Figure 3.12: The motherboard is connected to the power supply (wiring on the left) and is designed to host up to 4 holder boards.

to convey the following signals:

- *Power supply.* The motherboard brings stabilized voltage levels to the ASICs, to the detectors and to the DAQ board. In figure 3.12, all the connections to the power supply are shown on the left side.
- *Analog signals.* Analog signals that come from the detectors, are processed by the ASICs and then transmitted to the motherboard through special connectors placed on the bottom layer. Afterwards they are carried to the ADCs of the DAQ board through several coaxial cables, 2 of them for each ASIC.
- *Digital signals.* Digital signals are necessary to carry out the programming phase before the acquisition starts. They're sent from the DAQ board to the motherboard through a flat flexible cable, and then transmitted to the holder board where the ASIC is hosted.

3.4 Data acquisition board

A customized *data acquisition board* has been developed by an external team specifically for the Hicam project. This system is made of three parts:

- *Analog interface.* This is the stage where the analog differential signals, coming out from the multiplexer and through coaxial cables, are actually converted into digital signals by the ADCs.

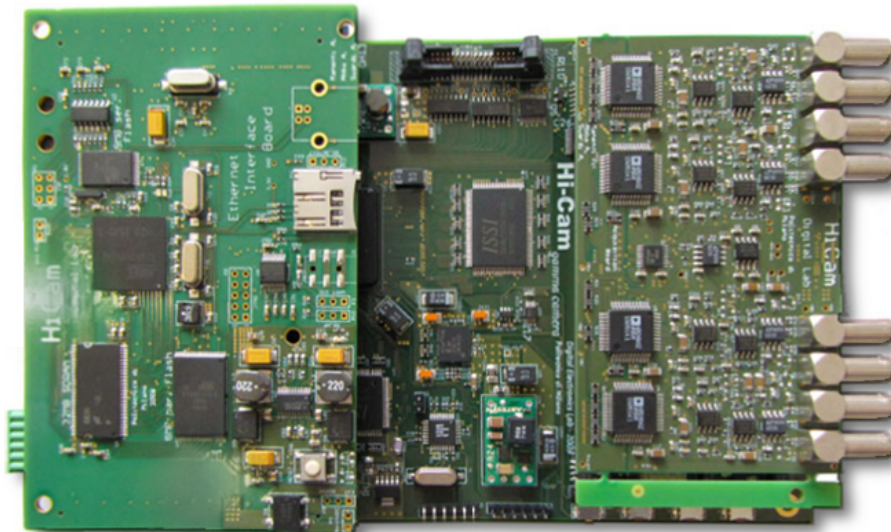


Figure 3.13: The digital acquisition board is formed by three different interfaces all plugged in together.

- *Ethernet interface.* This is the part of the system that actually communicates with the PC, dealing with the transmission of the data.
- *Main Board.* On the main board an FPGA is installed, whose task is to manage the phase in which the ASICs are programmed. The user can control the programming features from a *graphic user interface (GUI)* on the PC, therefore digital signals are sent to the integrated circuit passing through the motherboard.

3.5 Acquisition and reconstruction software

In the previous paragraph we did mention that the user can control the parameters of the programming phase from a PC, working on a specific *GUI* that has been developed by the same team who designed the DAQ (these two stages in fact are strictly linked to each other). The main features of the GUI will be listed hereafter:

- Management of the programming parameters like shaping time, gain, and an option allowing to inhibit some chosen channels.
- Save of the data and management of the acquisition.
- Online display of the acquired data in a channel map and in a pre-processed reconstructed image.
- Post-processor and filtering stage to show enhanced images, corrected in energy, linearity and uniformity.
- Management of the servo motor to carry out tomographic measurements.

The first version of the acquisition software had been developed inside Matlab, while running experiments with *Hicam25*. The second version instead, developed while assembling *Hicam100*, has been realized in *C language* since it's faster and allows to reconstruct images online. However, the saved data are stored in **.mat* files because they're easily manageable and it is possible to have a immediate processing with simple softwares, even if only offline. This feature has been very important, especially in the first phases of the project, when the final software was still in development and it was necessary to analyse the acquired data to carry on with the measurements and the testing of the whole system. A screenshot of the software is reported in figure 3.14.

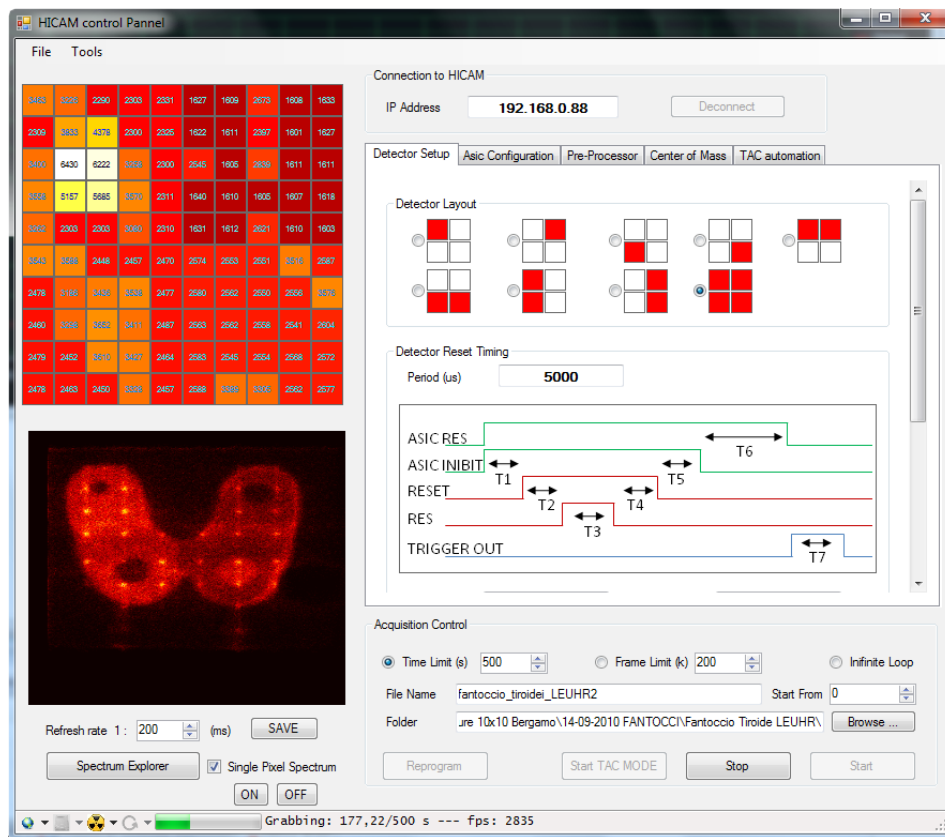


Figure 3.14: Screenshot of the acquisition software. A thyroid phantom is being reconstructed online, during acquisition.

Chapter 4

Charge collection analysis

“All models are wrong, but some are useful.”

George E. P. Box

In this chapter we will discuss the problems concerning charge collection that affect evaluation parameters like spatial resolution and energy resolution. The analysis is essential to provide feasible solutions to perform a correct reconstruction of acquired data.

4.1 Spatial resolution and energy resolution

In the previous chapters it was mentioned that spatial and energy resolution are two of the most important parameters that are generally evaluated to qualify the performances of a gamma camera. However, even if they're both dependant on the quantity of photons detected in the devices, they cannot be achieved with the same conditions: in fact a significant increase in the number of charges collected reflects in an improvement of the SNR, but it's also important not to lose the information concerning the position of the photons that is necessary to compute the coordinates of the gamma interaction. For these reasons, an absorbent coating is put on the lateral surfaces of the CsI(Tl) scintillation crystal: the implementation of a reflective coating would bring more photons on the detector level, nevertheless they would be spread all over the bottom surface corrupting the information regarding the position of the event, leading to a blurry image provided with a poor spatial resolution (an example is pictured in figure 4.1).

To tell the truth, in both the prototypes absorbent coatings are applied on the lateral surfaces, while a reflective layer is put on the top surface. This solution in fact allows to detect twice the photons without losing the spatial coordinates since symmetry is preserved. The only difference is that the reflected light is spread over a greater number of SDDs in relation to direct

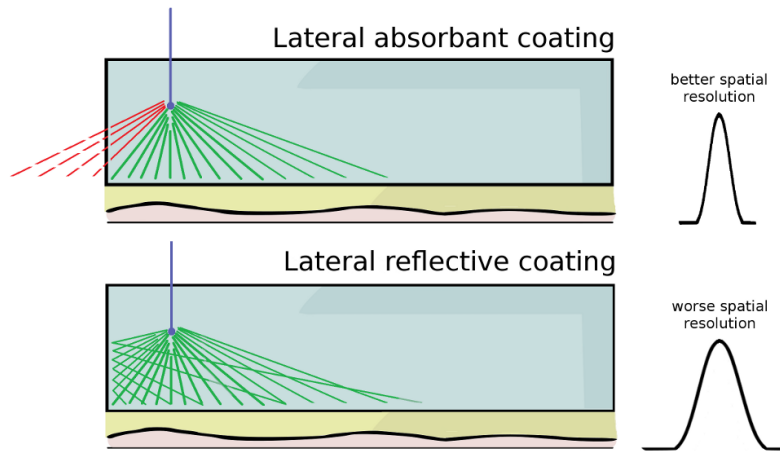


Figure 4.1: A trade-off must be discussed when considering charge collection. Different types of coatings have been implemented in order to fulfil the specifications concerning spatial resolution, that is the most expected feature of the Hicam gamma camera.

light: the consequences will be analysed as a worsening of the statistical noise contribution.

Spatial resolution, as already mentioned in the first chapter, must be one of the strong point of the Hicam gamma camera. Therefore all the measures were taken in order to achieve a good spatial reconstruction, to the detriment of a good energy resolution which is now a tricky requirement to meet.

This situation though, represents an obstacle when evaluating the measurements carried out with real patients. The γ -rays coming from the tracer injected in the human body are scattered when traveling through the tissues, being deflected from the original trajectory and losing part of their energy. If the detection system resolution is not high enough, it won't be possible to distinguish and reject scattered photons to reconstruct a clear image with a sharp spectrum, worsening the spatial resolution.

In our system energy resolution is about 20% (in a low-energy range) which makes it impossible to recognize two sources in a narrow energy window. An experiment has been carried out trying to reconstruct two sources at the same time: the first one is ^{57}Co , used in lots of tests, emitting γ -rays at 122keV , while the second one is $^{99\text{m}}\text{Tc}$, emitting γ -rays at 140keV , which is the source commonly used with patients. As it can be seen in figure 4.2, the two sources cannot be distinguished with our system. For this consideration, the sources ($^{99\text{m}}\text{Tc}$ and ^{57}Co) were simulated both in separated acquisitions, and then in the same experiment. During the reconstruction of the images it's thus necessary to consider the whole spectrum, in a reasonable energy range, settling for a low energy resolution and trying to improve to the utmost the the imaging features.

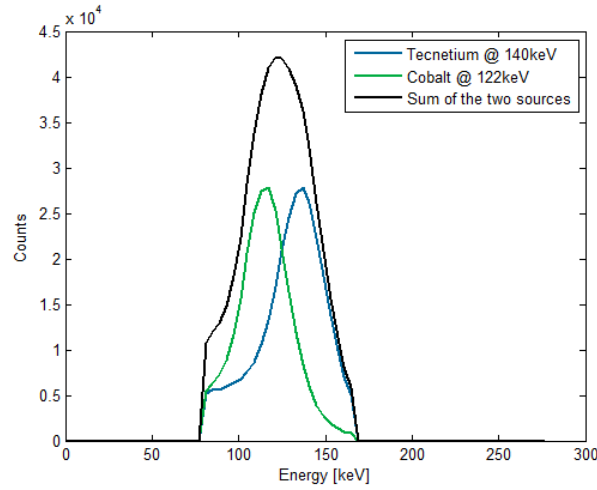


Figure 4.2: Spectra of a ^{57}Co and a $^{99\text{m}}\text{Tc}$ source. The sources cannot be distinguished in the global spectrum when analysed together because of a low energy resolution.

All the considerations made are based on the centroid method as our reconstruction algorithm: it is a very simple method, which however is affected by serious issues which will be discussed in detail up ahead.

4.2 Energy resolution analysis

In the previous paragraph it's been pointed out that the energy resolution is a limiting factor in the analysis of the reconstructed images. In this part, all the mechanisms involved in the detection will be investigated, discussing each contribution and the reasons of a similar spread in order to come up with a solution which allows a significant improvement.

4.2.1 Calculating the total energy resolution

The analytic formula used to calculate the energy resolution has been already demonstrated [17], and it is reported hereafter.

$$R_{tot} = \frac{\Delta E}{E} = 2.36 \sqrt{\left(\frac{\Delta E}{E}\right)_i^2 + \left(\frac{\sqrt{N_E}}{N_E}\right)^2 + \left(\frac{\sqrt{N_{SDD}} \cdot ENC}{N_E}\right)^2}, \quad (4.1)$$

where:

$\left(\frac{\Delta E}{E}\right)_i^2$: it is the intrinsic resolution of the scintillation crystal, which is related to several effects, like inhomogeneities due to the local variation of the light output or variations of the properties of the coatings surrounding the crystal;

$\left(\frac{\sqrt{N_E}}{N_E}\right)^2$: it is the statistical spread due to the scintillation photon generation and to the photon-electron conversion inside the detector, according to Poisson's distribution;

$\left(\frac{\sqrt{N_{SDD} \cdot ENC}}{N_E}\right)^2$: it is the statistical spread due to the *equivalent noise charge* introduced by the electronic read-out system;

N_E : it is the total number of primary electrons generated in the photodetector.

The trend of total energy resolution is shown in figure 4.3, as a function of the three contributions previously mentioned. In the first graph only one SDD is considered, and the resolution is dependent on all the three different sources. In the second graph instead, it's visible that electronic noise becomes dominant when multiple detectors are involved, while intrinsic and statistical contributions stay constant. This evaluation is necessary because gamma rays are absorbed in the scintillation crystal and no direct ionization occurs in the devices; the photons are thus spread over the detector layer (some of them are not detected because of dead areas and lateral absorbent coatings) involving a several detector whose electronic noise corrupts the measurement.

These curves show how energy resolution changes at a rough estimate: these value will be confirmed hereafter making use of a simulator compiled in *Matlab* by a specialized team working in our laboratories. From now on, intrinsic spread, statistical spread and electronic noise contribution will be investigated in detail.

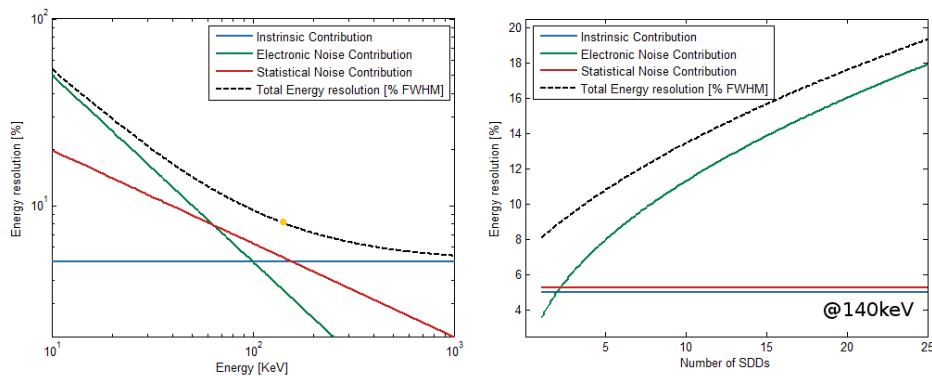


Figure 4.3: Trend of the energy resolution as a function of the energy (left) and trend of the energy resolution as a function of the number of detectors involved (right).

4.2.2 Intrinsic contribution

As already mentioned before, the intrinsic resolution brought by the scintillation crystal is dependant on lots of factors, like inhomogeneities due to the local variation of the light output or variations of the properties of the coatings surrounding the crystal. Unfortunately it's not possible for us to evaluate such parameters or the optical properties of the covers, therefore results coming from other experiments will be considered. In fact, several studies were carried out to evaluate yield and intrinsic resolution of a CsI(Tl) scintillator [18]. We supposed those characteristics to be constant, on the contrary it was discovered that they may change, as a function of both the energy range and the dopant concentration. For simplicity, from now on we will assume that at $140keV$ the instrinsic resolution of the CsI(Tl) crystal implemented in the Hicam gamma camera is about 5%, which is a good approximation to carry out an initial estimate.

4.2.3 Statistical contribution

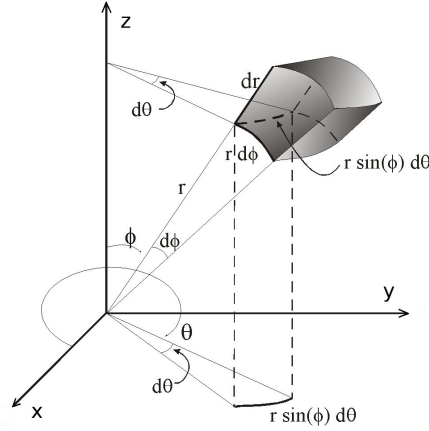
Statistical contribution to the total energy resolution depend on the number of electrons generated in the detectors whenever a γ -ray is absorbed in the crystal. The mean number of electrons will be now calculated considering all the factors that lead to a loss of photons or charges, and the result will be confirmed with the simulation of a flood image whose spectrum is expected to have a peak in correspondence to the value of N_E calculated. Efficiency η_{tot} is calculated considering both *quantum efficiency* η_q , and *geometrical efficiency* η_{geom} .

$$N_e = \eta_{tot} \cdot \Phi_{fresnel} \cdot N_{ph} = \eta_q \cdot \eta_{geom} \cdot \Phi_{fresnel} \cdot Y E_\gamma. \quad (4.2)$$

Quantum efficiency Quantum efficiency for Hicam SDDs coupled to a CsI(Tl) source ($\lambda = 550nm$) is about $\eta_q \approx 85\%$, taking advantage of a specific anti-reflective layer [19].

Geometrical efficiency Considering geometrical efficiency instead, it's necessary to investigate how Hicam dead areas affect the computation. As already mentioned, $\eta_{geom} = \frac{\Omega}{\Omega_{tot}}$, where Ω is the solid angle that a generic surface subtends at a point, while Ω_{tot} is the solid angle of a sphere, 4π . The solid angle for an arbitrary oriented surface S subtended at a point P is equal to the solid angle of the projection of the surface S to the unit sphere with center P, which can be calculated as the surface integral:

$$\Omega = \int \int_S \frac{\vec{r}' \cdot \hat{n}}{|r'|^3} dS, \quad (4.3)$$

Figure 4.4: Representation of a generic solid angle $d\Omega$.

where \vec{r} is the vector position of an infinitesimal area of surface dS with respect to point P and where \hat{n} represents the unit vector normal to the surface itself. This formula can be expressed both in cartesian coordinates

$$\Omega = \iint_S \frac{z}{\sqrt{(x^2 + y^2 + z^2)^3}} dx dy, \quad (4.4)$$

and in spherical coordinates

$$\Omega = \int \int_S \sin\phi d\phi d\theta, \quad (4.5)$$

where ϕ is the polar angle and θ the azimuth, shown in Figure 4.4.

Whenever a γ -ray interaction is considered though, Ω can't be defined as in eq.(4.3), where dS is the whole detection area and P the interacting point. It's thus necessary to take into account the critical angle ϑ_{lim} , defined by *Snell's Law* as the largest possible angle of incidence which still results in a refracted ray:

$$\vartheta_{lim} = \text{asin} \left(\frac{n_2}{n_1} \right), \quad (4.6)$$

where n_1 and n_2 are the refractive indexes of the scintillation crystal and the material interposed between the crystal itself and the detection matrix, usually a type of optical grease. In any other case the photons are totally reflected on the inside of the crystal. Considering this limitation, it is possible to calculate the actual solid angle Ω :

$$\Omega = \int_0^{2\pi} \left[\int_0^{\vartheta_{lim}} \sin\phi d\phi \right] d\theta = 2\pi[1 - \cos(\vartheta_{lim})]. \quad (4.7)$$

If the detector matrix hasn't any dead areas and it is wide enough to read all the visible light, the geometric efficiency can be eventually defined as:

$$\eta_{geom} \Big|_{id} = \frac{2\pi[1 - \cos(\vartheta_{lim})]}{4\pi} = \frac{1 - \cos(\vartheta_{lim})}{2}. \quad (4.8)$$

The elements implemented in the Hicam system will be now examined: the refraction index of CsI(Tl) scintillator is $n_1 = 1.788$, while the refraction index of optical grease is $n_2 = 1.463$. The critical angle is calculated as:

$$\vartheta_{lim} = \text{asin} \left(\frac{n_2}{n_1} \right) = \text{asin} \left(\frac{1.463}{1.788} \right) = 54.90^\circ. \quad (4.9)$$

Considering only the direct light contribution, the maximum value of the geometric efficiency is:

$$\eta_{geom} \Big|_{id} = \frac{1 - \cos(\vartheta_{lim})}{2} = 21.26\%. \quad (4.10)$$

In the real system unfortunately we have a matrix of detectors, and dead areas among them: geometric efficiency is obviously reduced since visible photons interacting with them are lost. This situation is shown in figure 4.5.

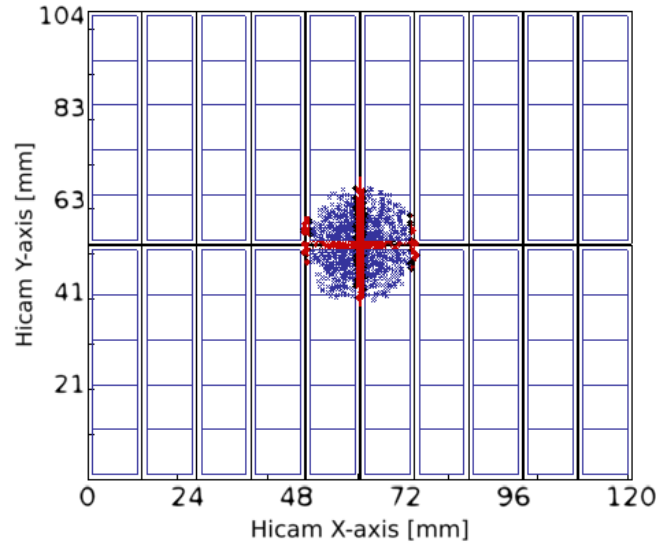


Figure 4.5: Representation of Hicam detectors: not all the photons generated after the scintillation are collected (in blue: photons collected, in red: photons lost because of dead areas).

With Matlab it is possible to evaluate the global effect of dead areas on geometric efficiency: for a given point of interaction $P(\bar{x}, \bar{y}, \bar{z})$ solid angle can be calculated as:

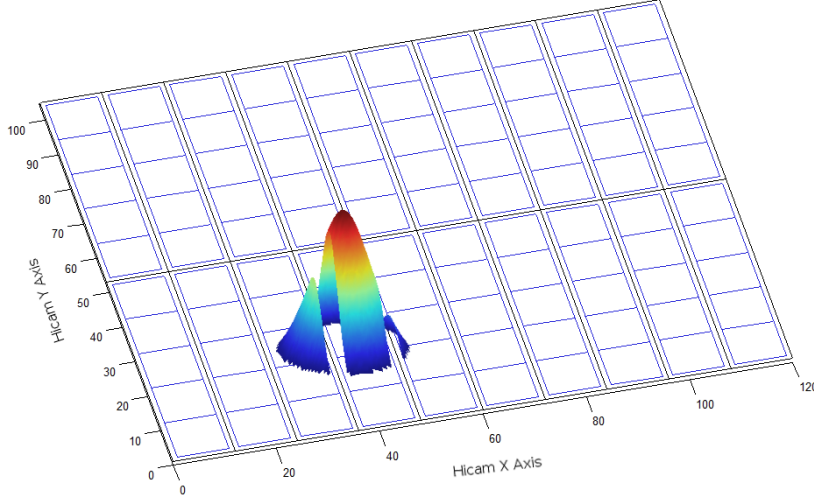


Figure 4.6: Solid angle including only those photons which are collected by detectors.

$$\Omega(\bar{x}, \bar{y}, \bar{z}) = \int \int_S \frac{\bar{z}}{\sqrt{(x^2 + y^2 + \bar{z}^2)^3}} dx dy = \sum_i \left(\sum_j \frac{\bar{z}}{\sqrt{(x_i^2 + y_j^2 + \bar{z}^2)^3}} \right). \quad (4.11)$$

The surface dS subtended at P can be fractionated in small areas $dx dy$ and the double integral can be approximated with the summation of the function evaluated in $dx dy$. Dead areas contribute with a significant loss of photons, as shown in figure 4.6.

This analysis is carried out in order to compile an efficiency map, calculated as the percentage of photons collected for each point of the detector layer. A customized software was designed to scroll an ideal source automatically from side to side across the detectors, and calculating how many photons are collected, considering both solid angle domain boundaries and dead areas contribution. Obviously, the diameter of the solid cone of light is variable with the depth of the interaction, since the critical angle is constant, thus is necessary to compute a weighted average considering the different coordinates of absorption. These mechanism are described by the following equations:

$$\Phi(z) = \lambda \cdot e^{-(z/\lambda)} \quad (4.12)$$

$$\eta_{geom}(x, y) = \frac{\int \eta(x, y, z) \cdot \Phi(z) \cdot dz}{\int \Phi(z) \cdot dz} \quad (4.13)$$

$$\eta_{geom}(x, y) \approx \frac{\sum_z \eta(x, y, z) \cdot \Phi(z)}{\sum_z \Phi(z)}. \quad (4.14)$$

Total efficiency $\eta_{geom}(x, y,)$ is the weighted average of efficiencies evaluated with different values of z (as shown in equation 4.13), with the absorption probability $\Phi(z)$ being the weight (equation 4.12). The chosen step on the z -axis is $1mm$, so the computation of $\eta_{geom}(x, y)$ is achieved using a discrete approximation of the usual continuous representation (as shown in equation 4.14). Efficiency values are stored in a matrix, whose size is dependent on the pixel dimension in which the detector level is divided. The chosen value is $0.4mm$ both along the X axis and the Y axis. In Figure 4.8 it is represented as a surf plot. The dimension of the pixel used to define the integration domain of the solid angle is $0.2mm$.

These analysis were carried out considering only the worsenings brought by the critical angle and the dead areas. Contributions coming from electronic noise or Poisson's spread of the visible photons were not included in the calculation. Figures 4.8 and 4.9 refer to the bigger gamma camera, Hicam100, because it's easier to notice the impact of these factors, but the same considerations are valid for Hicam25 as well. It's important to remember that the top layer covering the scintillation crystal is supposed to be ideally reflective, while all the other coatings are supposed to be totally absorbent. That's why the maximum value of the efficiency map is not equal to the one calculated before; the overall efficiency is computed taking advantage of the virtual image, as shown in figure 4.7.

The goal of these charts is to show that dead areas have a great influence on the geometric efficiency, worsening the photon detection. We should notice that the value of efficiency in correspondence to vertical dead areas (along the Y axis) is similar to the value in correspondence to the horizontal one (along the X axis), if considered in relation to an absolute scale. However, a loss of efficiency leads to a loss of photons, necessary to compute the centroid of the event. For this reason, this shouldn't cause a loss of

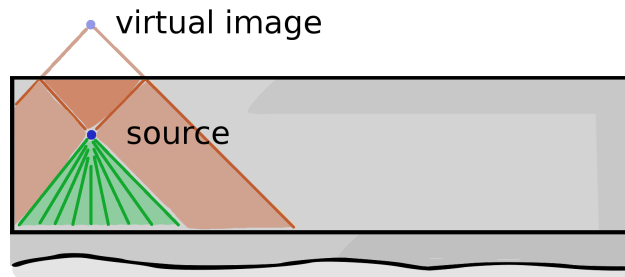


Figure 4.7: In the evaluation of the efficiency map both direct and reflected contribution are considered.

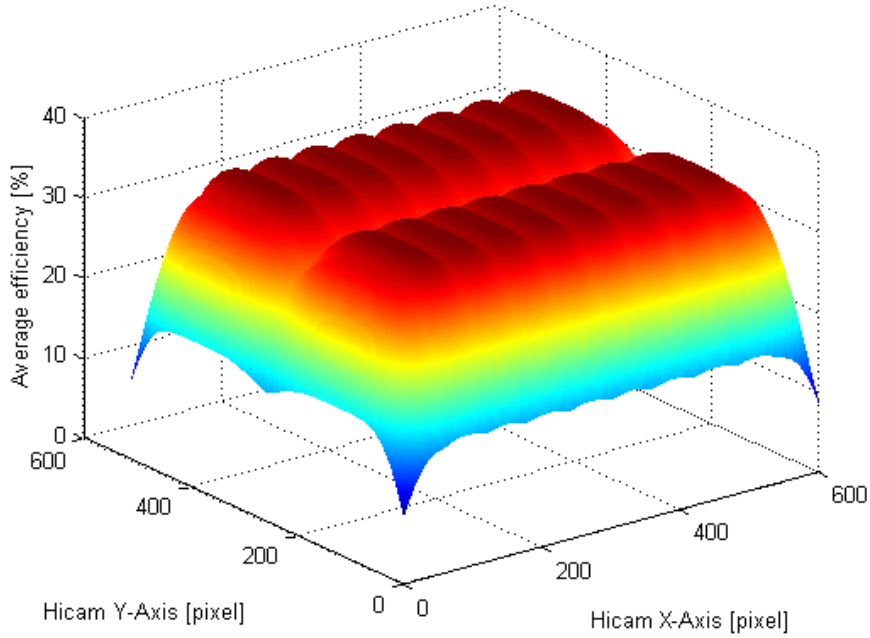


Figure 4.8: Total efficiency map represented as an interpolated surf plot.

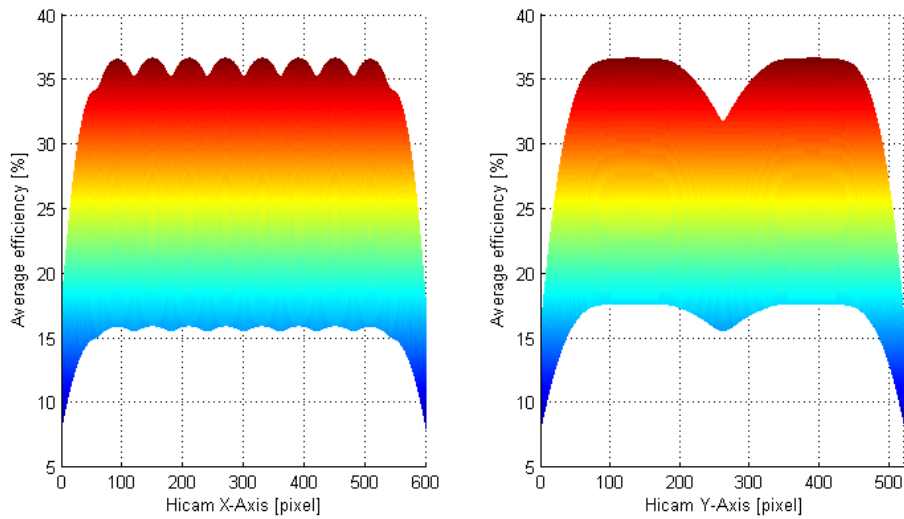


Figure 4.9: Total efficiency map projections, on Hicam axis.

counts (reconstructed events), but only a worse statistic bringing a decrease in the signal-to-noise ratio (proportional to the square root of the photons collected \sqrt{N} , according to *Poisson's distribution*). If some of the photons

are not collected, the relative contribution of electronic noise is bigger and the computation of the centroid is less accurate. Thanks to the simulations it will be demonstrated that efficiency is affected by the geometrical extension of the valleys of the efficiency map, and not by their value (Figure 4.9).

For a rough estimate of the geometrical efficiency we can conclude that $\eta_{geom} = 35\%$, calculated as the mean value of the weighted map of efficiency.

Considering also the contribute coming from quantum efficiency, it's possible to use this approximation:

$$\eta_{tot} \Big|_{mean} = \eta_q \cdot \eta_{geom} \approx 0.85 \cdot 0.35 = 0.2975 = 29.75\% \quad (4.15)$$

Transmission coefficient The transmission coefficient is represented by $\Phi_{fresnel}$ and it is introduced because when light moves from a medium of a given refractive index n_1 into a second medium with refractive index n_2 , both reflection and refraction of the light may occur, according to the *Fresnel equations*.

The fraction of the incident power that is reflected from the interface is given by the *reflectance* (R) and the fraction that is refracted is given by the *transmittance* (T); therefore these coefficients are usually expressed as percentages, and T is obtained as $T = 1 - R$. The calculation of R and T are depending on the polarisation of the incident light. Equations for coefficients corresponding to ratios of the electric field amplitudes of the

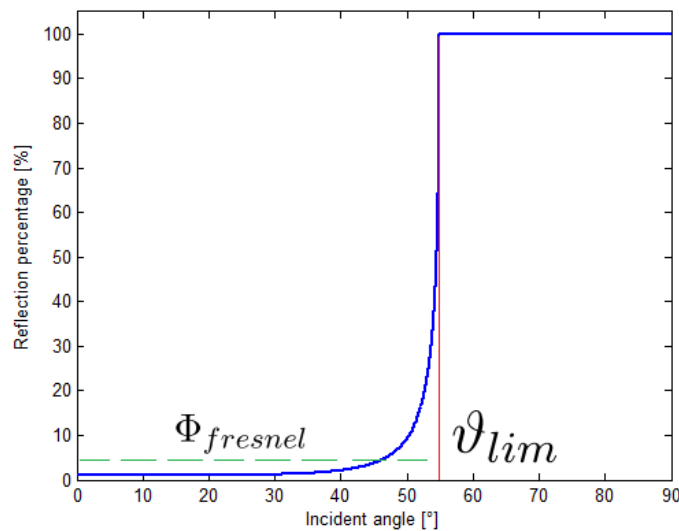


Figure 4.10: Reflectance of an incident ray of visible light. Light strikes the interface between a CsI(Tl) ($n_1 = 1.788$) and Visilox optical grease ($n_1 = 1.463$).

waves can also be derived, and these are also called *Fresnel equations*. As a consequence, it is clear that the critical angle is not a sharp limit in the light absorption. In figure 4.10 the real reflectance between a CsI(Tl) ($n_1 = 1.788$) and Visilox optical grease ($n_1 = 1.463$) is plotted. The simulator used takes account of this phenomenon, but for this first estimate it's necessary to make approximations. The critical angle will be considered as the last limit: all the photons striking the interface with an angle $\vartheta > \vartheta_{lim}$ will be totally reflected. Otherwise, the photons included in the solid angle are absorbed, but the intensity is attenuated by a mean coefficient $\Phi_{fresnel} = 0.98$ (dashed line in figure 4.10).

Scintillation Yield The nominal value of the yield of the crystal is considered as a constant, but it undergoes variations according to Poisson's distribution. This feature is a worsening factor when evaluating the energy resolution, and it is correctly implemented in our simulator. Furthermore the yield is also dependant on the temperature of the crystal, but few references are available, and they are different from each other. Therefore, since no reliable documents were found about the trend of the yield against temperature, it was considered as a constant in all the simulations carried out. It would be useful to run some test to evaluate this relationship, but with our system it is impossible to consider the contribution of the crystal alone, excluding performances of the detectors, that are seriously affected by temperature changings and electronic noise contributions.

After having obtained the values of all worsening factors, it is now possible to calculate the mean number of electron. The following values will be used: $E_\gamma = 140.2keV$, assuming that a ^{99m}Tc source is used, and $Y = 54ph/keV$ for our CsI(Tl) crystal.

$$N_e = \eta_{tot} \Big|_{mean} \cdot \Phi_{fresnel} \cdot Y E_\gamma = 0.2975 \cdot 0.98 \cdot 54ph/keV \cdot 140.2keV \approx 2207e^- . \quad (4.16)$$

To confirm this result, the simplest simulation will be run: a flood source, uniform all over the detector surface; 50000 γ -rays are randomly fired with an orthogonal incident direction. Gamma events are simulated using *Geant3* [11], which implements the real total attenuation coefficient.

The spectrum shown in figure 4.11 can be fitted with a gaussian curve, accounting an energy resolution equal to 7% and a peak at $2200e^-$. This value may be obtained in case no equivalent noise charge were introduced by the electronic read-out stage and with the crystal being totally ideal. This considerations are developed with an academic purpose, since this ideal situation cannot be reached in a real system.

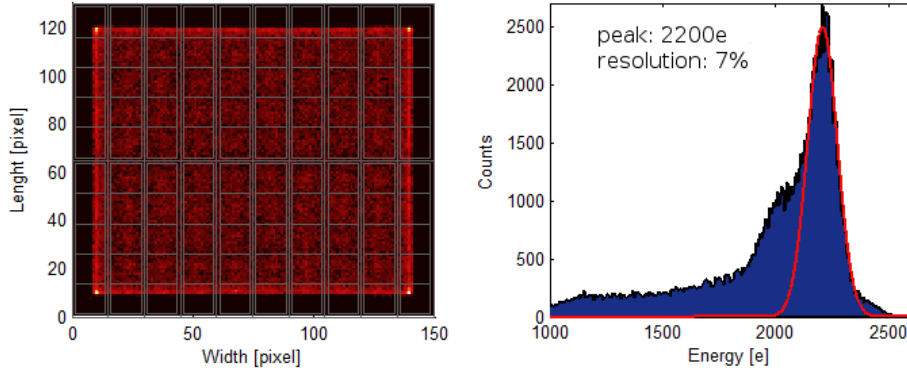


Figure 4.11: Reconstructed image and spectrum of the flood simulation, used to confirm the impact of the statistical contribution to the total energy resolution.

The energy resolution affected by intrinsic and statistical contributions is equal to:

$$R_{tot} = \frac{\Delta E}{E} = 2.36 \sqrt{\left(\frac{\Delta E}{E}\right)_i^2 + \left(\frac{\sqrt{N_E}}{N_E}\right)^2} = \sqrt{(5\%)^2 + (7\%)^2} \approx 8.6\%. \quad (4.17)$$

Considering figure 4.3, the contribution of both intrinsic and statistical resolution, quadratically added, lead to a total energy resolution of about 7.8%. Nevertheless the value obtained analysing simulated data is slightly worse than expected. In fact, as a first approximation, the geometry of the detector matrix was not considered, and the number of electrons was intended as the sum of the charges collected in each SDD. This assumption is strictly valid if a boundless matrix of detector is evaluated. In our case instead, if a gamma ray is absorbed near the edges, part of the visible photons will be absorbed by the coating applied on the lateral faces of the crystal: this phenomenon is a practical demonstration that the mean number of electrons shouldn't be considered as a constant, and it is necessary to make use of the simulator to achieve calculations with a better precision.

In figure 4.12 the phenomenon previously described is shown: the gamma photons that are absorbed in the active area account for a total energy which contribute to the peak of the spectrum; otherwise the events reconstructed in correspondance to the borders and the central dead area lead to a spread in the spectrum, worsening the energy resolution, due to a loss of collected charges.

The electronic noise contribution will be analysed in detail in the next section since it is dominant when several detectors are involved in the detection process.

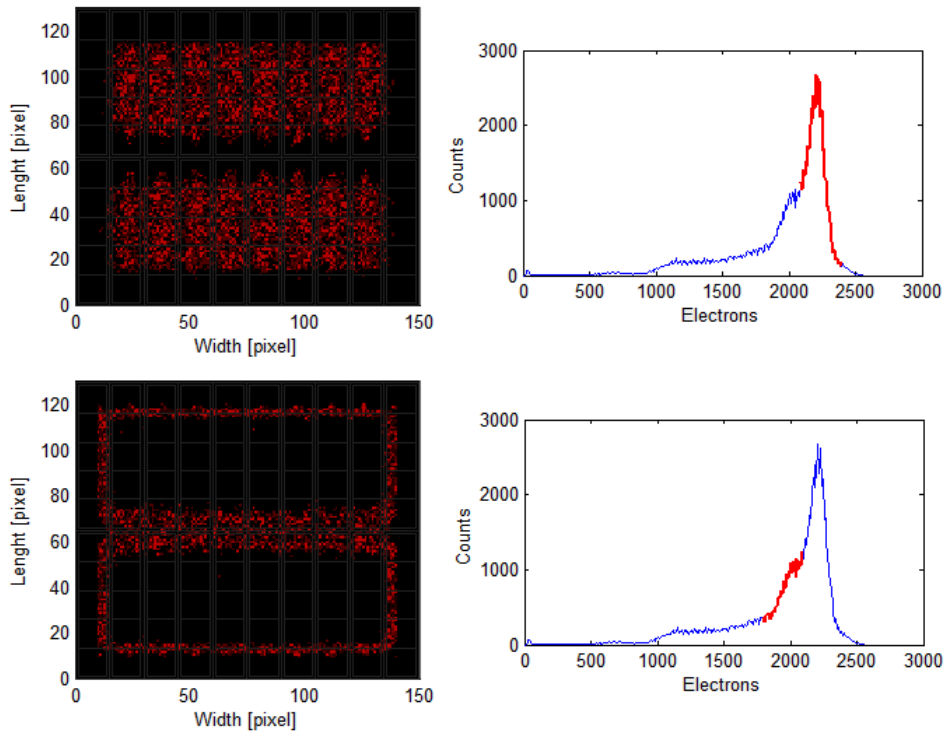


Figure 4.12: Events reconstructed in different locations in the detector matrix lead to a spread of the spectrum.

4.2.4 Electronic noise contribution

Electronic noise contribution is the most significant when several detectors are involved. In our case, a number of 24 detectors is averaged in the previous simulation, as shown in figure 4.13, therefore it may be assumed that

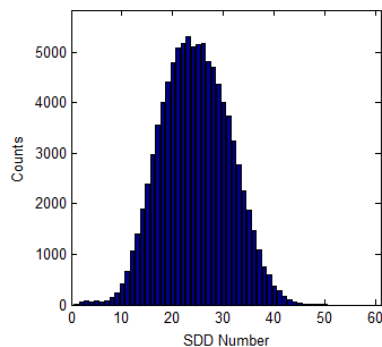


Figure 4.13: Histogram of the number of SDD involved in the detection of a gamma event at 140.2 keV.

electronic noise affects energy resolution with a dominant contribution.

In the following paragraph, the *equivalent noise charge* will be introduced, showing the contributions that lead to the final formula and analysing the solutions adopted to minimize the impact of noise on the performances of the Hicam system. The calculation of the ENC has already been studied and deepened in several articles [8], and will not be reported here in its complete formulation.

ENC calculation

The *equivalent noise charge (ENC)* is introduced to evaluate the noise performances of the detectors. By definition, the ENC is the total amount of charge that needs to be collected in the SDD to achieve a signal-to-noise ratio equal to 1 at the end of the analog electronic acquisition; it is usually expressed in number of electrons. The total formula is reported hereafter:

$$ENC^2 = (C_D + C_G)^2 A_1 \frac{a}{\tau} + (C_D + C_G)^2 c A_2 + b \tau A_3;$$

the different elements are described in the following list:

τ is the shaping time.

a is the series contribution which is represented by the thermal noise of the preamplifier (FET); it is in inverse proportion to the shaping time.

$$a = S_{v,thermal} = \frac{2\alpha KT}{C_G \omega_T};$$

α is a parameter depending on the working point and it is considered as $2/3$, while ω_T is the cutoff frequency.

b is the parallel contribution and it is due to the leakage current of the detector and the shot noise of the current of the FET amplifier. It is directly proportional to the shaping time.

$$b = S_{i,dark} + S_{i,FET} = qI_{dark} + qI_{FET};$$

c is the $1/f$ contribution and it is due to the fluctuating occupancies of traps in the preamplifier.

$$\frac{c}{|\omega|} = S_{1/f} = \frac{A_f}{2|f|} = \frac{2\alpha KT \omega_1}{C_G \omega_T |\omega|};$$

A_f is the flicker noise coefficient and ω_1 is the noise corner frequency.

C_D , C_G are respectively the capacitance of the detector itself, and the capacitance associated to the gate of the FET.

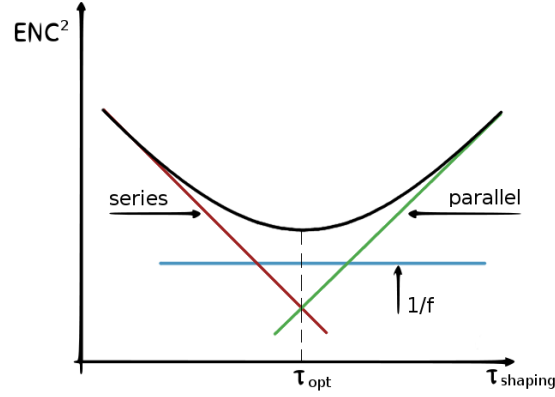


Figure 4.14: Trend of the equivalent noise charge as a result of three different contributions: series, parallel, and $1/f$. The ENC^2 is plotted as a function of the shaping time.

A_1 , A_2 , A_3 are dimensionless coefficients depending only on the shape of the impulse response of the shaping filter itself.

Considering the curve plotted in figure 4.14, is it possible to calculate the optimum shaping time (τ_{opt}) in order to have a smaller equivalent noise charge to affect our imaging system.

$$\tau_{opt} = \sqrt{C_D} \left(\sqrt{\frac{C_D}{C_G}} + \sqrt{\frac{C_G}{C_D}} \right) \sqrt{\frac{2\alpha KT}{\omega_T q I_L}} \sqrt{\frac{A_1}{A_3}};$$

$$ENC^2(\tau_{opt}) = 2\sqrt{C_D} \left(\sqrt{\frac{C_D}{C_G}} + \sqrt{\frac{C_G}{C_D}} \right) \sqrt{\frac{2\alpha KT q I_L}{\omega_T}} \sqrt{A_1 A_3}.$$

It's clear that the equivalent noise charge is reduced whenever a smaller depletion capacitance of the detector (C_D) is considered. That is the reason why SDDs provide better performances if compared to PIN diodes with the same active area.

In order to maximize the signal-to-noise ratio, it should be better to implement a matched filter, which in this case is an ideal cusp [7]. However, this kind weighting function is not physically achievable and it is necessary to find other solutions. One of them is the semigaussian filter, which may be implemented taking advantage of both real and complex conjugate poles. Once the shape of the filter has been chosen, the coefficients A_1 , A_2 and A_3 are determined.

Furthermore, there are other implications that need to be checked before choosing the correct value of shaping time. On one hand, if the shaping time is too long, it may occur that a signal is overlapped with the following one, leading to a corrupt stream of data which is impossible to reconstruct

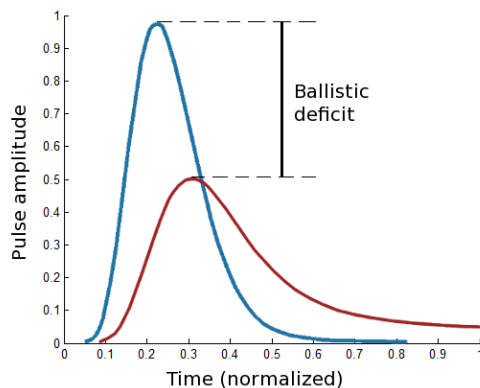


Figure 4.15: Representation of the ballistic deficit. A significant loss of charge occurs because of a short shaping time.

correctly. On the other hand, if the shaping time is too short, only part of the total charge is integrated and the output of the filter do not manage to reach the maximum amplitude, leading to a loss of signal. This phenomenon is called *ballistic deficit* and a schematization is pictured in figure 4.15. In fact, the pulses coming from the detectors are not perfect delta functions, because the scintillation crystal spreads visible photons according to a given time constant, which in CsI(Tl) is comparable with shaping time values commonly used. This situation is found in the Hicam system too: the solution is to adopt a shaping time longer than the optimum $\tau > \tau_{opt}$.

The most significant consequence of this loss of charge due to the ballistic deficit is the worsening of the signal-to-noise ratio. As a practical evaluation, the representation of this phenomenon will be carried out keeping constant the value of the signal while the number of noise electrons will be increased.

$$ENC_{DB} = \frac{ENC}{1 - DB}$$

In the Hicam system ballistic deficit is negligible, since the crystal has a time constant which is $1\mu s$ long while the shaping time used during gamma experiments is much longer, measuring $8.3\mu s$.

It should be mentioned that ENC worsens as the temperature of the detectors increases. In fact, thermal noise and most of all leakage current are significant factors which bring a serious worsening in the reading of the signal. For these reason, detectors are cooled down to low temperature values ($-5^\circ \div -10^\circ$) thanks to a Peltier stage and a chiller, which have already been introduced. However, scintillation crystal performances are affected by temperature changings, resulting in a variable yield of scintillation. In particular, if the temperature drops below a given range typical of the crystal, less visible photons are irradiated as a consequence of a gamma ray absorption, leading to a signal that is smaller in amplitude than expected. These two

effects seem to compensate for each other, but actually an objective measurement cannot be carried out to define these relationships, since the process itself would be corrupted by the factors that are to be measured. Considering these issues, dependancies on the temperature are not implemented in the simulator, and the value of the ENC should be chosen according to experimental data.

ENC in the Hicam system

For both the Hicam prototypes, the photodetectors without scintillation crystal have been directly irradiated with a ^{55}Fe source in order to achieve an evaluation of the electronic noise offered by the SDD array. The equivalent noise charge was determined from the energy resolution measured at 5.9keV (with a gaussian fit of the peak), subtracting the square of the Fano contribution. The acquisition with the bigger camera was carried out with the SDDs cooled down to a temperature of -10° and a peaking time of $8.3\mu\text{s}$ for the shaping amplifier. All units showed spectra with homogeneity of performances; some of them are reported in figure 4.16. The calculated average noise is of about 30 electrons rms.

The curve of the ENC as a function of the shaping time is not reported here, but it's important to mention that the gamma camera is operating in a range where parallel noise contribution is dominant. Shaping time can be chosen among few values included in a range between $2.8\mu\text{s}$ and $11\mu\text{s}$.

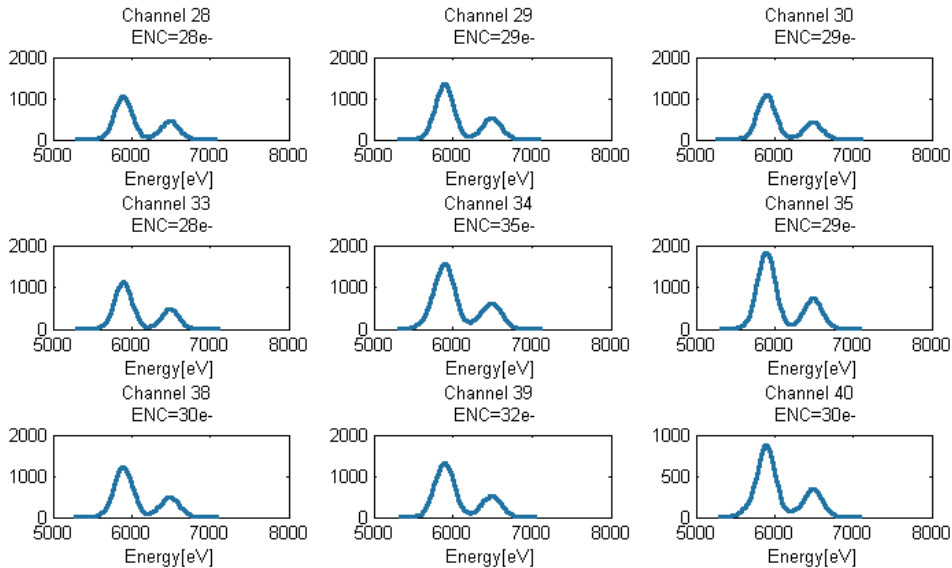


Figure 4.16: Some of the detector spectra are shown: a ^{55}Fe source was employed for this acquisition. These are some of detector arrays mounted in the bigger prototype.

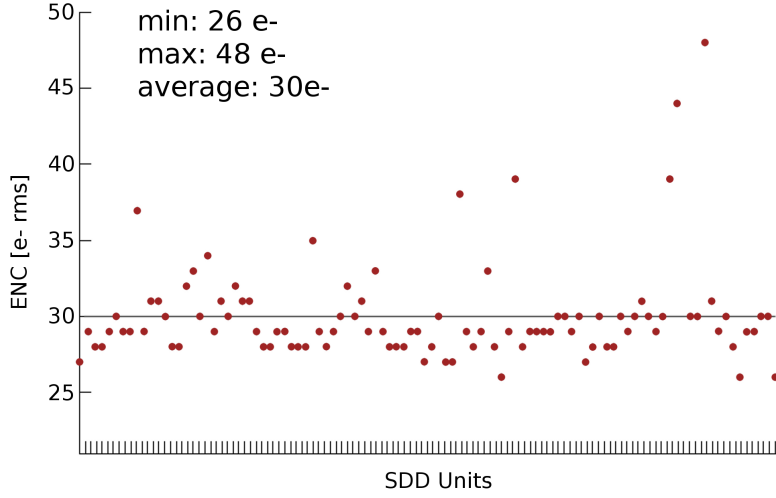


Figure 4.17: Trend of the equivalent noise charge. ENC value is calculated for each SDD, and an average value will be used for the following simulations.

In this case, a value equal to $8.3\mu s$ is used. These values are greater than the optimum but they represent the only feasible solution to achieve an acceptable ENC and a relatively low ballistic deficit, since the CsI(Tl) crystal provides high gain but it suffers from a slow time constant.

Calculation of the energy resolution

After having explained how the equivalent noise charge is affecting our measurement system, it's now possible to analyse how this phenomenon worsens the energy resolution and the performances of the gamma camera.

The simulation that will be run to obtain these results is carried out with the same initial conditions as the previous one, and then equivalent noise charge is introduced according to Poisson's distribution. A value of $ENC=30e$ rms is considered.

The spectrum shown in figure 4.18 can be fitted with a gaussian curve, accounting an energy resolution equal to 20.3% and a peak at $2300e^-$. In the simulation, the intrinsic spread brought by the crystal is not considered.

The energy resolution affected by intrinsic, statistical and electronic noise contributions is equal to:

$$R_{tot} = \frac{\Delta E}{E} = 2.36 \sqrt{\left(\frac{\Delta E}{E}\right)_i^2 + \left[\left(\frac{\sqrt{N_E}}{N_E}\right)^2 + \left(\frac{\sqrt{N_{SDD}} \cdot ENC}{N_E}\right)^2\right]}, \quad (4.18)$$

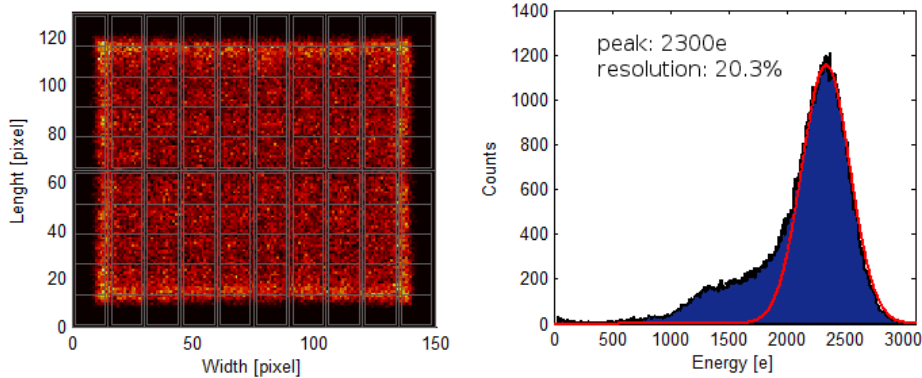


Figure 4.18: Reconstructed image and spectrum of the flood simulation, used to confirm the impact of the electronic noise contribution to the total energy resolution.

$$R_{tot} = \frac{\Delta E}{E} = \sqrt{\left(5\%\right)^2 + \left(20.3\%\right)^2} \approx 20.9\%, \quad (4.19)$$

where an average value of 24 involved detectors has been considered.

Considering figure 4.3, the sum of the three contributions, quadratically added, lead to a total energy resolution of about 19.5%. All the considerations previously made about the worsening of the energy resolution due to the detector layout remain still valid.

From now on, we will take advantage of the simulations in order to make a detailed comparison with the experimental data. Thanks to the simulator in fact, it is possible to keep track of the coordinates of absorption of each gamma event, allowing us to make some further considerations about some phenomena that would be undiscovered if studies were focused only on real acquisitions.

However, in the comparison with real data, a significant worsening is expected, because we have not considered some phenomena that have a great influence on resolution: for example, the variations of the light yield with the temperature or the percentage of reflection of the top coating of the crystal. This analysis is completed as an ideal case, shown only to explain how resolution may be affected from different sources. Unfortunately these contributions cannot be quantified with a certain procedure, and should be investigated in the future.

4.3 Dead areas impact

All the factors which bring a significant contribution to the energy resolution have been presented in detail before. The total number of electrons is

depending mainly on the value of geometrical efficiency that should be considered for a given gamma event. The two factors that reduce the amount of photons that reach active areas are the solid angle (depending on the critical angle) and the dead areas. The percentage of dead areas is variable, according to the three dimensional coordinates of the point where the gamma ray is absorbed. In figure 4.8 a distribution map of efficiency was presented. The map is calculated as a weighted average of several maps obtained simulating interactions at different depths of absorption, where the weight is the exponential function that represent the absorption probability. To calculate the average number of electrons collected after each interaction, an average value of efficiency was considered. This approximation seems to be valid in the central active area, excluding those detectors near the borders of the gamma camera. However it is better to analyse in detail how efficiency change when a gamma ray is absorbed in the crystal at a low-z coordinate, since these events may affect reconstruction.

Figure 4.19 and figure 4.20 will be now discussed. In the first diagram (figure 4.19(A)) the trend of efficiency along z-axis is plotted. The simulated point is located at the centre of a detector, and if the gamma ray is absorbed near the detector layer, maximum theoretical efficiency is achieved as expected when considering only direct light contribution. However, efficiency worsen if the photon is absorbed near the top of crystal since the cone of light include dead areas where visible photons cannot be absorbed. Considering direct and reflected light together instead (figure 4.19(B)), the situation is almost the same since reflected light brings a contribution which is almost constant. The simulations were then carried out moving the source point to a dead area. The direct light contribution trend (figure 4.20(A)) is opposite to the one in the previous case: in fact, when the photon is absorbed near the detector layer, the cone of light is so small that no photons actually hit

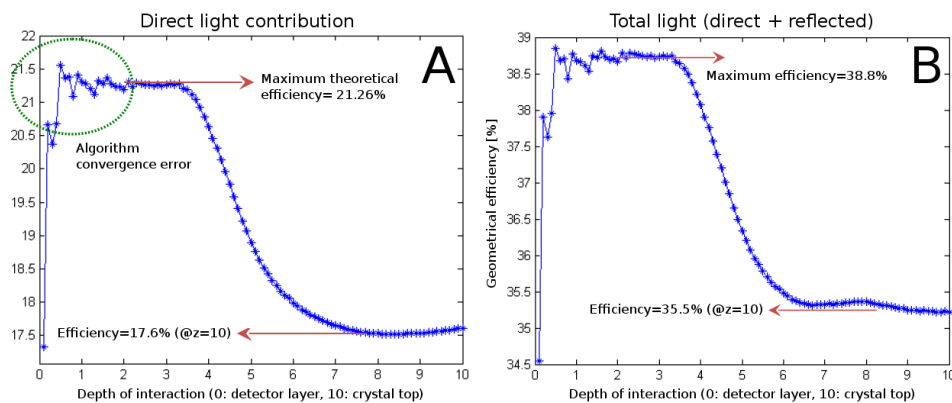


Figure 4.19: Trend of efficiency along Z-axis, orthogonal to the detector layer. The simulated point of interaction is located at the centre of a detector.

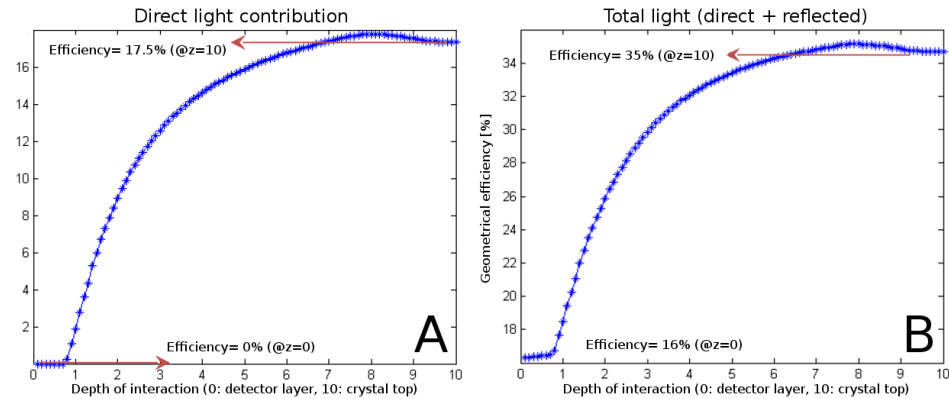


Figure 4.20: Trend of efficiency along Z-axis, orthogonal to the detector layer. The simulated point of interaction is located at the centre of a dead area.

an active area, leading to an efficiency value of 0%. The efficiency calculated considering both direct and reflected light (figure 4.20(B)) is increasing moving towards the top of the crystal since more active areas are involved (in percentage), and since the reflected light brings a constant contribution even in this case ¹.

As a conclusion it is useful to compare figure 4.19(B) with 4.20(B). Efficiency value is almost similar if the photon is absorbed near the top of the crystal, that however is the most likely occurrence, but serious differences are to be faced whenever the photons is absorbed more deeply in the crystal, which is not a rare situation in a relatively thin scintillation crystal such as ours. This phenomenon affects the performances of the gamma camera in terms of energy resolution as presented previously, but it also results in reconstruction artifacts that cannot be avoided if the process is carried out with the centroid method. Energy resolution in fact, is affected by electronic noise, which is the dominant factor, and the worsening brought by dead areas are not so relevant. Considering reconstruction issues instead, dead areas would be a damaging factor even in an ideal case where no electronic noise is considered, resulting in a worsening of spatial resolution and bringing imaging artifacts in the final reconstruction.

¹The contribution brought by reflected light is constant as long as the scintillation crystal is sufficiently thin. In fact, the diameter of the light cone cast on the detector layer is smaller enough to be included in the gamma camera active area (except for those areas near the borders). Whether a thicker crystal were installed, the diameter of the cone of light would have grown too big to be entirely included in the active area, leading to a loss of photons.

4.4 Reconstruction issues

4.4.1 Hicam25 - first issues

The method used to reconstruct the images is the *centroid method*. It is the simplest and the fastest method since the coordinates of the reconstructed event may be calculated with the map of the collected charge and the coordinates of the centres of the detectors. The algorithm is completed in a few steps:

$$X_R = \frac{\sum_i^n x_i N_i}{\sum_i^n N_i}, \quad Y_R = \frac{\sum_i^n y_i N_i}{\sum_i^n N_i}.$$

The result is a fast process and a good spatial resolution, if compared to the size of the detectors. However it comes with some severe problems which unfortunately have no solution but to change the reconstruction method, and move to one of the advanced techniques such as *maximum likelihood expectation* and *neural networks*.

The problems affecting image reconstruction are clearly visible in picture 4.21, which represent the most simple experiment that can be carried out with Hicam25. Images are evaluated with a pixel measuring 0.4mm . The first one is a flood image where the centres of the detectors present more counts in relation to the surrounding areas: in fact, all those gamma rays absorbed at low-z coordinates cast the visible light mostly on one detector and the event is brought back to the centre, even if it was actually located near a corner. The second image instead, is a plot of the mean value of the number of electrons collected along Hicam x-axis, considering an integrated area of a few pixel (highlighted in blue in the first image). It can be noticed that the first 5mm from each side are lost, since no event can be reconstructed near the borders: some external detectors should be placed next to the camera for the active area to be exploited entirely. Some valleys can be seen

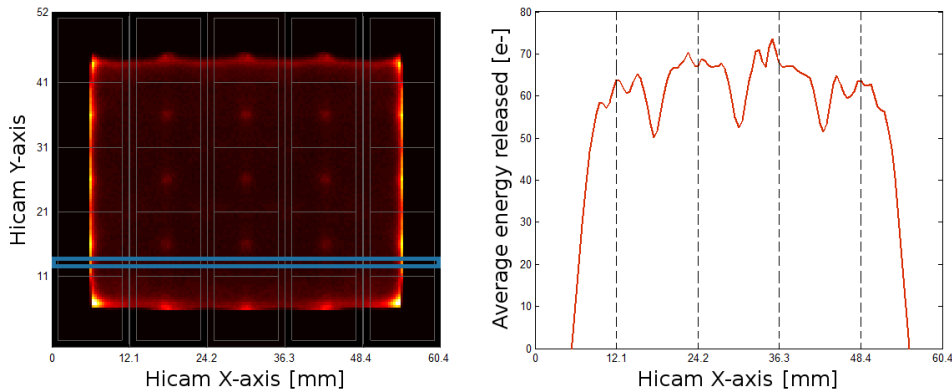


Figure 4.21: Reconstructed image of a flood acquisition and average energy absorbed in a given pixel row.

too, because the cone of light cast on the detector layer is about 2.8cm wide (diameter), thus in correspondance to the centres of the central modules the cone of light includes two dead areas, reducing the amount of photons absorbed. The centroid method leads to a limited field of view (FOV), due to the fact that the spectrum is simply built as the sum of the collected charges, with no correction or deterministic calibration based on the geometry of the active area. A possible solution is to implement an *energy correction* during reconstruction: the principle and the algorithm used will be discussed in the next chapter.

4.4.2 Hicam100 - unexpected issues

The problems encountered with the small prototype were quite easy to understand, and they were expected to occur thanks to a detailed study of the gamma camera dynamics and some simulations. However, when Hicam100 was studied, there were new issues that needed to be faced. Considering Figure 4.22, a uniform image was supposed to be seen after having processed real data. In the middle of the image instead, we can see a darker area where fewer counts are reconstructed ².

This phenomenon was associated with the presence of dead areas in the

²A big hole is shown in the bottom-right corner of the image. However it is not associated to any reconstruction artifact; a bonding bringing high voltage to that detector was broken during transportation of the gamma camera, and it wasn't possible to fix it, since experiments were carried out at *Ospedali Riuniti di Bergamo*.

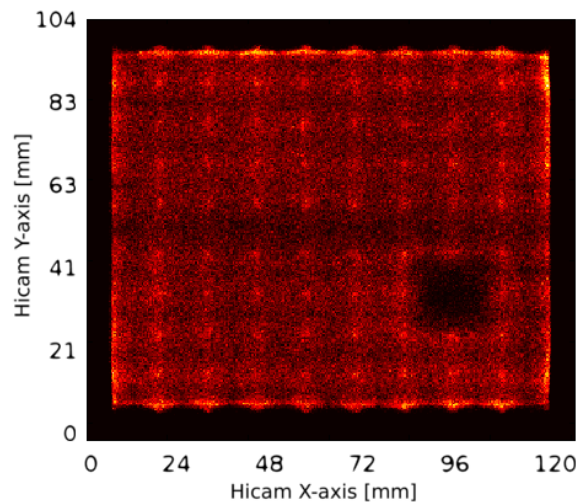


Figure 4.22: Reconstructed image processed from flood acquisition. Detector layout is omitted to show better the problem.

first place, but even if they lead to a loss of geometric efficiency, and therefore to a loss of collected charge in the detectors, they shouldn't bring to a loss of counts, but only to a worse statistic, as already said. However, the reconstruction made with the centroid method shouldn't be heavily affected. Further simulations will show why the image obtained from experimental data seems to have less counts in the central area, in correspondence to the horizontal dead area.

Simulation #1

In the first simulation 20 000 γ -rays, divided with uniform probability, will interact in two single points of the crystal. Points are expressed in *mm* units, respectively located in the centre of the horizontal dead area and in the centre of a vertical active array:

- $(X_1, Y_1) = (18, 52)$;
- $(X_2, Y_2) = (18, 80)$.

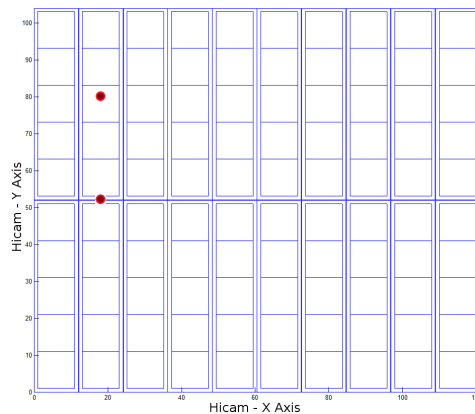


Figure 4.23: Simulation of 20 000 γ -rays, divided in two single points.

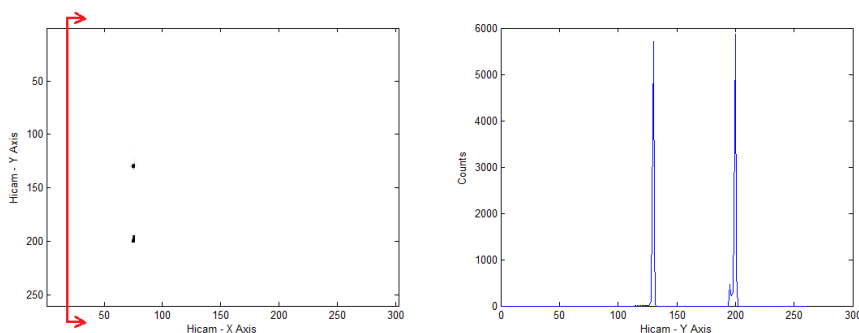


Figure 4.24: Reconstructed image of the two points (A) and profile of the counts (B).

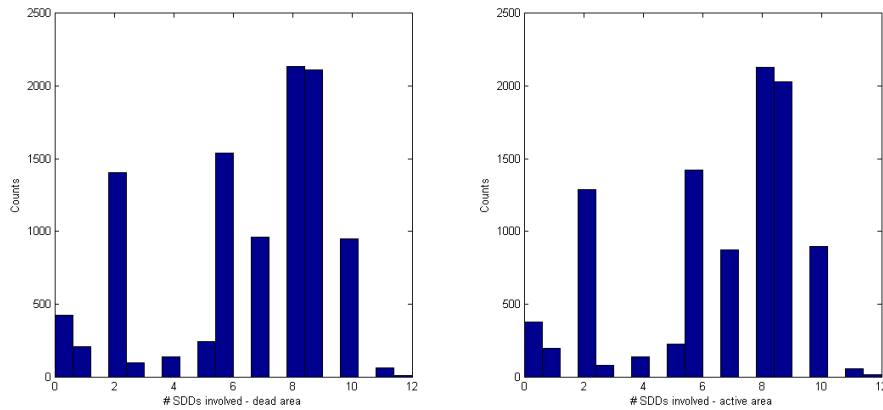


Figure 4.25: Histogram showing the distribution of the SDDs involved. (X_1, Y_1) in figure (A), and (X_2, Y_2) in figure (B).

The objective is to check if there are any attenuation issues in this case too, as seen in the experimental data. The first point, (X_1, Y_1) , was supposed to have fewer counts than the one simulated in the centre of an active area, but in figure 4.24(B) is clear that the counts of the two points are almost equal. The difference is due to the fact that some γ -rays are absorbed near the detectors ($z = 0$), casting a small cone of light on the dead area, hence no photons are collected and no event is reconstructed. Furthermore, these points are generated with a uniform probability density function, meaning that there could be some differences in the number of interactions for each point.

We also decided to check how many SDD are involved in the interactions. In fact, real data are usually filtered, considering only those events that involve from 5 to 25 SDDs. However, the maximum diameter of the cone cast is about 2.8cm , which doesn't light more than 16 SDDs if you consider only direct photons. In these simulation no filter will be applied, since the objective is to recreate an ideal situation without any electronic noise contribution that might corrupt the reconstruction. However, considering figure 4.25, the distributions of the SDDs involved are almost the same for both the points, excluding that a further filtering stage might cut some counts out; in that case, both the points would be affected in the same way, and there should be no differences between them.

This simulation hasn't been useful to explain why there are attenuated areas in the real images. We will now proceed with some other simulation considering wider areas of interaction and comparing the results with experimental data.

Simulation #2

In this simulation we decided to make 50 000 γ -rays interact in correspondance to the central horizontal dead area. The domain is uniform and limited by the following points (expressed in *mm* units):

- $(X_1, Y_1) = (6, 51)$;
- $(X_2, Y_2) = (6, 53.1)$;
- $(X_3, Y_3) = (114.9, 51)$;
- $(X_4, Y_4) = (114.9, 53.1)$.

In figure 4.27 the reconstructed image and the profile of the counts are respectively shown. In figure 4.27(B) we plotted the profiles as the sum of the counts along X axis: the profile of the input points of the simulation is in red, while the profile of the reconstructed points is in blue. The integral of the two curves is the almost same, so there aren't any losses of charge.

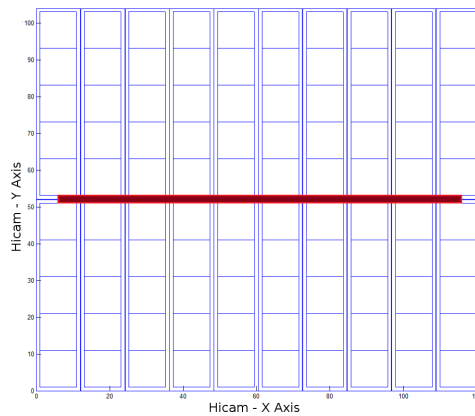


Figure 4.26: Simulation of 50 000 γ -rays, randomly distributed in the red area.

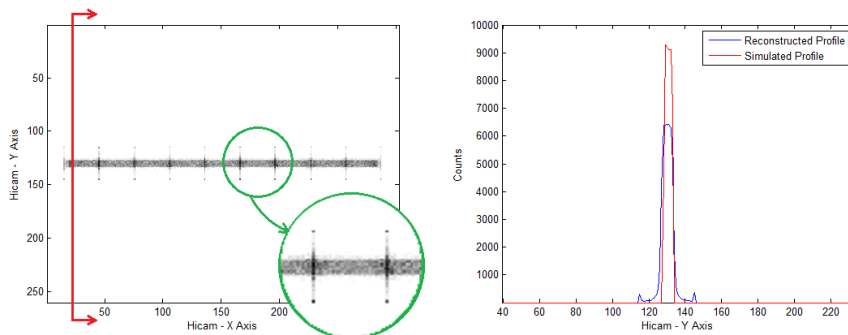


Figure 4.27: Reconstructed image of the simulated data (A) and profile of the counts (B).

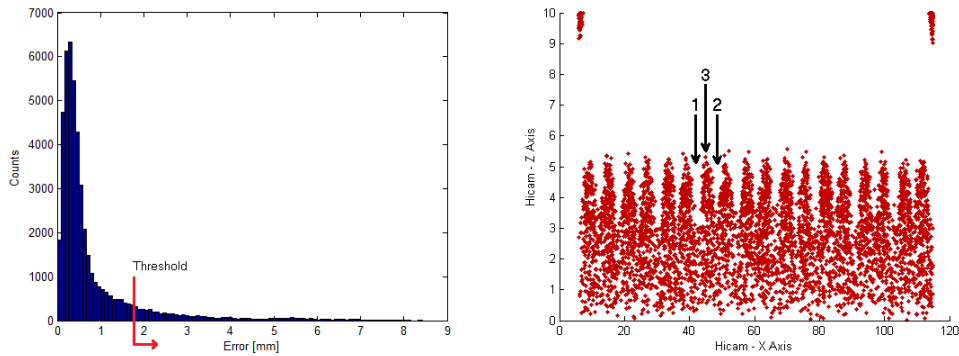


Figure 4.28: Distribution of the error (A), and location of points whose error is over threshold (X axis projections).

However, there are much fewer counts in the central part, corresponding to the dead area, because some of them are deflected towards the centres of the closest detectors, as seen in figure 4.27(A).

For this very reason, it's useful to analyze the distribution of the error, shown in figure 4.28(A). The error is defined as the distance between a simulated point and the reconstructed one:

$$\Delta\epsilon = \sqrt{(X_1 - X_s)^2 + (Y_1 - Y_s)^2}.$$

It's interesting to visualize in a spatial plot the origin of those points that will be reconstructed with a remarkable error; in figure 4.28(B) spatial distribution along 'Hicam X Axis' is shown. In this experiment we decided to set our threshold value at 1.8mm . It's clear that γ -rays that interact deep down in the scintillation crystal are then reconstructed in a fairly precise position. Among these, the ones whose error is small are usually aligned with centres or dead areas, while the others are located in between; this happens because in the first two cases, depicted in Figure 4.29.1 and 4.29.2, the centroid is right in the centre of symmetry and the effects of dead areas are less significant, while in Figure 4.29.3 symmetry is not respected and the dead areas lead to a mismatch between the actual centroid and the computed

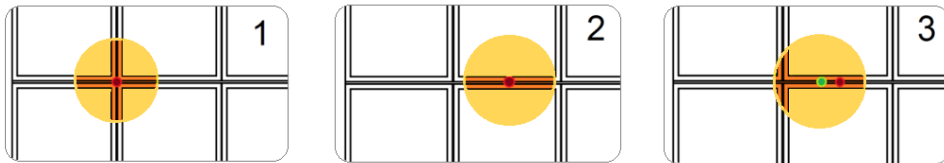


Figure 4.29: Light cast on the detectors in three different positions. Actual centroid is painted in green, while the location of the reconstructed centroid is painted in red.

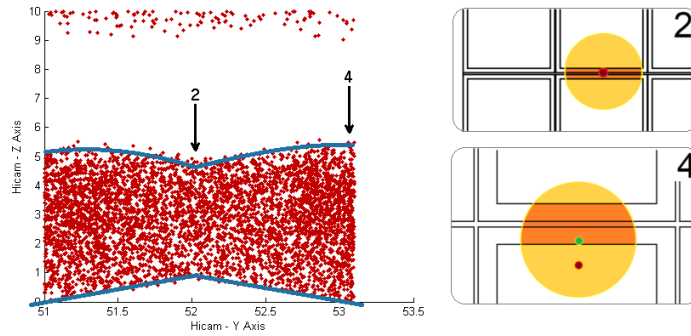


Figure 4.30: Location of points whose error is over threshold (A) and light cast on the detectors in two different positions (B). Actual centroid is painted in green, while the location of the reconstructed centroid is painted in red.

one.

Looking at figure 4.28(B), we notice that points are more sparse near $z = 0$. On one hand, error is more significant at low values of z , because the percentage of dead areas gets bigger; but on the other hand, if z is too low, we aren't even able to collect photons, because all of them hit the dead area. That's why there is an empty space near the detectors.

In figure 4.30(A) spatial distribution along 'Hicam Y Axis' is shown. It's more difficult to reconstruct points near the borders of the dead area, since the error is bigger because of the asymmetry issues previously shown. There are also some points near the top of the scintillation crystal ($z \approx 10$): these points are close to the borders of the gamma camera, and the centroid algorithm is the cause of the reconstruction error.

Simulation #3

In this simulation we decided to make 50 000 γ -rays interact in correspondance to one of the vertical dead areas. The domain is uniform and limited by the following points (expressed in *mm* units):

- $(X_1, Y_1) = (23.1, 2)$;
- $(X_2, Y_2) = (23.1.50)$;
- $(X_3, Y_3) = (25.1, 2)$;
- $(X_4, Y_4) = (25.1, 50)$.

In figure 4.32 the reconstructed image and the profile of the counts are respectively shown. The total amount of charge is the same for the simulated and the reconstructed profile, except for the differences already mentioned. The charge above the dead area is deflected towards the centers of the closest detectors though, as seen in the previous case and shown in figure 4.32(A).

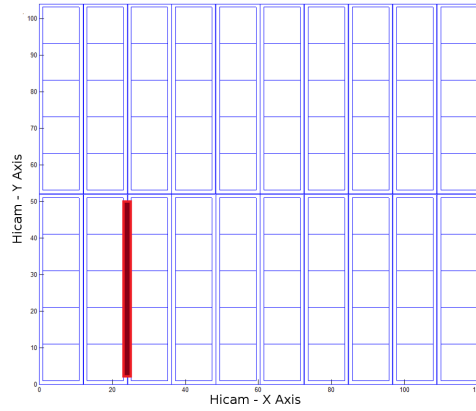


Figure 4.31: Simulation of 50 000 γ -rays, randomly distributed in the red area.

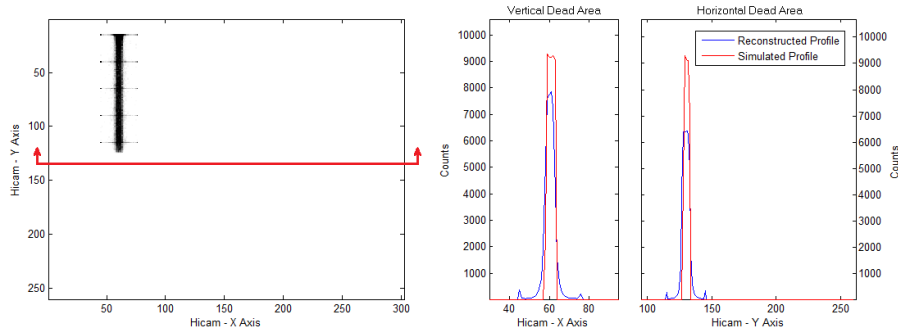


Figure 4.32: Reconstructed image of the simulated data (A) and profile of the counts (B); comparison with the horizontal dead area profile is also shown (C).

However, comparing this profile (figure 4.32(B)) with the previous one (Figure 4.32(C)), it's clear that the deterioration in the charge collection is smaller although the absolute value of total efficiency is worse (figure 4.9).

Keeping track of the simulated points, we can plot the histogram representing the distribution of the reconstruction error (figure 4.33) whose shape is very similar to the previous computation; for this reason the fixed threshold is the same, $\Delta\epsilon_{min} = 1.8mm$.

Most of the points affected by a reconstruction error are condensed near the detectors' level, at low values of z (figure 4.34(B)). Among these, most of them are located at the borders of the dead areas, and near the end of the gamma camera (figure 4.34), following the trend of the efficiency map.

In figure 4.35 a comparison between horizontal (A) and vertical (B) dead areas is made. Their effect is different: in fact, in the first case there are more points affected by reconstruction error and they're all condensed in the first $5mm$ from the detectors' level, while in the second case they're located in a layer thinner than $4mm$.

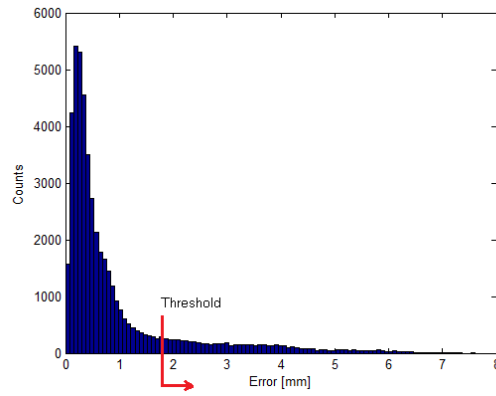


Figure 4.33: Distribution of the reconstruction error.

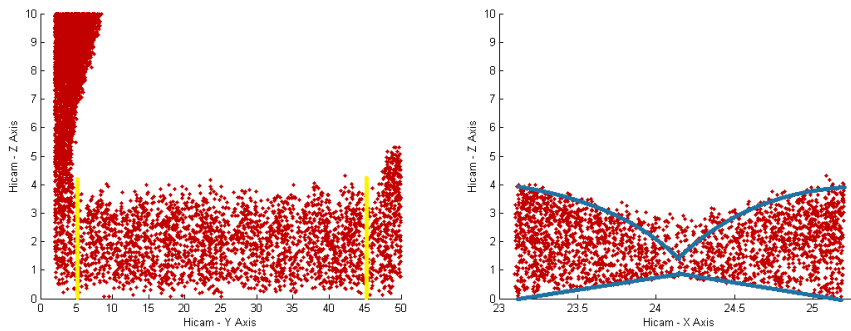


Figure 4.34: Location of points whose error is over threshold: lateral projection (A), frontal projection (B). The frontal projection considers only the points that aren't affected by border effect, evaluated between 5mm and 45mm ; these boundaries are painted in yellow in (A).

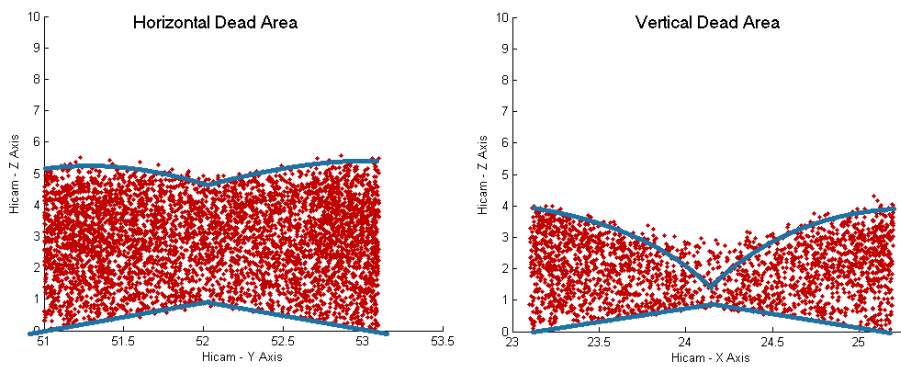


Figure 4.35: Comparison between the horizontal (A) and vertical (B) dead areas and their effect on reconstruction.

This means that, in correspondance to the vertical dead areas, there are less γ -event which are then reconstructed with a significant error. Otherwise, those points which interact above the horizontal dead area are deflected towards the centres of the detectors.

Conclusions

In conclusion, the horizontal darker area in the centre of the experimental image is a consequence of known centroid algorithm troubles; this computational method is not able to deal with asymmetry issues brought by dead areas, leading to gross errors in the reconstruction of γ -rays absorbed at low values of z . It's faulty then to state that the central area is somehow attenuated, because there's no actual loss of counts, which are just deflected and reconstructed in a wrong position. This is a validation of the previous hypothesis: the absolute values of the valleys in the efficiency map do not affect the reconstruction, but the wider they are the worse is the error brought in the processing of the events.

Looking back to the first simulation, it's now clear why there weren't any conspicuous artifacts: the two points considered were placed in the centre of a dead area (the horizontal one) and in the centre of one active area, which are particular cases. A diagram showing this phenomenon is shown in figure 4.36.

The cone of light on the detectors was symmetrical to its centre, and the dead areas were by no means a source of error: all the points were then reconstructed correctly, even if the loss of charge due to geometrical efficiency led to a worse statistic.

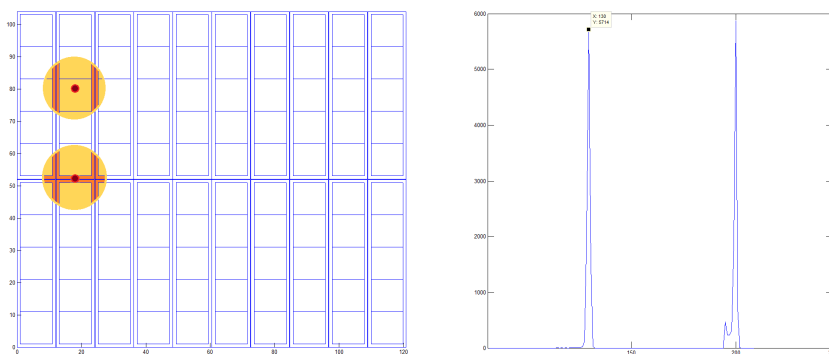


Figure 4.36: Simulation of two source of events which cast a symmetrical cone of light (A); the profile of the reconstructed image is also shown (B).

Simulated and experimental data

In this further simulation we fire 80 000 γ -rays in a rectangular area across the horizontal dead area, shown in figure 4.37. The domain is uniform and limited by the following points (expressed in *mm* units):

- $(X_1, Y_1) = (18.1, 0)$;
- $(X_2, Y_2) = (18.1, 104.1)$;
- $(X_3, Y_3) = (42.2, 0)$;
- $(X_4, Y_4) = (42.2, 104.1)$.

This simulation is meaningful because is the most similar to a real case such as the flood acquisition shown in figure 4.22. Thanks to the information gathered from the previous simulation, we're now able to make a sensible comparison and draw some conclusions.

In figure 4.38(B) the simulated profile and the reconstructed one are plotted as usual. The total charge collected is the same as expected, even if it is spread in a different way: in fact yellow and green areas compensate for each other keeping the integral of the profile constant. A deep valley is noticeable in corrispondence to the horizontal dead area in the reconstructed profile, balancing a slight increase near its borders and above the centers. In figure 4.39 the experimental data are analyzed and processed, after having selected the same area as the previous simulation. The differences between the two images, figure 4.38(A) and figure 4.39(A), are due to the fact that the simulation is carried out with a value of $ENC = 0$. In the real setup though a value of $ENC \approx 30$ is calculated. The electronic noise that obviously affect the imaging of our system is a further worsening factor of the asymmetry problem, and we're not able to deal with it as long as we keep on using the centroid method.

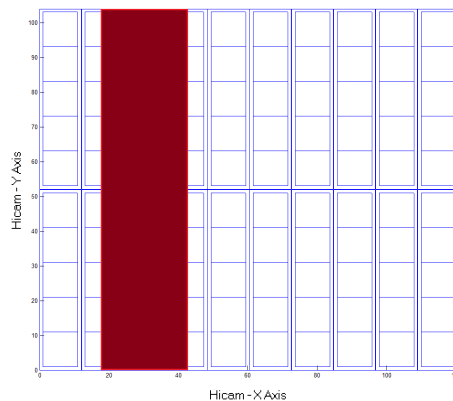


Figure 4.37: Simulation of 80 000 γ -rays, randomly distributed in the red area.

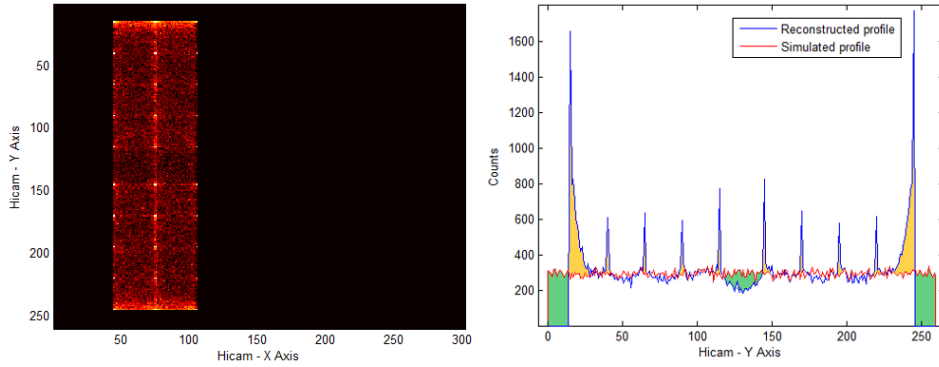


Figure 4.38: Reconstructed image of the simulated data (A) and profile of the counts (B). Yellow and green areas compensate for each other keeping the integral of the profile constant.

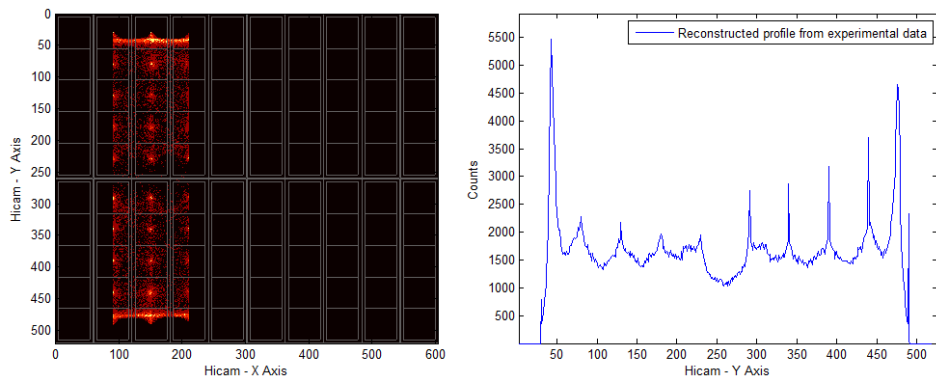


Figure 4.39: Reconstructed image of the experimental data (A) and profile of the counts (B).

Chapter 5

Reconstruction software

“Some people think that science is just all this technology around, but NO it's something much deeper than that. Science, scientific thinking, scientific method is for me the only philosophical construct that the human race has developed to determine what is reliably true.”

Sir Harry Kroto

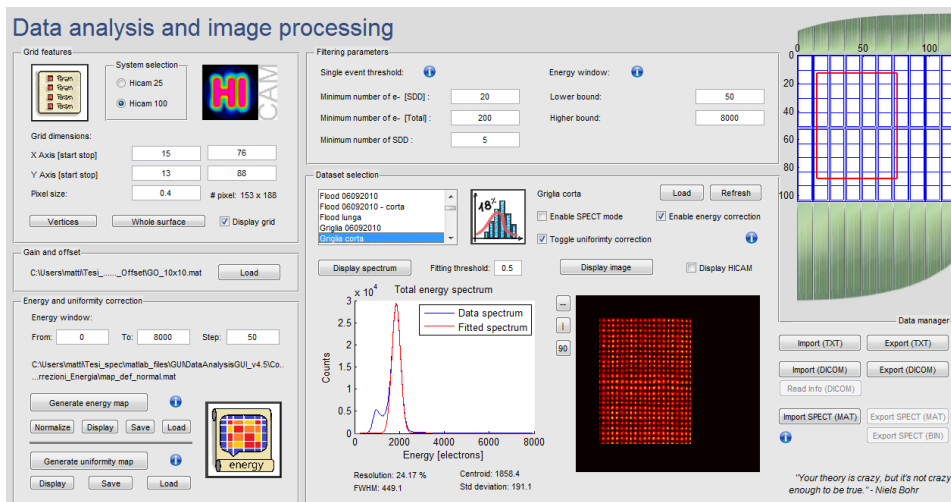


Figure 5.1: Reconstruction software developed in Matlab environment.

In the previous chapters we mentioned that a custom software was realized in *C/Basic* to save the acquired data and to carry out the post-processing operations too. However, this program was written by an external team while the system itself was being tested. Our software was thus developed in order to check immediately if the system were properly working. Several features were also added to calibrate the gamma camera, reconstruct

the images and apply corrections to the data. An overview of the functioning will be now presented, together with the results achieved in both the hardware and the software performances.

5.1 Image reconstruction

In this section the general functioning of the program will be shown, without any calibration or correction being performed.

Reconstruction area selection

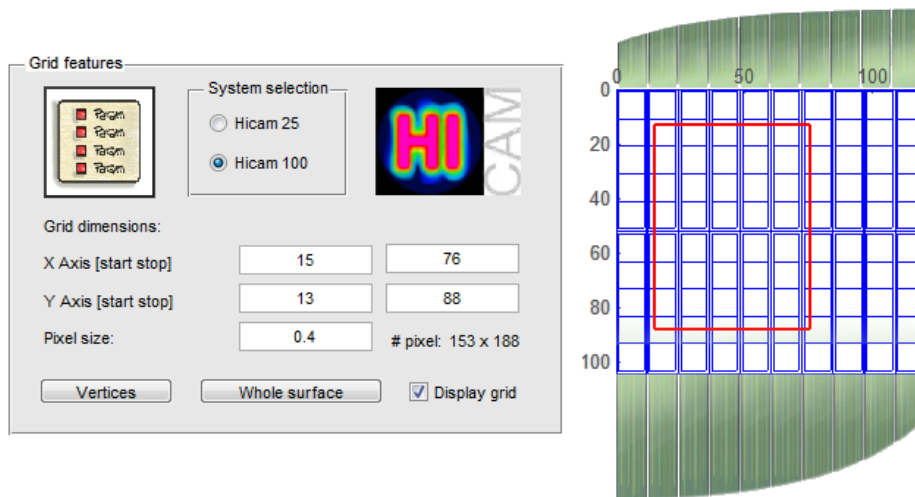
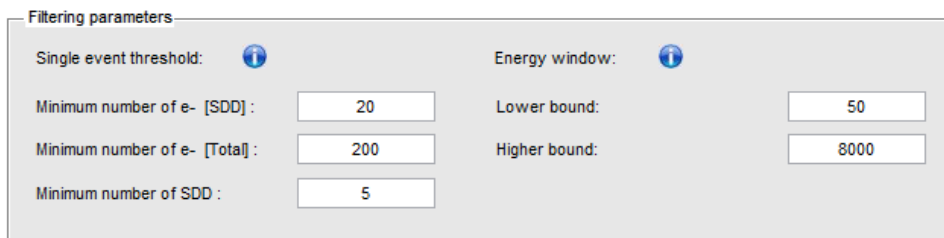


Figure 5.2: This panel is introduced to select the size and the location of the reconstruction area.

- *System selection*: the radio buttons allow to select which system is going to be used, in order to elaborate images acquired with Hicam25 or Hicam100. All the features, the parameters and the datasets are stored in different files and they're automatically loaded when the selection changes.
- *Active area coordinates*: it's possible to limit the active area of the gamma camera to a smaller field. This feature is very important because the borders of the camera do not belong to the UFOV (useful field of view) and bring a serious worsening of the energy resolution. If a specific evaluation is being carried out, it is useful to exclude a frame about $1.5 \div 2\text{cm}$ wide and reconstruct only those events which are included in the actual field of view. Coordinates of the corners may be inserted here.

- *Pixel size*: this edit box allows to change the dimension of the pixels of the final image. To choose this value correctly, a trade-off must be evaluated: a smaller pixel in fact provides a better spatial resolution, but a good statistic is required to place a significant number of events in each one. The duration of the measurement and the rate of the source are to be considered to find the correct value, which are usually chosen between $0.2mm$ and $0.8mm$ depending on the application. Images of grids and phantoms are usually reconstructed using a $0.2mm$ or a $0.4mm$ pixel size, while patients' images are reconstructed using a pixel $0.8mm$ wide to have more significant images.
- *Vertices*: this button enables a cursor that allows the reconstruction area to be traced directly on the map.
- *Whole surface*: this button selects all the active area of the gamma camera.

Filtering stage parameters



Filtering parameters	
Single event threshold: ⓘ	Energy window: ⓘ
Minimum number of e- [SDD]: <input type="text" value="20"/>	Lower bound: <input type="text" value="50"/>
Minimum number of e- [Total]: <input type="text" value="200"/>	Higher bound: <input type="text" value="8000"/>
Minimum number of SDD: <input type="text" value="5"/>	

Figure 5.3: Filtering stage parameters selection.

A filtering stage is necessary to exclude all those channels or frames which do not contribute with a significant reconstructed point in the final image.

- *Minimum number of e^- [SDD]*: this parameter acts as a threshold to determine if the number of electrons is significant to be included in the reconstruction algorithm. Some channels in fact, show negative or incredibly small values of collected charges; this situation is not physically acceptable, as it is most likely due to electronic noise, thus a value equal to 0 is set.
- *Minimum number of e^- [Total]*: this parameter acts as a threshold to determine if there is a detector which has at least a given number of electrons. This filter is introduced to exclude those rare events which are not related to an actual gamma event.
- *Minimum number SDD*: this parameter sets the minimum number of detectors that should be involved when a gamma ray is absorbed. We

have previously discussed about the problems related to the photons absorbed at low-z coordinates which, lighting only a single detector, are erroneously reconstructed in correspondance to the centre of the that detector. This filter is particularly useful when the crystal is covered with an absorbent coating.

- *Energy window*: this filter is implemented to select only those events that bring a contribute to the spectrum included in the selected range. Once the energy of the source is known, it is possible to select a narrow range to exclude those events that have been scattered on their way. In the final image only events included in that range are reconstructed and shown.

Main panel

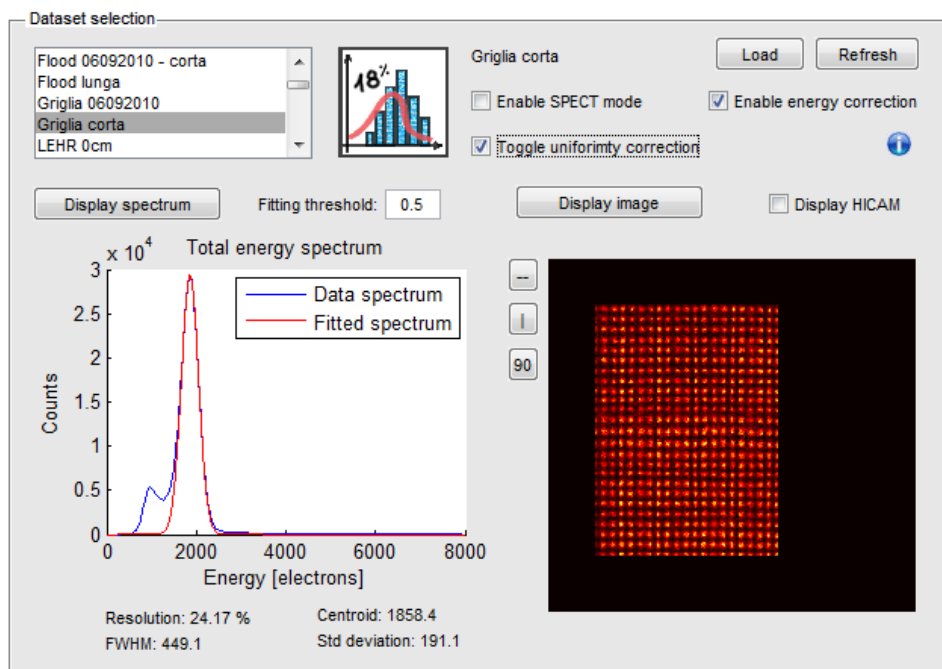


Figure 5.4: Main panel of the reconstruction software.

In this panel the results are actually shown, together with some other options implemented to improve the reconstruction.

- *Dataset selection*: this list show all the datasets imported in the default folder. All the experiments can be selected directly from this here. The list is automatically refreshed when the system selection changes, loading the data coming from experiments carried out with the other prototype.

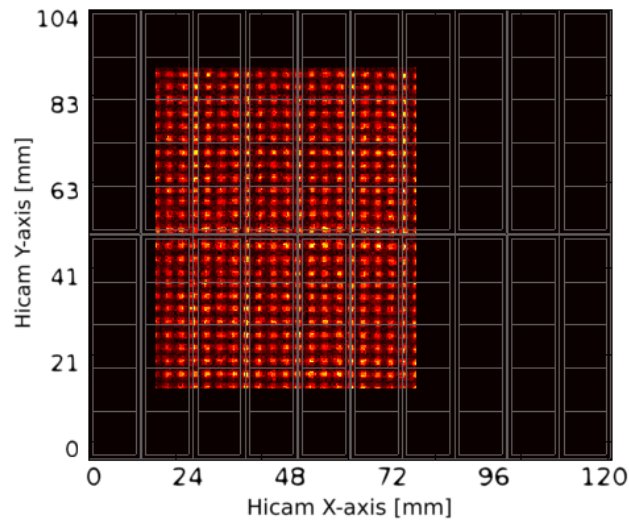


Figure 5.5: Figure of the reconstructed image, displayed together with the detector layout.

- *Spectrum figure*: in this figure the spectrum calculated from real data is plotted, together with an advanced gaussian fitting. Some significant parameters (centroid, FWHM and resolution [%]) are reported below the figure.
- *Fitting threshold*: the second peak is usually so small that may corrupt a normal fitting. The threshold is used to set the ratio that will be considered in relation to the height of the peak. If a value equal to 0.6 is typed, the program will calculate the fitting curve excluding the part of the curve below $0.6 \cdot \text{peak height}$. Usually a value equal to 0.5 is used to find the correct value of the FWHM. A specific button is also placed near the figure to open the graph in a bigger separate window, so to trace the curve in its points. The smaller peak is due to the *compton effect* and it is usually excluded from the reconstruction.
- *Image figure*: in this figure the reconstructed image is shown. Three small buttons are also implemented to rotate and reflect the image. A specific button is implemented to open the image in a separate figure, together with the possibility to display the detector layout too (figure 5.5).
- *Enable SPECT mode*: this option must be selected if the experiment to be analysed is a tomographic acquisition. In this case, a small slider is displayed below the *image figure* allowing to browse through the 180 slides acquired. Pressing the button *Play* a separate GUI will be opened to play a *mini-movie* of the rotating phantom (figure 5.6).

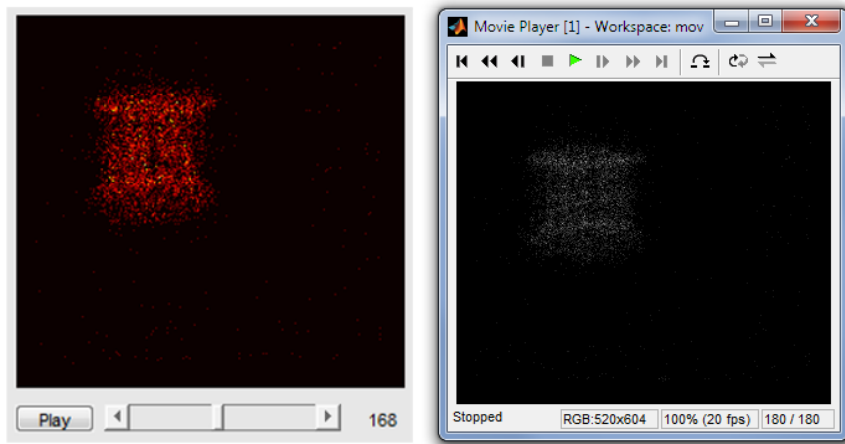


Figure 5.6: Figure showing the slides of a tomographic acquisition. A *mini-movie* can be generated to display the rotating phantom.

- *Enable energy correction* and *Toggle uniformity correction*: these two options will be discussed hereafter, when the role of calibrations and corrections will be explained too.

Data manager

The data manager allows to load or save images as *.txt* files, providing compatibility with different programs. SPECT data may be saved in *.mat* or *.bin* files. The management of DICOM files has also been included as the format is the most used in medical facilities. Several experiments were carried out with real patients with both our gamma camera and a commercial one, and

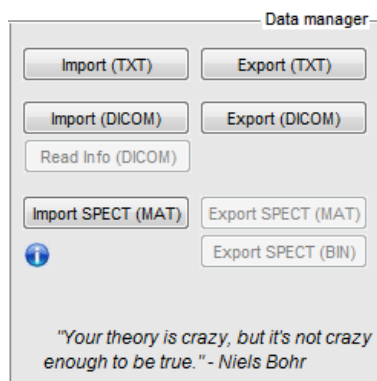


Figure 5.7: The data manager allows to save and load images saved in different formats.

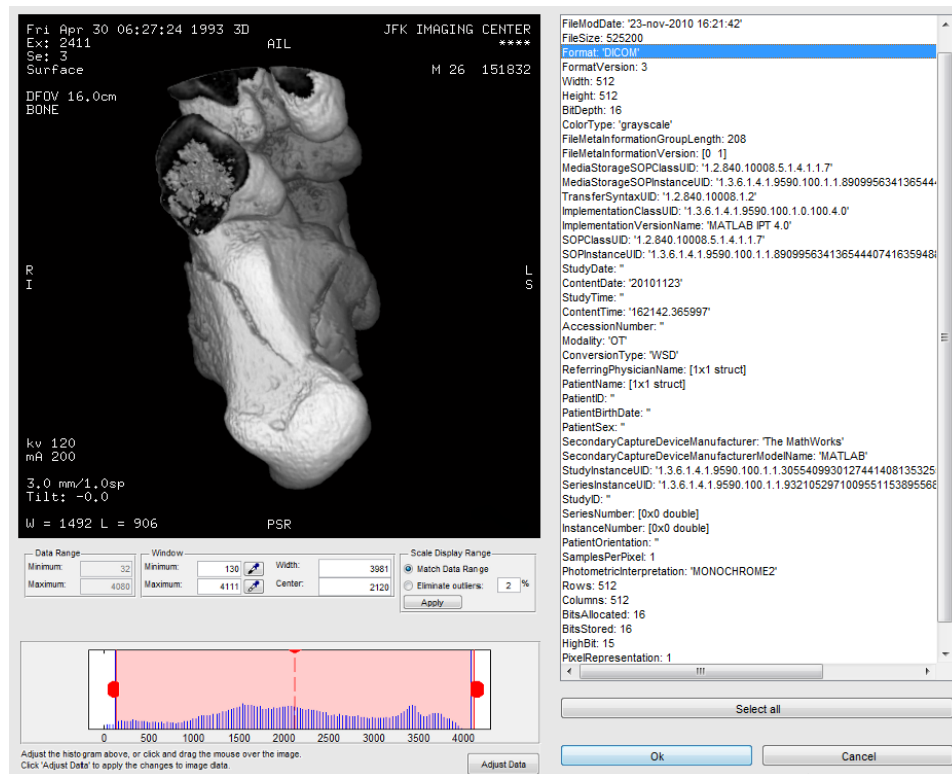


Figure 5.8: Graphic user interface implemented to visualize DICOM images.

this feature allows a comparison between the two reconstructed images. A sample is reported in figure 5.8.

5.2 Calibrations and corrections

In this section, calibrations and corrections involved in the processing will be discussed: some of them are essential for the reconstruction to be carried out correctly, while others are implemented to improve the performances of the gamma camera in terms of energy and spatial resolution[20].

5.2.1 Gain and offset calibration

Unfortunately the centroid method is suitable to process ideal data, generated with the simulator, but it is not sufficient to reconstruct a stream of raw data. In fact, due to the manufacturing process and to the preamplifier unit used in the measurement, each detector is not perfectly identical to the others, and this is visible looking at figure 5.9(A): a source of ^{55}Fe , which is known to irradiate photons with 5.9keV and 6.4keV , is pointed to the gamma camera and the spectra of single detectors are not aligned as expected. It's clear that

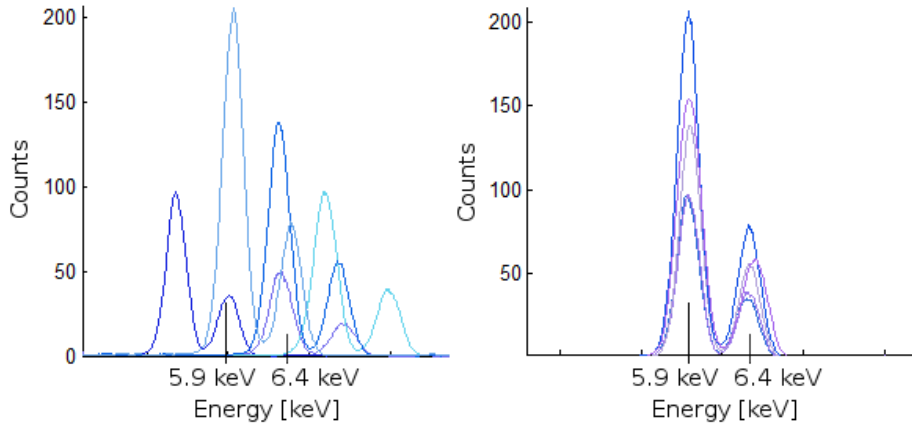


Figure 5.9: ^{55}Fe spectra of single detectors are not aligned due to manufacturing mismatches, but a suitable calibration can be implemented to align the spectra with the expected iron peaks.

without a proper calibration, different energy values (in a rather wide range) are assigned to photons coming from the same source, making it impossible for the centroid method to calculate the coordinates of the event correctly. Analysing these data, a conversion coefficient can be obtained so to align the spectra in correspondance to the real peaks of iron; an example of the spectra after calibration is shown in figure 5.9(B).

A third peak is also found at low-energy values, and it is associated with noise¹. The first step of the calibration consists in the translation of the spectrum so to align the peak of noise to the origin of the energy axis; the length of the translation is called *offset*. The second step is aimed at the alignment of iron peaks to their correct value and it is carried out rescaling the energy axis, which is divided by a coefficient called *gain*.

This calibration is carried out before the positioning of the scintillation crystal, with a ^{55}Fe source: detectors are working with X -rays absorbed directly, making it possible to evaluate the conversion coefficient properly, since photons are not spread onto several detectors and each SDD can be considered separately.

Gain and *offset* coefficients are calculated for each detector and stored in a matrix. In the reconstruction process in fact, each frame is calibrated

¹The peak is not shown in figure 5.9 because it is far from the spectrum of the signal, which needs to be represented clearly, in a narrow energy range.

by subtracting his *offset* and dividing by his *gain*². After these steps are completed, the reconstruction continues with the filtering stage and the calculation of the centroid.

5.2.2 Energy correction

Energy correction is the principal feature introduced to improve the performances of the Hicam gamma camera in terms of energy resolution. The easiest experiment that can be carried out with our gamma camera is a flood acquisition, which is completed taking advantage of a point-like radioactive source, located far from the detector level so that the active area is equally exposed. However, the energy associated with each reconstructed point is dependant on the location of the point itself, leading to an unexpected spread in the spectrum curve. The spectrum is calculated as the histogram of the energy values associated to the reconstructed points, that is achieved as the sum of the charges collected in single detectors. It is now necessary to explain how the reconstruction algorithm works, because it is essential to understand how an *energy correction map* is created and how it is then applied to other experiments.

Acquired files are loaded and each frame is processed in order to find the interaction coordinates, and the energy value associated with the gamma ray absorbed. These information are then stored in a big 3D matrix, like a three-dimensional histogram: the x-axis and the y-axis are the axis of the gamma camera, where the number of rows and columns depend on the

²Files coming from the acquisition are made by 100 rows, representing the number of detectors, and 100000 columns, representing the number of events acquires. Each column is usually called *frame*.

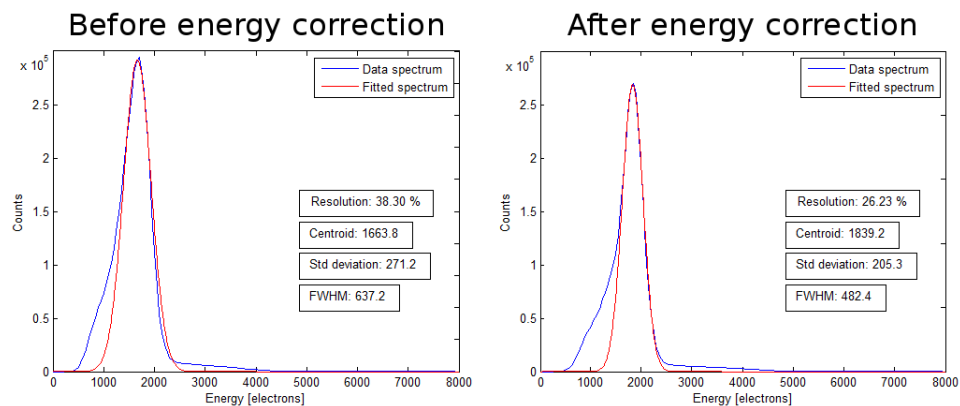


Figure 5.10: Global spectrum of a flood image calculated before and after energy correction.

dimension of the pixel, while the z-axis is the energy is the energy axis. The number of levels can be chosen according to the radioactive source involved as it represents the maximum energy value acceptable, and the step is chosen according to the capability of the calculator. In the beginning, the matrix is filled with values equal to 0, and after an event is processed a +1 is given to the cell corresponding to the spatial coordinates and to the correct energy value. In this way both the position and the energies are turned into discrete values. For each pixel, the corresponding energy axis may be plotted and the peaks are expected to have a similar value, since the gamma camera is illuminated in a uniform way. However, the real spectra have different centroids due to the presence of dead areas or other factors already discussed, like inequalities in the scintillation crystal. Considering a long experiment, a lot of data are available, and assuming an ergodic process, the centroid of the spectrum of a given pixel is going to be the located at the same energy value also in further experiments. This values, one for each pixel, is saved in a *correction map*, which will be recalled for every experiment carried out with the same source. Operating this way, an equivalent value of charge is assigned to each cell as if the spectrum of a given pixel was translated to be aligned with all the others to a normalized value. The *correction map* is generated from a flood acquisition, with a high statistic to have a smooth spectrum, where no energy window is selected. The map is then saved and may be applied to other datasets, even if the selected pixel has different dimensions, since the map is adapting to image size.

This solution allowed to reduced the spread brought by events reconstructed in different locations, and the enhancement of the performances is visible in figure 5.10 where global spectra before and after correction are shown: energy resolution records an improvement from 38% down to 26%.

5.2.3 Uniformity correction

Uniformity correction is introduced to improve the quality of the images taking care of those artifacts which can't currently be removed with a specific filtering stage. Unfortunately, this solution is not working on the collected charges, but only on the final reconstructed image, making it impossible to improve the global spectrum as well.

The correction is carried out taking advantage of a *correction map* that can be generated after the processing of a flood acquisition. In fact, this is the basic experiment, and may be considered as an *impulse response* of the system. Looking at the behaviour of the gamma camera in this situation, we can correct the occurrence of given artifacts in any experiment, since they are linked only to the reconstruction method (centroid method). Knowing that several events are wrongly reconstructed nearby the centres, they will be given a smaller weight, so to achieve a uniform image. Therefore, the correction map is simply calculated as the inverse of the reconstructed flood



Figure 5.11: Image of a thyroid phantom shown before and after uniformity correction.

image, conveniently processed with a $2D$ low-pass filter, in order to build a map which is not too close to image noise. It is important to mention that correction maps generated considering a limited energy range should be applied to images that are reconstructed according to the same energy window, since the behaviour of the gamma camera is very sensitive to the involvement of other events, especially if they're far from the energy peak. Considering the dimension of the pixel, the map may be applied to any image.

An example of the performances of the uniformity correction is shown in figure 5.11.

5.2.4 Linearity correction

Linearity correction is introduced in the reconstruction process as a method to correct the spatial distortions of planar images [21]. The field of view of our gamma camera is quite small in relation to the average distance of the source from the detector level, and the artifacts caused by spatial distortion are not so significant, nevertheless linearity correction is applied to all the images of real patients, in order to be clinically valuable.

The correction algorithm was developed by an external team from University College of London, but unfortunately it was developed in a different software environment, therefore it is not possible to describe how the algorithm works. All the images shown so far were reconstructed without taking advantage of the linearity correction.

This correction has a great impact on the final image as it can be seen in the following experiment. A lead mask, $2mm$ thick, has been manufactured and then pierced in order to create a grid of small holes, $1mm$ wide, aligned

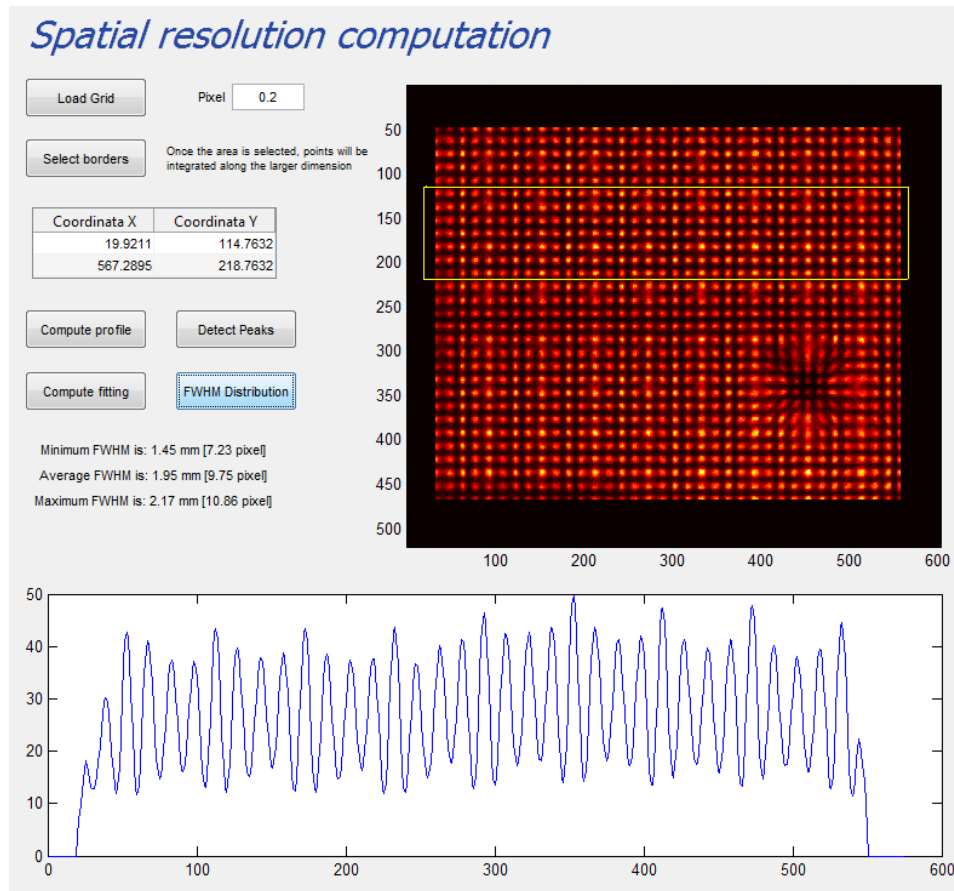


Figure 5.12: Graphic user interface built to calculate the profile of an image, in order to evaluate spatial resolution. In this screenshot a grid image is shown, processed with uniformity and linearity correction.

in a matrix with a 3mm spacing (from a centre to the next one). The mask works as a shield to the gamma camera, in which only the gamma rays passing through the holes are absorbed and reconstructed. Some images from this experiment has already been shown. When the linearity correction is also performed, all the points are aligned in a perfect grid, as well as the mask, and also the artifact due to the non-working state of a detector is almost compensated. An example of that grid is shown in figure 5.12, included in a specific GUI (developed in Matlab) created to evaluate the spatial resolution of the gamma camera.

Thanks to this GUI, saved images can be loaded to carry out evaluations concerning spatial resolution. A finite two-dimensional domain is selected upon the image with a specific cursor, and counts are integrated along the shortest dimension: in this case counts are integrated along y-axis to achieve the profile of x-axis. The profile of the counts is shown below the buttons:

every peak is fitted with a gaussian curve, in order to measure the FWHM. For these image, an average FWHM of 1.95mm is achieved.

It's important to point out that this is not the maximum resolution achievable with this gamma camera, since the diameter of the holes in the grid is too wide to carry out this kind of evaluation. A specific set of measures has been performed taking advantage of capillars located at different heights from the detector level. These data were studied by UCL, accounting a maximum spatial resolution of about 1mm , fulfilling on the most significant objectives of the Hicam project³.

5.2.5 Software implementation

Corrections and calibrations are also implemented in the reconstruction software to enhance images.

- *Gain and offset*: a button allows to load the file where values of gain and offset are stored.
- *Energy correction*: a small section is designed to generate, view, save and load, the energy correction map.

³Linearity correction is essential for these kind of analyses. In fact, if an image was to be analysed before the correction, nonaligned points would have contributed with a significant spread which does not reflect the capability of the gamma camera.

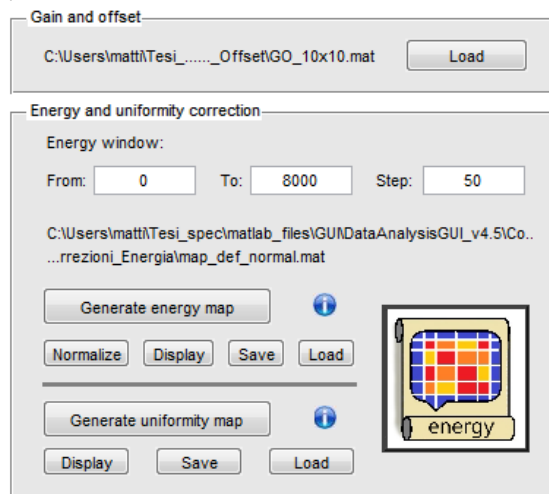


Figure 5.13: Panels embedded in the reconstruction software to load and generate correction maps.

- *Uniformity correction*: a small section is designed to generate, view, save and load, the uniformity correction map.

Correction values are strictly associated with the features of the detectors, therefore maps are to be changed according to the selected system (Hicam25 or Hicam100).

5.3 Setup of the prototype

The peculiarity of the system developed within the Hicam project consists in an extreme compactness, due mainly to the use of solid state detectors instead of a classical photomultiplier-based system. A very compact system implies, other than a smaller volume, a lower weight and, eventually, a more slender architecture of the mechanics. The final prototype needs to be limited in dimensions and weight, in order to allow a comfortable transportation and ease of use in a laboratory workbench (for example, on small animals), exploiting to its best the field of view available. The preliminary design of the main mechanics consisted of several elements:

- the detector head container;
- a rotating fork supporting the detector head;
- a rotating arm, allowing the rotation of both detector head and fork;
- an extensible motorized column, carrying all of the weight, which allows to translate vertically the detector head;
- a steel platform on wheels, where all of the elements above are mounted, as well as the cooling system and the power supply units.

The final configuration of the system is shown in figure 5.14.

The head can rotate around its longitudinal axis by two pins, which connect it to the fork. Rotation is allowed in discrete positions only, by intervals of 15 degrees. A safety lock system has been implemented to fix the head to the fork, requiring an apposite tool for mounting and dismounting. The fork can rotate around its longitudinal axis, allowing two degrees of freedom for the rotation of the head. Rotation is allowed in discrete positions only, by intervals of 10 degrees. The motorized column is equipped by a remote control for the up-down movement. The maximum available run is about 70cm. The power and signal cables, as well as the water pipes for cooling the detector head, have been gathered in a flexible pipe, fixed by a hook to the top of the moving column. The DAQ system has been initially mounted in a separated box and had been finally been mounted on a stand also located on the top of the moving column. The overall weight of the system (head, mechanics, chiller and supply unit) is about 120kg. The weight of the detector head turned out to be approximately 15kg.

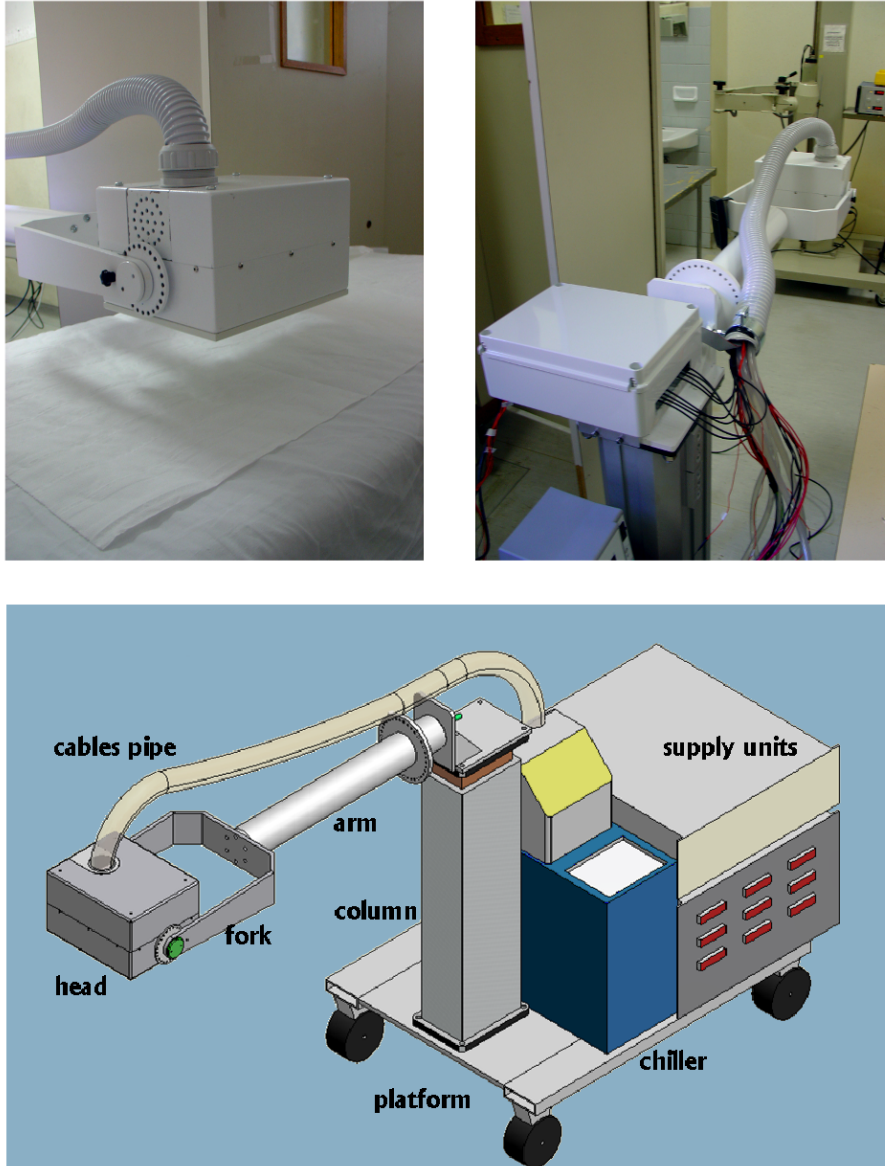


Figure 5.14: Photographs of the system in operational condition, and diagram showing the final setup.

5.4 Results and applications

In these section some of the measurements carried out with real patients are shown. For a more complete documentation, other sources must be consulted [22]. Images obtained with Hicam were very satisfactory, with high spatial resolution and high contrast, despite the modest activity administrated to the patient (about 15 MBq of ^{99m}Tc -Nanocoll).

The first image is a comparison between a thyroid phantom and a real one, and it is shown in figure 5.15. Clinical aspects of the experiments are not discussed here, as the image is reported here as a demonstration of the performances of the gamma camera developed.

A specific experiment was also completed: we selected some patients with diagnosed breast cancer (or melanoma) which needed to undergo lymphoscintigraphy to localize the sentinel nodes. Patients were imaged with Hicam prototype but also with a commercial gamma camera. For the standard acquisition *E.Cam* by Siemens was used, including a NaI(Tl) detector, 5/8" thick. In particular, in one of these studies, we found a very interesting case. Observing Hicam image it was possible to recognize a node in which the tracer was drained near the axillary region. This node was very close to the injection site and, as a consequence of this, the standard gamma camera could not recognize it. Figure 5.16 shows that in the image acquired with *E.cam*, only two nodes are visible, while in the Hicam image three distinct nodules can be seen. This is due to the better resolution of Hicam and to its possibility of a better position of the patient that reduce the target-collimator distance.

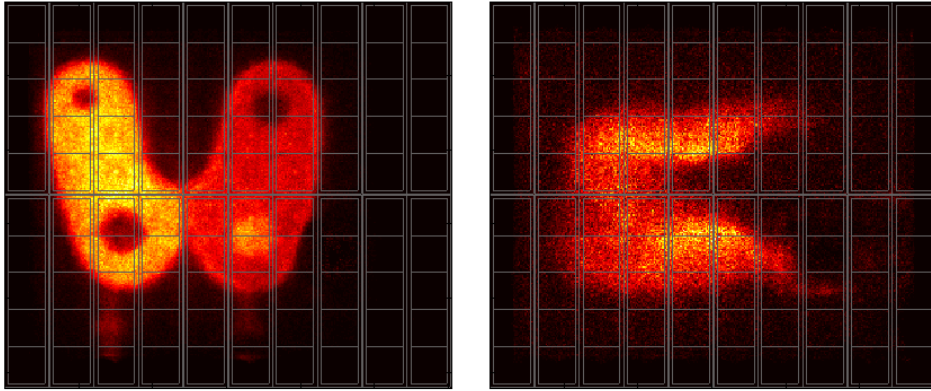


Figure 5.15: Comparison of a thyroid phantom (left) with a thyroid of a real patient (right).

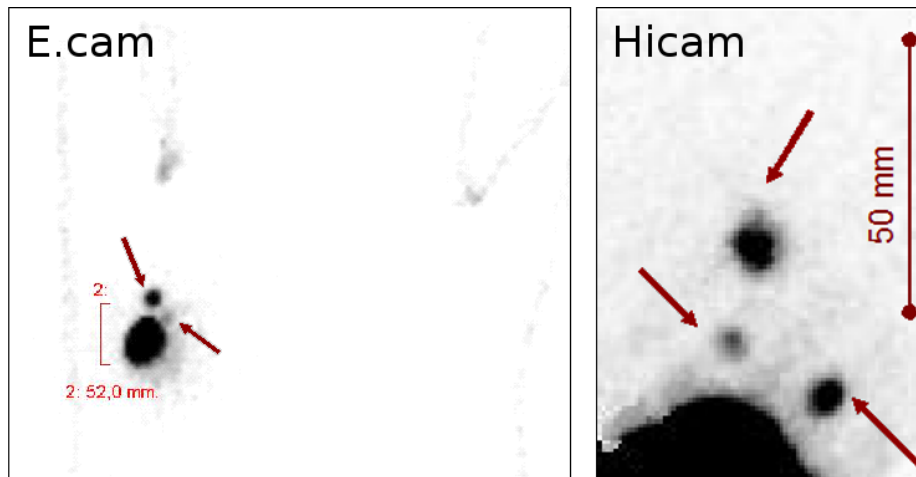


Figure 5.16: Comparison between two measurements of the same patient carried out with a commercial gamma camera (E.cam) and the Hicam prototype.

Chapter 6

Single photon emission computed tomography

“Science, like art, is not a copy of nature but a re-creation of her.”

Jacob Bronowski

The performances of the Hicam gamma camera in terms of spatial resolution, allowed us to carry out some experiments involving 3D acquisition and reconstruction. Images of the inside of the human body can be obtained non-invasively using tomographic acquisition and processing techniques. In particular, these techniques are commonly used to obtain images of a γ -emitter distribution after being injected in the human body. The reconstructed images are obtained given a set of their projections, acquired using rotating gamma cameras. A general overview of analytic and iterative methods of reconstruction in SPECT is presented with a special focus on filter back-projection (FBP), which is faster than iterative algorithms, with the latter providing a framework for accurately modeling the emission and detection processes [23].

6.1 Principles and techniques

The principle of nuclear medicine exams is to collect information about the position of a gamma tracer injected in the body of the patient: however, the image acquired represents the projection of a 3D distribution on the detector level, which is two-dimensional, losing information about the depth of interaction. To better understand the issues encountered during the reconstruction process, it's useful to analyse figure 6.1.

We define $g(s, \theta)$ as the number of scintillations detected at any location s along the detector when the detector head is at an angular position θ . We also define the quantity $f(x, y)$ as the estimated number of photons emitted

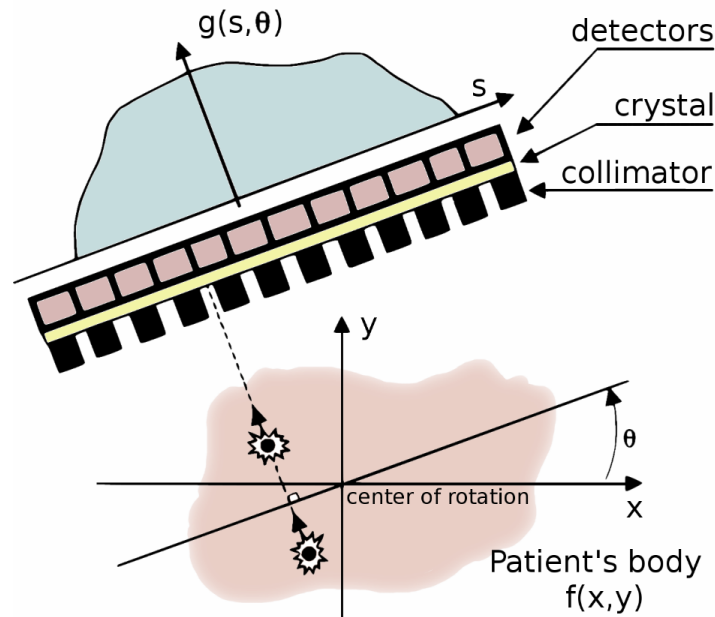


Figure 6.1: Principle of tomographic acquisition. The gamma camera is rotating around the patient's body, injected with the tracer.

at any point (x, y) of the transverse slice in the field of view. This unknown quantity is assumed to be proportional to the tracer concentration we are interested in. The function g is the projection of f onto the crystal as allowed by the collimator. This means that $g(s, \theta)$ is the sum of the radioactive counts recorded in any time interval at point s when the detector is at angle θ . The difficulty is that photons emitted at different depths, but along the same direction, can potentially produce scintillations at the same location in the crystal; thus, the distance between the emission site and the scintillation site is unfortunately unknown. As a consequence, the amount of information brought by only one projection is insufficient to obtain an image of the tracer distribution in the organ of interest, because a large number of radioactive distributions can generate the same pattern in a single projection. Moreover, activities stemming from separate structures may overlap each other on the detector plane, since the images hold integral information, leading to low contrast reconstructed images. Fortunately, the number of possible solutions can be reduced in acquiring projections for many distinct angular positions of the detector. At the end of the acquisition process, each point of the detector, for each angular position, contains the number of scintillations, or counts. A common representation for the projection data g corresponding to a slice is the *sinogram* [24]. A sinogram is a 2D image, in which the horizontal axis represents the count location on the detector, and the vertical axis corresponds to the angular position of the detector: an example is presented

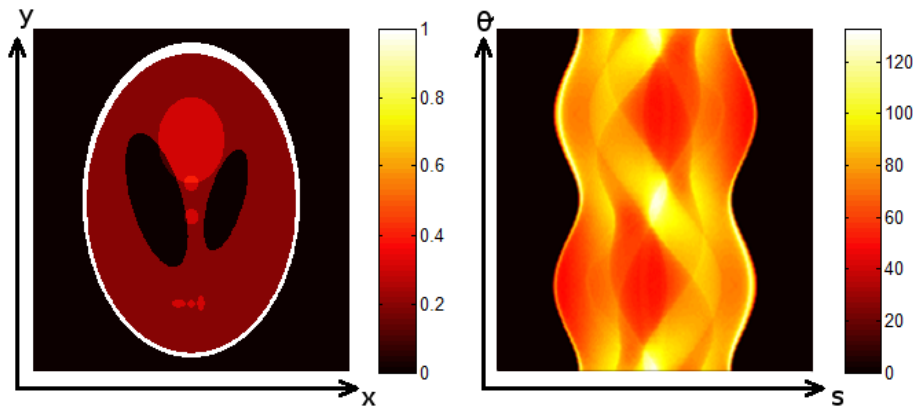


Figure 6.2: Shepp-Logan phantom (500x500 pixels), and corresponding sinogram, calculated between 0° and 359° (step = 2°). Each row of the sinogram is the projection of a slice at a given angular position of the detector.

in figure 6.2. The corresponding number of counts is assigned to each point of the sinogram. The problem is thus how to find the distribution of the radioactive source in the body, considering a given sinogram g . In this section some of the most significant methods for the tomographic reconstruction will be analysed, with a particular consideration for the *filtered backprojection method*, which is not as accurate as some others, but it is still the fastest and the simplest to be implemented.

It's also important to point out that the basic idea of a SPECT exam is to obtain, as accurately as possible, an image of the γ -emitter distribution in any slice of the body, using projections of this image acquired by a rotating gamma camera from several angles of view; all the slices are then piled up to form the final image. From now on we will consider the processing of a single slice, where the acquisition had been carried out taking advantage of a parallel hole collimator.

6.1.1 Filtered backprojection (FBP)

Projection operator and Radon transform

First of all, it's essential to consider the *projection operator*: it is defined as the number of counts detected in any point of the detector line $g(s, \theta)$ as a function of the number of counts $f(x, y)$ emitted in any point of the field of view, where $s = x \cdot \cos\theta + y \cdot \sin\theta$ is the direction parallel to the detector plane. We consider the ideal case, without noise, attenuation or scattering.

From a mathematical point of view, it's possible to calculate the projections taking advantage of the *Radon transform*, which is the line integral of the values of $f(x, y)$ along the line inclined at an angle θ from the x-axis at a distance s from the origin:

$$g(s, \theta) = \int_{-\infty}^{+\infty} f(s \cdot \cos\theta - u \cdot \sin\theta, s \cdot \sin\theta + u \cdot \cos\theta) du. \quad (6.1)$$

Actually, detectors are composed by a finite number of elements: in particular the elements of the slice are the pixels, and each point of measurement on the detector, for each projection angle, is called a bin. Thus the integral is basically a sum of values, and $g(s, \theta)$ is called *ray-sum*.

Backprojection operator

The *backprojection operator* is defined as it follows:

$$b(x, y) = \int_0^\pi g(s, \theta) d\theta, \quad (6.2)$$

and it is the operator that allows to reconstruct the slice scanned, starting from the sinogram: applying backprojection to projection data is called the summation algorithm. The integral is limited between 0 and π : in fact, in ideal conditions, the projections acquired at angles between π and 2π do not provide new information, because they're identical to the ones acquired between 0 and π , and this simmetrical situation results in a deducible periodicity in the sinogram. To carry out a perfect reconstruction, an infinite number of projections would be required: the lack of projections may lead

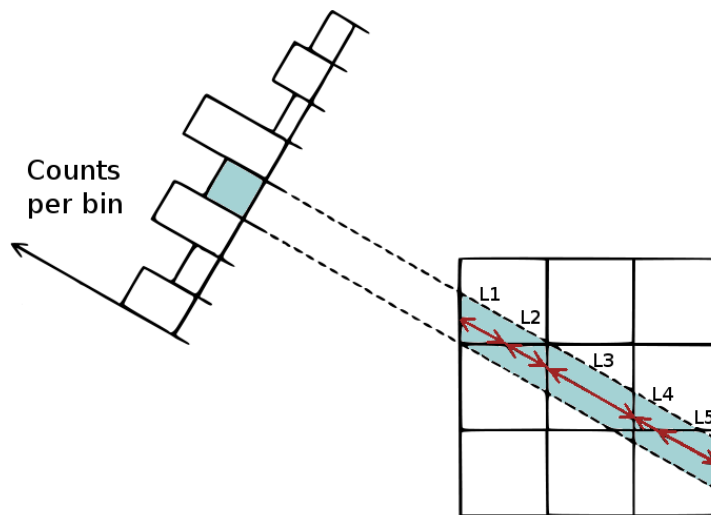


Figure 6.3: Modelization of geometry of backprojection. With ray-driven method, value attributed to each pixel along a given direction is proportional to the line length.

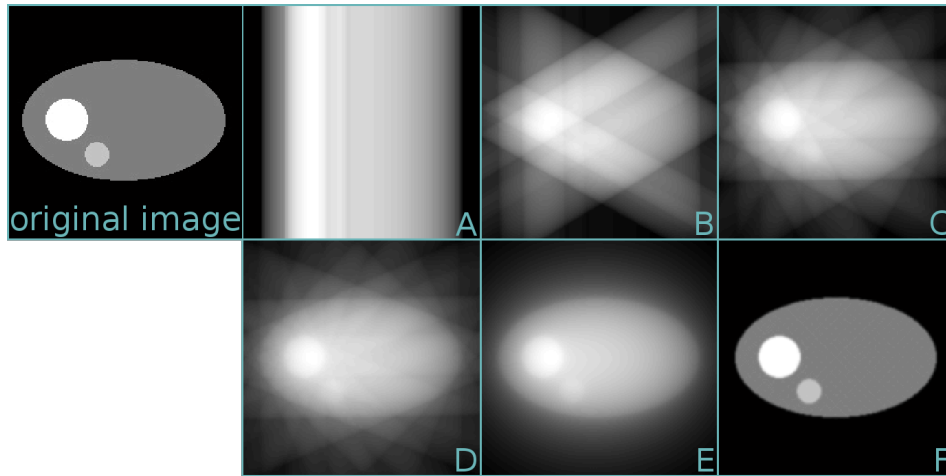


Figure 6.4: Steps of the backprojection algorithm. In the first figure the original phantom is represented. The other figures (A-D) show how the image may be reconstructed taking advantage of 1, 3, 6, 8 projections. In the last two figures the image is reconstructed with 180 projections, which are enough to avoid any artifact; however the image is blurred (E) because of the issues already dealt with, but it may be improved with a common *Hamming filter* (F), which is a two-dimensional band-pass filter.

to a *star artifact*, especially when few bins in the sinogram are considered¹.

Also the number and the dimension of the pixels must be taken into account, because these features affect the way projections are calculated and thus they must be considered in the algorithm of backprojection as well. The contribution of a given pixel to a given bin is variable, because it depends on their relative positions and the angle of acquisition. A simple solution to this problem may be the *ray-driven method*: the value in each bin is added to the image evaluating only those pixels the ray goes through, but the addition is weighted according to the ray length in each pixel, as pictured in figure 6.3.

The most important point of this examination is that the backprojection operation is not the inverse of the projection operation. This means that applying backprojection to the rows of the sinogram, $g(s, \theta)$, the result is not $f(x, y)$ but a blurred representation of $f(x, y)$. This problem is due to the fact that during the backprojection process, each bin value is attributed to all pixels that project onto that bin and not only to the pixel corresponding to the location of the source, that is unknown. Some of issues discussed are

¹The star artifact can be easily avoided increasing the number of projection. This operation is essential when the images acquired have a great number of pixel, leading to a sinogram with a lot of bins: if a good spatial resolution is achieved in the acquired images, lots of projections would be necessary to have an acceptable reconstruction as well.

described by the diagram shown in figure 6.4.

Spatial frequencies are similar to the frequencies of any other signal: a high frequency component in an image is found when the amplitude of the signal varies quickly over a given distance, in any direction. According to this specification, there are several solutions that may be implemented to solve the problem of blurred images resulting from the backprojection method. A simple solution involves the summation algorithm to backproject the projection dataset and then filtering stage to improve the result: the image is separated in a large number of frequency components which are evaluated considering different weights, according to the chosen filter. In the FBP algorithm instead, the order of these operations is reversed: first each line of the sinogram is filtered, and then the filtered projections are backprojected. One of the filters used is the *ramp filter*, which gives a weight proportional to its frequency to each of the components. With this approach, the amplitude of the low-frequency components is reduced in the sinogram, row by row, before the backprojection; high frequencies are thus enhanced, leading to a high-contrast image, with more sharpened edges. Nevertheless, much of the image noise is present at higher frequencies: the ramp filter needs to be replaced with other band-pass filters (e.g., *Hamming*, *Hann*, *Butterworth*) that also reduce the weight of the highest-frequency components, where noise typically is found. There is no univocal way to choose which filter suits best, since the reduction in noise is achieved bringing a significant loss of spatial resolution.

6.1.2 Iterative methods

The principle of the iterative algorithms is to find a solution of a problem by successive estimates. A possible schematization of our problem may be the following: finding a vector f that is a solution of $g = A \cdot f$, where g is the sinogram and f is the expected reconstructed image. After each step, the projections corresponding to the current estimate are compared with the measured projections, and the result of that comparison is used to modify the current estimate, creating a new one. There are several algorithms based on these principles, but they differ in the way measured and estimated projections are compared. In the following example, a uniform image is initialized to 0, since the additive form of the *algebraic reconstruction technique (ART)* is implemented, as an example of iterative algorithm.

The iterative process is given by:

$$f_j^{(k+1)} = f_j^{(k)} + \frac{g_i - \sum_{j=1}^N f_{ji}^{(k)}}{N}, \quad (6.3)$$

where $f_j^{(k)}$ and $f_j^{(k+1)}$ are the current and the new estimates, respectively; N is the number of pixels along ray i ; $\sum_{j=1}^N f_{ji}^{(k)}$ is the sum of counts in the

N pixels along ray i , for the k – th iteration; and g_i is the measured number of counts for ray i , as expressed in the sinogram. Considering equation 6.3, we see that the new estimate is found by adding a correction term to the current estimate, while the comparison method consists in the subtraction of the estimated projections from the measured projections. In the following paragraphs, the *CG algorithm* and the *MLEM algorithm* are introduced: both are optimization methods, working to find the best estimate for the solution according to a given criterion.

Conjugate Gradient

In the CG algorithm, the criterion used to achieve the solution is the minimization of the difference between g and $A \cdot f$.

Considering that a large number of images may be evaluated as a solution, the goal is to find which one fulfil the objective. Therefore it's necessary to observe how the difference between g and $A \cdot f$ change as a function of the value of the pixels. The simplest situation is a 2-pixel image, because it allows a 3D plot of that trend, which can be here represented as a mountainous terrain: the 2 horizontal axes are used to indicate the value of each pixel, and the vertical axis is used to plot the difference. The reasoning still holds for a larger number of pixels in the images, although the visualization is much more difficult because the number of dimensions of the plot is equal to the number of pixels in the images. The aim is to find the location of the lowest point, where the difference is minimal, because the coordinates of that point are the pixel values of the solution image. The idea is thus to start from an arbitrary location and move to a point of lower altitude an so on, until the lowest point is found. The problem is to optimize the direction and the length of the steps, so that the lowest point is reached in a minimal number of steps: the more intuitive way to is to follow the steepest descent, whose direction is the opposite to the gradient. This method is called *gradient algorithm*, or *steepest-descent algorithm*.

This method though, has efficiency issues (lots of iterations are usually required) and it is the best only in a local range; the *conjugate gradient method* is a more suitable solution, because it is more efficient and uses a combination of the current gradient with the gradient found at the previous location to calculate the next direction. These algorithms usually converge in a number of iterations equal to the number of equations of the system, which in our case is represented by the number of pixels of the image.

Maximum likelihood expectation maximization

In the MLEM algorithm, the criterion used to achieve the solution is the maximization of the likelihood of the reconstructed image.

Radioactive decay is affected by Poisson probabilistic phenomena that

bring significant variations to the measurements. As a consequence, a specific dataset \tilde{g} corresponds to a particular measurement and \tilde{f} is the specific solution, but only when the probabilistic phenomena are not taken into account. The aim of the MLEM algorithm is to find a general solution as the best estimate for f , that is the mean number of radioactive disintegrations \bar{f} in the image that can produce the sinogram \tilde{g} with the highest likelihood. Each iteration of the algorithm is divided in two steps: in the expectation step (E step), the formula expressing the likelihood of any reconstructed image given the measured data is formed, and in the maximization step (M step), the image that has the greatest likelihood to give the measured data is found.

For example, iterations may start considering a uniform disk in the field of view or a first estimate obtained by the FBP algorithm, then the EM algorithm step in and works as a set of successive projections/backprojections:

$$\text{Image}^{(k+1)} = \text{Image}^{(k)} \times \left(\text{norm.backprojection of } \frac{\text{Measured Projections}}{\text{Projections of Image}^{(k)}} \right),$$

which is a simplification of the complete formula implemented in the MLEM algorithm [23][25]. The measured projections are then compared with simulated projections of the current estimate, and the ratio between these simulated and measured projections is used to modify the current estimate to produce an updated estimate, which becomes iteration $(k+1)$.

Another algorithm that should be mentioned is the *ordered subsets expectation maximization* (OSEM) [23][26], which has also been used to reconstruct images acquired with our SPECT system [27]. Thanks to this approach, the set of projections is divided into n smaller subsets, allowing an accelerated reconstruction process using the MLEM algorithm. All the subsets contain projections equally distributed about the patient and each one is processed in turn, as a subiteration; an overall iteration is completed when all the blocks are processed. Use of n subsets in OSEM would accelerate convergence by nearly a factor of n , if compared with a standard MLEM algorithm, and it is a great improvement which is useful to shorten the computing time needed for reconstruction.

Maximum a posteriori algorithms (MAP)

The reconstructed images obtained using the MLEM algorithm tend to become noisy as the number of iterations increases, because noisy reconstructed images themselves may yield projections that are very close to the measured ones. Thus estimated projections should not be simply as close as possible to measured ones, but they also need to be not too noisy to obtain subjectively high-quality reconstructed images.

The introduction of a prior knowledge as a constraint that may favor convergence of the EM process is called regularization, and it is based on an assumption of what the true image is, in order to penalize the noisy images. The goal is now to find a solution so that the requirements are simultaneously maximized. This modified EM algorithm is called the MAPEM algorithm using the OSL approach ².

The MAP algorithm can give better image quality compared with the FBP algorithm [28], and the streak artifact observed when a region of the body is highly radioactive relative to the neighborhood has been shown to be intense with FBP but strongly reduced when OSEM is used in bone SPECT studies [29].

6.2 Hicam setup

In the previous chapters, it was shown that the Hicam system could be moved and placed next to the patient in different comfortable positions, but these operations must be carried out manually, because it wasn't possible to arrange a rotating gamma camera in these first experimental stages. For these reasons, and considering the limited active area of the gamma camera, it wasn't possible to carry out SPECT exams with real patients. However a small setup was arranged to demonstrate that the system was suitable to achieve good results in tomographic acquisitions.

A Jaszczak phantom was placed on a computer-controlled rotating stage, right above the gamma camera: instead of moving the detectors, which is a risky and difficult operation, it was decided to rotate the phantom injected

²OSL means *one-step-late*, and it is an iterative scheme used to achieve maximization.

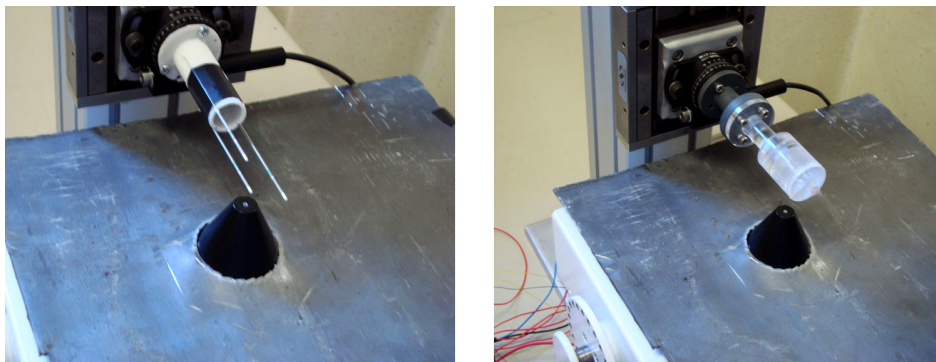


Figure 6.5: Photo of the setup used for SPECT experiments. On the left, 3 capillars are used to perform the calibration of the system, while on the right a typical phantom is being studied with a pinhole collimator.

with the radioactive source (^{99m}Tc), allowing the camera to be kept steady.

Two different phantoms were scanned. Each phantom was cylindrical, containing 6 sections with hot rods of different sizes. Within each section the rods are defined by their diameter and separation (which are equal). The first phantom had a diameter of 30mm and rods sizes of $1.4\text{-}1.9\text{mm}$, and the second one a diameter of 25mm and rods sizes of $0.7\text{-}1.2\text{mm}$. Two different collimators were used; a parallel-hole and a pinhole collimator. The parallel-hole collimator had a hole-size of 1.2mm and a length of 45mm . The pinhole collimator had an aperture of 0.6mm and a focal length of $f = 50\text{mm}$. We also performed some studies in which the pinhole collimator was placed at a distance from the detector in order to achieve a longer focal length ($f = 110\text{mm}$) and thereby a larger magnification factor. SPECT studies were done by acquiring projection data at 180 angles over 360° ; each acquisition had lasted for 30 seconds. For each setup, calibration studies were also made using three point sources, consisting of drops of activity in capillary tubes of 1mm diameter. 90 projection angles were acquired for the point sources. Pictures illustrating the pinhole SPECT setup are shown in figure 6.5, and a summary of the different experiments performed is presented in the following table.

Experiment	Phantom (rods)	Collimator	Activity(MBq)
1	$1.4\text{-}1.9\text{mm}$	Parallel hole	≈ 50
2	$1.4\text{-}1.9\text{mm}$	Pinhole ($f = 50\text{mm}$)	≈ 100
3	$0.7\text{-}1.2\text{mm}$	Pinhole ($f = 50\text{mm}$)	≈ 100
4	$0.7\text{-}1.2\text{mm}$	Pinhole ($f = 110\text{mm}$)	≈ 135

6.3 Image reconstruction

As already mentioned, a specialized team from University College of London (UCL) took part in the Hicam project as they developed software for uniformity and linearity correction of the data as well as for calibration and reconstruction of tomographic data (SPECT) for both parallel-hole and pinhole geometries [27]. The linearity and uniformity corrections in fact are also essential parts of image formation process and especially important for tomographic imaging. The reconstruction of tomographic data also requires knowledge of a number of geometric parameters. A novel calibration procedure with improved accuracy for pinhole SPECT was developed as part of their collaboration. The point source pinhole SPECT data (not shown here) were reconstructed using filtered back-projection (FBP). It's visible that the pinhole collimator gives a better resolution due to its smaller aperture. The resolution depends on the magnification factor (the ratio of the focal length and the source-to-pinhole distance): the larger the magnification, the smaller the effect of the intrinsic detector resolution. Filtered back-projection reconstructions of the two phantoms with the three collimator geometries are

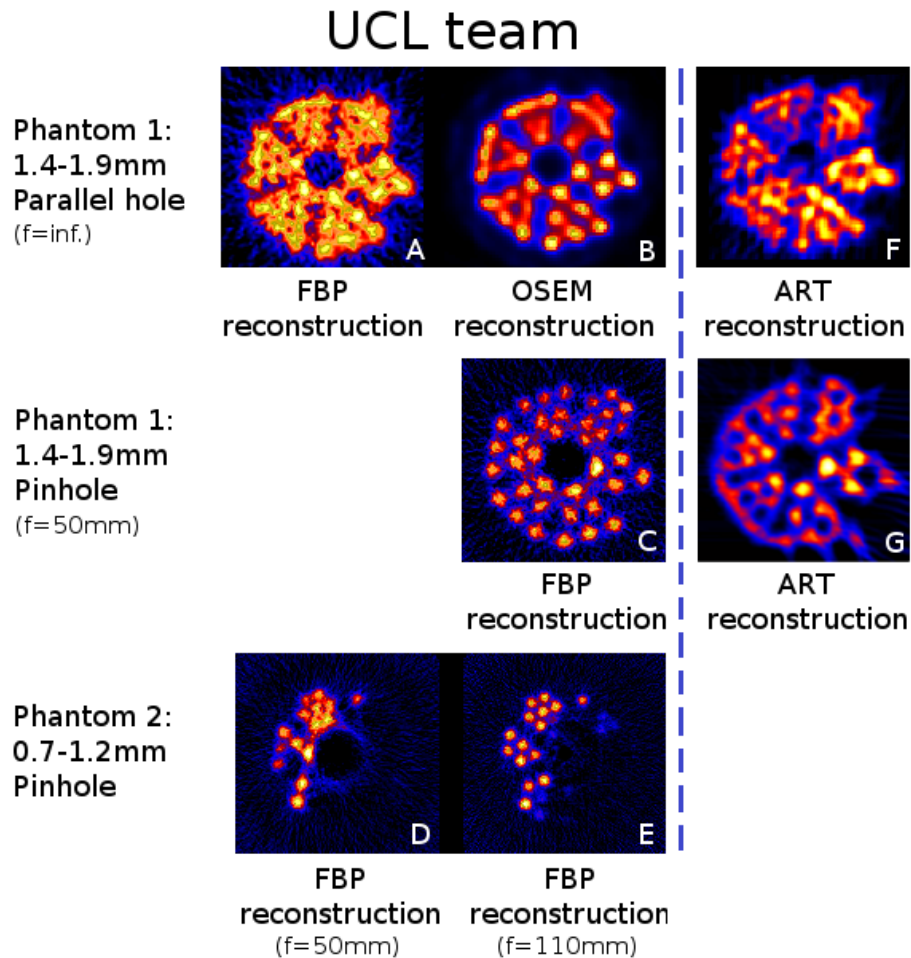


Figure 6.6: Comparison between the images reconstructed with the ART algorithm and the images reconstructed with advanced calibration techniques by a partner team from UCL.

shown in figure 6.6 (A, C, D and E).

The images have been integrated in the axial direction over a distance of 9.5 and 7.5mm for the large and small phantom, respectively, in order to improve the statistics. With the parallel-hole collimator (A) it is possible to identify the different sections in the large phantom, but it is difficult to distinguish the different rods within each section. With the pinhole collimator, each rod in the phantom can clearly be distinguished (C), due to the superior resolution. In the case of the second phantom (D, E), only about half of the phantom is visible due to filling problems. The section with the largest number of visible rods corresponds to the 1.0mm rod size. These rods are clearly distinguishable with the longer focal length (E), but

not with the shorter one (D). The reconstructed resolution can be improved by using an iterative reconstruction algorithm (such as the ordered subsets expectation maximization algorithm) with resolution recovery, as shown in image B. However, this would make an objective quantitative evaluation more difficult, as the method is non-linear. These results and experimental studies show that the HICAM detector can be used for small-animal SPECT studies with a reconstructed resolution around $1mm$.

Considering figure 6.6, images A,B,C,D and E are the images reconstructed by the team from UCL, while F and G represent our first attempt to implement the ART algorithm. It should be said that this evaluation had been carried out with a didactic purpose in order to demonstrate the validity of the method previously described. In fact, to complete the reconstruction, we took advantage of the basic tools included in Matlab, which however did not prove to be sufficient to achieve the final goal. Some issues in fact were to be faced: the most significant concerned the size of the image, whose dimensions were continuously changing because of the zero-padding method used by the program itself to fill in the remaining blanks after an image was rotated. Size is an important feature to be kept constant because in an iterative process they need to be compared to each other and corrected at every step. Furthermore, iterations should be depending on a specific figure of merit to converge, for example the minimum error accepted between two variables: our algorithm however, was limited to 10 iterations only, since no visible improvements were noticed.

The most important difference that should be mentioned is that images F and G were reconstructed without the employment of a proper calibration process, which was involved only in the reconstruction of images A to E. This difference is very relevant, especially when a pinhole acquisition is evaluated. In fact, the size of the phantom is comparable with the focal length of the collimator, which provide a variable magnification factor to different areas of the phantom, during the same acquisition: therefore the further part of the phantom results magnified by a greater factor on the detector level. Also the phantom is not symmetrical, and projections over the first 180° are not enough to reconstruct correctly the image. Therefore, if all the 180 projections over 360° are evaluated, it is impossible to achieve convergence without a previous calibration process; otherwise, considering only the first 90 projections (over 180°), a blurred image is obtained, with a great loss in terms of spatial resolution because useful information is being ignored.

The results achieved with the ART algorithm should be investigated in a more detailed way in order to obtain significant improvements.

ART algorithm

An example of the code implemented to carry out the reconstruction with the ART algorithm is reported hereafter as a demonstration of the formulas

previously analysed:

```
% Loading of data and uniformity map

load phantom_big_pinhole
load unif_map

% Application of the uniformity map to every single slice;
%
% Centroid_figure is a 3D matrix that contains the projections;

for i=1:180
    centroid_figure(:,:,i)=centroid_figure(:,:,i).*unif_map;
end

% This is the start of every iteration: the following lines
% must be executed whenever a new iteration is needed;

% This cycle is necessary to build the sinogram in which every
% column represent a projection at a given angle;
%
% Only 90 projections are considered because projections over
% 180 degrees are enough to reconstruct the image.

for u=1:90
    projection_base(:,u)=smooth(sum(centroid_figure(:,:,u)),...
        ...filter_length);
end

% In this part the first image is reconstructed with the Matlab
% function 'iradon' that is based on the FPB method.
%
% Images need to be resized because of the zero-padding method that
% Matlab uses to fill in the blanks after a rotation.

back_proj_base=iradon(projection_base,0:2:178,'hann');
back_proj_base=back_proj_base(2:end-1,2:end-1);

projection_base_resize=projection_base((size(projection_base,1)-...
    ...size(back_proj_base,2))/2+1:end-(size(projection_base,1)-...
    ...size(back_proj_base,2))/2,:);
```

```

% In this part the correction factor is generated comparing the latest
% sinogram with the one generated with read acquired data;
%
% The correction is applied and the image is prepared to be processed
% with the correction factor extracted from the next projection;
%
% 'i' is an index that represent the current projection.

```

```

for i=1:90
    projection_iter=radon(back_proj_base,0:2:178);
    projection_iter_resize=projection_iter((size(projection_iter,1)-...
        ...size(back_proj_base,2))/2+1:end-(size(projection_iter,1)-...
        ...size(back_proj_base,2))/2,:);
    correction=(projection_base_resize(:,i)-...
        ...projection_iter_resize(:,i))/size(back_proj_base,1);

    [back_proj_base]=rotate_resize(back_proj_base,i*2);

    for j=1:size(back_proj_base,1)
        back_proj_base(j,:)=back_proj_base(j,:)+correction';
    end

    [back_proj_base]=rotate_resize(back_proj_base,-i*2);
    index=find(back_proj_base<0);
    back_proj_base(index)=0;
end

```

```

% Display of the final image at the end of the iterations.

```

```

imagesc(back_proj_base)
axis image

```


Chapter 7

Conclusion and future developments

“I have learned to use the word impossible with the greatest caution.”

Werner von Braun

The objectives of the Hicam project were fulfilled with good results, also validated with a comparison of our images with the ones acquired with a standard gamma camera, currently used in several hospitals. In that experiment, a high spatial resolution of Hicam proved to be essential to the detection of small hot spots that could not be found with a standard gamma camera.

A significant improvement in terms of energy resolution was also achieved, even if the dynamics of this phenomenon are still a research object: in particular, the dependance of the resolution on the temperature of the crystal and the properties of the coatings applied on the surfaces are to be investigated. In fact, our performances in this field are limited by the impact of electronic noise that can be reduced with the design of a new ASIC, which is currently under development. The role of energy resolution is very important especially in experiments with patients, where the possibility of excluding scattered events reflects in sharp and contrasted reconstructed images.

The main limit to these issues is the implementation of the centroid method, which proved to be fast but not accurate enough to calculate the correct reconstructed point and account the actual energy value. These defects lead to the reconstruction of images with uniformity problems, due to the fact that the depth of absorption of gamma rays cannot be traced. Several filtering stages were also implemented both in this measurement campaign and in other experiments which are currently running, but they could not compensate the artifact brought by the centroid method. One of the solutions is the implementation of more advanced reconstruction methods

like *maximum likelihood expectation (MLE)* and *neural networks (NN)*, and a team from our laboratories is considering which approach is the most suitable to our device.

Despite these facts that are still to be studied, Hicam proved to be a flexible device which can be involved in different kinds of applications.

In fact, Hicam is being used to carry out imaging experiment with sources provided with higher energy values. Up to now, rewarding results were achieved, and an example is presented in figure 7.1.

Furthermore, in-vivo experiments will be carried out on small animals. In fact, plain scintigraphy was already being performed in previous phases of the Hicam project: an image acquired back then is shown in figure 7.2. However, there were issues concerning the the count rate of the acquisitions, which was a limit to the duration of the measurements that proved to be very long, making it impossible to complete a SPECT exam. For this reason, a newly designed electronic apparatus was implemented, solving the problem of the count rate. After having enhanced the device, SPECT experiments could be performed easily and good results have already been shown with the reconstruction of small phantoms. The next objective is thus the fulfillment of in-vivo SPECT experiments involving small animals.

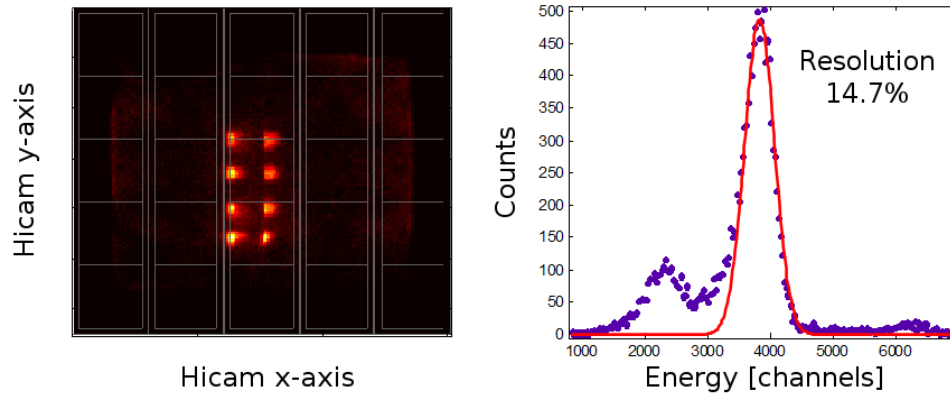


Figure 7.1: A collimated source of ^{137}Cs (661 keV) is shifted, while pointed at the gamma camera from an orthogonal direction. The spectrum is calculated considering the measurement of a single point only

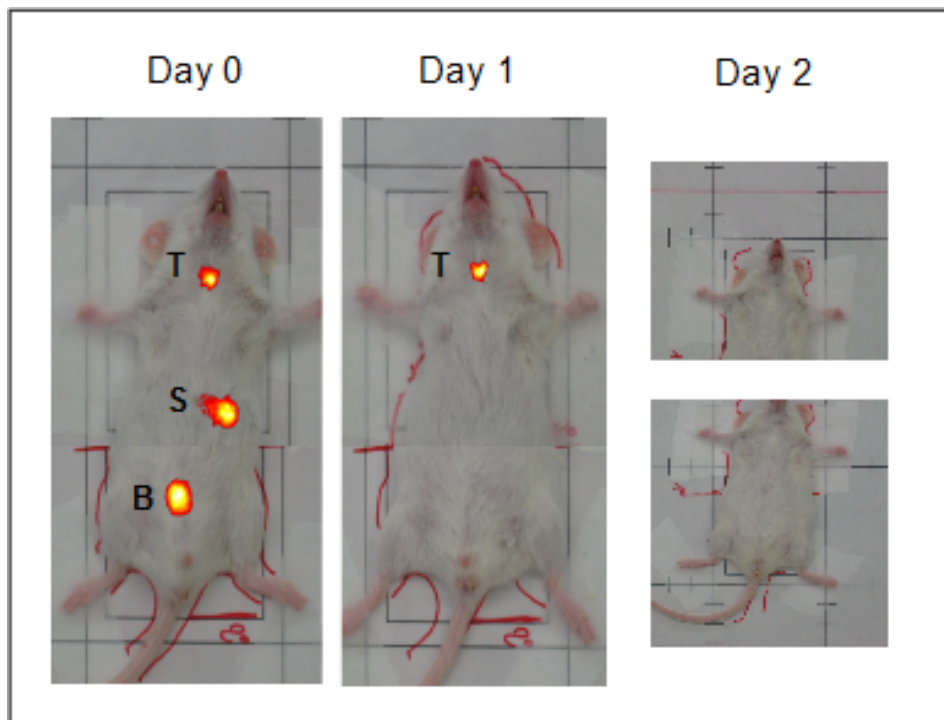


Figure 7.2: Biodistribution of ^{123}I in a small mouse. T=thyroid, B=bladder, S=spleen.

Bibliography

- [1] C. Fiorini, “Progettazione elettronica per strumentazione biomedica (academic course material),” AA 2009 - 2010.
- [2] Wikipedia, “Dual-energy x-ray absorptiometry.”
- [3] U. degli studi di Padova, “Nuclear medicine school (academic course material).”
- [4] Wikipedia, “Radioactive decay.”
- [5] Wikipedia, “Isomeric transition.”
- [6] G. Knoll, *Radiation detection and measurement*. Wiley New York:, 1989.
- [7] E. Gatti and P. Manfredi, “Processing the signals from solid-state detectors in elementary-particle physics,” *La Rivista del Nuovo Cimento (1978-1999)*, vol. 9, no. 1, pp. 1–146, 1986.
- [8] A. Longoni and C. Fiorini, “X-ray detectors and signal processing,”
- [9] A. Gola, L. Bombelli, C. Fiorini, T. Frizzi, G. Membretti, R. Nava, and R. Peloso, “A multi-channel ASIC for the readout of the HICAM gamma camera,” in *Nuclear Science Symposium Conference Record, 2008. NSS’08. IEEE*, pp. 1810–1814, IEEE, 2008.
- [10] NUclearFieldsInternational, “Collimator design calculator - <http://www.nuclearfields.com/collimators-design-calculator.htm>.”
- [11] Geant3, “<http://wwwasd.web.cern.ch/wwwasd/geant/index.html>.”
- [12] A. Bird, T. Carter, A. Dean, D. Ramsden, and B. Swinyard, “The optimisation of small csi (tl) gamma-ray detectors,” *Nuclear Science, IEEE Transactions on*, vol. 40, no. 4, pp. 395–399, 1993.
- [13] D. McElroy, S. Huang, and E. Hoffman, “The use of retro-reflective tape for improving spatial resolution of scintillation detectors,” *Nuclear Science, IEEE Transactions on*, vol. 49, no. 1, pp. 165–171, 2002.

-
- [14] M. I. staff writers, "Spect/mri hybrid prototype looks deep into soft tissues of the brain," 20-07-2010.
- [15] E. Gatti and P. Rehak, "Semiconductor drift chamber - An application of a novel charge transport scheme," *Nuclear Instruments and Methods in Physics Research*, vol. 225, no. 3, pp. 608–614, 1984.
- [16] P. Busca, "Hicam: sviluppo di una gamma camera per imaging medicale ad elevata risoluzione spaziale," Master's thesis, 2009.
- [17] C. Fiorini, "Gamma detectors for spectroscopy and imaging based on scintillators coupled to semiconductor detectors," in *Proceedings of SPIE*, vol. 4141, p. 97, 2000.
- [18] A. Syntfeld-Kazuch, L. Swiderski, W. Czarnacki, M. Gierlik, W. Klamra, M. Moszynski, and P. Schotanus, "Non-proportionality and energy resolution of csi (tl)," in *Nuclear Science Symposium Conference Record, 2006. IEEE*, vol. 2, pp. 1144–1149, IEEE, 2006.
- [19] C. Fiorini, A. Gola, M. Zanchi, A. Longoni, P. Lechner, H. Soltau, and L. Struder, "Gamma-Ray Spectroscopy With LaBr₃:Ce Scintillator Readout by a Silicon Drift Detector," *Nuclear Science, IEEE Transactions on*, vol. 53, no. 4, pp. 2392–2397, 2006.
- [20] M. Jeong, Y. Choi, Y. Chung, T. Song, J. Jung, K. Hong, B. Min, Y. Choe, K. Lee, and B. Kim, "Position mapping, energy calibration, and flood correction improve the performances of small gamma camera using pspmt," in *Nuclear Science Symposium Conference Record, 2003 IEEE*, vol. 3, pp. 2103–2107, IEEE.
- [21] E. G. N. G. A. K. C. P. D. Thanasas, D. Maintas and E. Stiliaris, "Correcting spatial distortion and non-uniformity in planar images from gamma camera systems," *2008 IEEE Nuclear Science Symposium Conference Record*, 2008.
- [22] F. Fort, "Applicazione della gamma camera hicam in sperimentazione clinica," Master's thesis, 2011.
- [23] P. Bruyant, "Analytic and iterative reconstruction algorithms in spect," *Journal of Nuclear Medicine*, vol. 43, no. 10, p. 1343, 2002.
- [24] M. G. Signorini, "Bioimmagini (academic course material)," AA 2009 - 2010.
- [25] K. Lange and R. Carson, "EM reconstruction algorithms for emission and transmission tomography.," *Journal of computer assisted tomography*, vol. 8, no. 2, p. 306, 1984.

-
- [26] H. Hudson and R. Larkin, "Accelerated image reconstruction using ordered subsets of projection data," *Medical Imaging, IEEE Transactions on*, vol. 13, no. 4, pp. 601–609, 1994.
- [27] K. Erlandsson and B. Hutton, "Report on spect configuration for pre-clinical and clinical use and results of spect performance measurements."
- [28] C. Wang, W. Sneijder, G. Bilbro, and P. Santago, "Performance evaluation of filtered back projection reconstruction and iterative reconstruction methods for PET images," *Computers in Biology and Medicine*, vol. 28, no. 11, p. 13, 1998.
- [29] D. Blocklet, A. Seret, N. Popa, and A. Schoutens, "Maximum-likelihood reconstruction with ordered subsets in bone SPECT," *Journal of Nuclear Medicine*, vol. 40, no. 12, p. 1978, 1999.